

Geomorphology

Gravitational slope processes triggered by past earthquakes on the Western Cantabrian Mountains (Sierra de la Sobia, Northern Spain)

--Manuscript Draft--

Manuscript Number:	GEOMOR-10601R2
Article Type:	Research Paper
Keywords:	Rock-avalanche; U/Th dating; Quaternary tectonics; Cantabrian Mountains
Corresponding Author:	Francisco José Fernández, Ph.D. University of Oviedo Oviedo, Principado of Asturias SPAIN
First Author:	Francisco José Fernández, Ph.D.
Order of Authors:	Francisco José Fernández, Ph.D. Rosana Menéndez-Duarte Luis Pando Laura Rodríguez-Rodríguez Miguel Iglesias
Abstract:	<p>Sierra de la Sobia is a linear mountain range of arcuate shape, located west of the Cantabrian Mountains. The long-lived crustal León Fault runs along its western hillslope, and its trace is partially covered by multiple rock-avalanches. Here we discuss if recurrent paleo-earthquakes in the M6+ range could have acted as the triggering factor for rock-avalanches in a region where the historical and instrumental seismic records only include seismic events up to M 4.6. Evidence concurring with a coseismic origin includes: (i) kinematic of current-lived minor transverse and parallel faults to Sierra de la Sobia is consistent with a horizontal North-South re-tightening of the Cantabrian Arc; (ii) slopes of the depletion zones would become unstable if horizontal ground seismic rose 0.10–0.15 g; and (iii) block size-reduction by dynamic fragmentation creates block size distribution with fractal dimension, ranging between 2.24 and 2.70. U/Th dating of seven calcite precipitates coating the blocks of cemented rock-avalanche deposits suggests that cementation has taken place in multiple episodes since MIS-9a. Neotectonics of Sierra de la Sobia are expressed in subtle changes in relief after extremely rapid co-seismic events, with average recurrence intervals much longer than the time covered by the regional historical and instrumental period.</p>

Comment on Ms. Ref. No.: GEOMOR-10601 by F.J. Fernández et al.

ffernandez@uniovi.es

Francisco José Fernández. Departamento de Geología, Universidad de Oviedo, Jesús Arias de Velasco sn, 33005 Oviedo. Spain

Dear Markus,

The few minor errors found in the revised version by the reviewers of our Ms have been corrected.

We hope you will find it suitable for publication in Geomorphology.

Best regards,

FJ Fernández

In addition, we provide a marked-up manuscript version showing the few minor errors corrected (highlighted in red).

Paleo-earthquakes M6+ triggered rock- avalanches in the Western Cantabrian Mountains.

Kinematic of active faults being consistent with a horizontal N-S compression.

Slopes of the depletion zones become unstable with horizontal seismic ground > 0.10 g.

Dynamic fragmentation is not fractal and change in block size ca 1 m.

Sierra de la Sobia is a linear mountain range of arcuate shape, located West of the Cantabrian Mountains. The long-lived crustal León Fault runs along its western hillslope, and its trace is partially covered by multiple rock-avalanches. Here we discuss if recurrent paleo-earthquakes in the $M6+$ range could have acted as the triggering factor for rock-avalanches in a region where the historical and instrumental seismic records only include seismic events up to M_s 4.6. Evidence concurring with a coseismic origin includes: (i) kinematic of current minor transverse and parallel faults to Sierra de la Sobia being consistent with a horizontal North-South compression of the Cantabrian Arc; (ii) slopes of the depletion zones that would become unstable if horizontal seismic ground rose 0.10–0.15 g; and (iii) block size-reduction by dynamic fragmentation creating block size distribution with fractal dimension, ranging between 2.24 and 2.70. U/Th dating of seven calcite precipitates coating the blocks of cemented rock-avalanche deposits suggesting that cementation has taken place in multiple episodes since MIS-9a. Neotectonics of Sierra de la Sobia are expressed in subtle changes in relief after extremely rapid coseismic events, with average recurrence intervals much longer than the time covered by the regional historical and instrumental period.

1 **Gravitational slope processes triggered by past earthquakes on the Western**
2 **Cantabrian Mountains (Sierra de la Sobia, Northern Spain)**

3 Francisco José Fernández ^{*a}, Rosana Menéndez-Duarte ^a, Luis Pando ^a, Laura
4 Rodríguez-Rodríguez ^b, Miguel Iglesias ^a

5 ^a Departamento de Geología, Universidad de Oviedo, c/ Jesús Arias de Velasco s/n,
6 33005 Oviedo, Asturias, Spain.

7 ^b Departamento de Ciencias de la Tierra y Física de la Materia Condensada, Universidad
8 de Cantabria, Av. Los Castros s/n, 39005 Santander, Spain.

9 ^{*}Corresponding author. E-mail address: fjfernandez@uniovi.es

10 **Abstract**

11 Sierra de la Sobia is a linear mountain range of arcuate shape, located West of the
12 Cantabrian Mountains. The long-lived crustal León Fault runs along its western hillslope,
13 and its trace is partially covered by multiple rock-avalanches. Here we discuss if recurrent
14 paleo-earthquakes in the M₆+ range could have acted as the triggering factor for rock-
15 avalanches in a region where the historical and instrumental seismic records only include
16 seismic events up to M_s 4.6. Evidence concurring with a coseismic origin includes: (i)
17 kinematic of current minor transverse and parallel faults to Sierra de la Sobia being
18 consistent with a horizontal North-South compression of the Cantabrian Arc; (ii) slopes
19 of the depletion zones that would become unstable if horizontal seismic ground rose 0.10–
20 0.15 g; and (iii) block size-reduction by dynamic fragmentation creating block size
21 distribution with fractal dimension, ranging between 2.24 and 2.70. U/Th dating of seven
22 calcite precipitates coating the blocks of cemented rock-avalanche deposits suggesting

23 that cementation has taken place in multiple episodes since MIS-9a. Neotectonics of
24 Sierra de la Sobia are expressed in subtle changes in relief after extremely rapid co-
25 seismic events, with average recurrence intervals much longer than the time covered by
26 the regional historical and instrumental period.

27 *Keywords:* Rock-avalanche; U/Th dating; Quaternary tectonics; Cantabrian Mountains;
28 Northern Iberia plate, paleo-seismicity.

29 **1. Introduction**

30 The Cantabrian Arc (CA), also known as Ibero-Armorican Arc (Lefort, 1989), is the
31 largest structure of the Variscan orogeny in Western Europe. The CA deformed an
32 initially linear foreland thrust and fold belt, formally defined as the Cantabrian Zone (CZ;
33 Lotze, 1945) in the latest Stephanian to the earliest Permian (Weil et al., 2001). Later, the
34 CA also controlled the reactivation of the basement during the Alpine cycle, when the
35 Cantabrian Mountains were raised (Gallastegui et al., 2016). Alpine deformation
36 produced the inversion of the northern Iberian plate, and it migrated and decreased
37 progressively from the Pyrenees, westward to the CA (Fig. 1A). Alpine sedimentation
38 ceased after the Late Oligocene (Álvarez-Marron et al., 1997), and Alpine exhumation of
39 the central part of the Cantabrian Mountains occurred from 39 to 29 Ma, at a rate of 2.4–
40 3 mm yr⁻¹ (Fillon et al., 2016). Little is known about the post-Oligocene tectonics of the
41 Cantabrian Mountains due to the scarcity of Tertiary outcrops, the limited size of surficial
42 formations formed since the late Quaternary glaciations, and the later slope dynamics
43 controlled by fluvial incision (Menéndez-Duarte et al., 2007; Rodríguez-Rodríguez et al.,
44 2015). Consequently, we might wonder if evidence of Quaternary deformation exists in
45 the Cantabrian Mountains, and what traces correspond to active landscape processes.

46 Nowadays, northern Iberia is considered a passive margin, hundreds of kilometres away
47 from the interaction of the Nubia Plate with the Iberian microplate. This overall tectonic
48 setting engenders a stress field in the Iberian Peninsula, characterized by a predominately
49 NNW to NW trending maximum horizontal stress (SHmax; [de Vicente et al., 2008](#);
50 [Custódio et al., 2015](#)). In this context, the Cantabrian Mountains are considered a
51 seismically active shallow crust ([Delavaud et al., 2012](#)) with earthquakes of low to
52 moderate magnitude ([Stich et al., 2020](#)). During the 2015–2017 instrumental period, the
53 CZ recorded 40 seismic events of surface wave magnitude (M_s)>2 at depths of between
54 9 and 18 km at the intersection between the León and Ventaniella faults and the biggest
55 recorded was an M_s 3.7 event (Fig. 1B; [López- Fernández et al., 2018](#)). The León Fault
56 is a breaching fault ([Alonso et al., 2009](#)) buckled by the CA, and cut northwards by the
57 younger Permo-Triassic right-lateral Ventaniella Fault. Large submarine avalanche
58 deposits have recently been found, along with the northwest offshore extension of the
59 Ventaniella Fault-scarp ([Fernández-Viejo et al., 2014](#)), near to the location of the
60 historical earthquakes of 1522 and 1861 (Fig. 1B). East-west trending uplifted wave-cut
61 platforms extend along the Cantabrian coastline for more than 400 km, tectonically
62 uplifted since at least 1–2 Ma ([Álvarez-Marrón et al., 2008](#)).

63 These tectonic geomorphology imprints might result from the ongoing slow convergence
64 and inversion extending along the Cantabrian coast, where the CA may reactivate. To test
65 this hypothesis, we studied the recent tectonic geomorphology of Sierra de la Sobia, a
66 Carboniferous limestone mountain range of arcuate shape, buckled according to the
67 curvature of the CA to the west of the Ventaniella Fault. The northern branch of the León
68 Fault lies along the western flank of Sierra de la Sobia (Figs. 1B and 1C), and an unusually
69 high number of rock-avalanches never previously described or analysed overlie the fault
70 trace. In 1996 an earthquake of M_s 4.1 (Fig. 1B) struck the Villa de Sub village on the

71 southern slope of Sierra de la Sobia, triggering a rock-fall. North-westward, El Canto
72 district was built atop the most massive rock-avalanche, composed of several superposed
73 deposits. The higher parts of this avalanche still represent a severe risk for the citizens of
74 Entrago and La Plaza. Moreover, an early cemented deposit accumulated about 600 m
75 east of Sobrevilla has its origin in a rockfall from the deposit. The number of tension
76 cracks easily visible on Google Earth suggest that more rockfalls are likely to happen. In
77 addition, a reverse fault superposing Carboniferous limestone onto cemented talus scree
78 deposits has also been described (Fernández et al., 2018). At first sight, Sierra de la Sobia
79 is among the best places to shed new light on the Quaternary tectonic geomorphology in
80 the CZ.

81 **2. Regional setting**

82 Sierra de la Sobia is in the eastern nappe of the Somiedo Unit (Figs. 1B, C; Alonso et al.,
83 2009). From a geomorphological standpoint, it is an arcuate mountain range ~16 km long
84 and 2-5 km wide with a Range Level of Summits (RLS) dipping 1.5° northward (Figs. 2,
85 3, 4 and 5). It is formed by a continuously well-exposed outcrop of Carboniferous
86 limestone. The highest elevations of these mountains are south of Sierra de la Sobia, at
87 the Ubiña Massif with peaks 400 m higher than the regional-RLS. It is noteworthy that
88 the León Fault is bent around the Ubiña Peak (2417 m), accordingly with CA orocline
89 and such a footwall corner gives relief to a syntaxial shape (Fig. 2). Carboniferous
90 limestone overrides the Lower Cretaceous cover south of the Ubiña Peak, evidencing the
91 Alpine reactivation of the León Fault (Alonso et al., 2007). The long-lived León Fault has
92 been active in different tectonic cycles, and it remains seismically active (Fig. 1B;
93 López- Fernández et al., 2018).

94 **2.1 Variscan structure**

95 The Paleozoic basement of the Sobia Nappe involves an ~2500 m and a 500 m-thick syn-
96 orogenic sequence (Fig. 3; Marcos and Pulgar, 1982). During the Variscan orogeny the
97 oldest thrusts, such as the Sobia, Tameza, and Somiedo, accommodated most of the
98 shortening in deep levels (Figs. 1C and 3). Upwards, the shortening was accommodated
99 stratigraphically by fault-propagation folds, like the Caranga Antiform (Figs. 3 and 4B;
100 Bulnes and Aller, 2002). It consists of a stack of at least three thrusts of Ordovician
101 quartzite and sandstone formed to facilitate accommodation for shortening northwards
102 due to the presence of lateral thrust ramps (Bastida and Castro, 1988).

103 Later, the León Fault cut the sequence, superposing the Somiedo and the Tameza Nappes
104 onto the Sobia Nappe (Fig. 1C). The primary displacement of the León Thrust occurred
105 before the CA, and kinematic markers indicate an ENE transport direction (Alonso et al.,
106 2009). Since the CA bends the León Fault, it trends along with two main strikes N30°W
107 and N100°E, respectively, from the Ubiña Massif (Fig. 2). Its North-Western termination
108 consists of a splay fault formed by three main segments. The Marabio Segment-Fault
109 (MSF; Figs. 1C, 2, 4) is the longest at 48 km, its trace being partially covered by rock
110 avalanches triggered along the western flank of Sierra de la Sobia.

111 **3. Materials and methods**

112 The geology of Sierra de la Sobia was entirely reviewed based on the latest regional study
113 (Alonso et al., 2009) and **the analysis of** previous geological maps of the northern and
114 eastern areas (Bastida and Castro, 1988; Bulnes, 1994), and the online version of the
115 continuous digital geological map of the CZ, scale 1:50,000 (Merino-Tomé et al., 2011).
116 This map differentiates the unconformable Quaternary, Tertiary, and Stephanian outcrops
117 from the Paleozoic underlying basement, as well as the Variscan mechanical contact from
118 the latterly developed structures (Fig. 3). Quaternary deposits and fracture networks
119 within the limestone massif have been tracked from fieldwork and ortho-photographs,

120 scale 1:50,000 (PNOA series, IGN). Due to the difficulties inherent to discriminating
121 Quaternary faults from other earlier Cenozoic faults, both have been grouped as “late
122 faults” when cut-off relationships with the earlier Variscan faults can be established.
123 However, most of these later faults do not show relative displacements at our working
124 scale, because fault slips are frequently <10 m.

125 A selection of nine rock-avalanches was quantitatively characterized. The vertical drop
126 (H) measures the difference in height between the crown of the depletion zone and the
127 toe of the accumulation body, and the length (L) is the horizontal distance between both
128 points. The rock-avalanche volume was estimated multiplying its surface area by the
129 mean thickness of the accumulation body. The average thickness of rock-avalanche
130 deposits was indirectly estimated as half of the possible maximum thickness of the
131 deposit, calculated from the topographic expression of the accumulation body.

132 Analyses of Block Size Distribution (BSD) were completed in four representative
133 deposits of rock-avalanches using high-resolution drone imagery to compile maps of
134 block sizes >10 cm. Ortho-photographs were acquired from a drone, ATYGES FV-8,
135 using pre-planned flight lines of the mapped areas and geo-referenced with a GPS,
136 LEYCA GS14 GNSS. The fractal dimension (D , Epstein, 1947) was calculated in such
137 deposits easily, using the BSD of >14k blocks as the slope of the lineal fit in log
138 frequency/log equivalent radius diagrams; they were plotted showing 20 bins per order
139 of magnitude. The shape parameter S calculated as $S = \frac{4\pi A}{P^2}$ (1) (Fernández et al., 2005),
140 where the area A and perimeter P of wedges were measured in pixel² and pixel,
141 respectively. Wedges <20 pixel² were removed. S is not wedge-size dependent, and
142 ranges between 1 (wedge-shape is a perfect circle) and 0 as irregularities of the wedge-

143 shape increase. Block size measures by the radii equivalent (r_i) of each block, where $r_i =$

144 $\sqrt{\frac{(A+P)}{\pi}}$ (2).

145 The rock mechanics of the residual slope were analysed where the rupture scarps were
146 mapped. Slope stability was calculated based on over 350 measurements of joint and fault
147 plain orientations using the advanced computational tools for geometrical, kinematical,
148 and mechanical analysis of the Dips 7.0, Rocplane, and Swedge programs, respectively.

149 Mechanical discontinuities were heuristically classified as: (i) bedding planes (S_0); (ii)
150 faults parallel (F_p) or transverse (F_r) to the range trend; and (iii) joints parallel (J_p) or
151 transverse (J_r) to the range trend. Joints transverse to the range were subdivided according
152 to the direction and angle of dip in: (i) $<30^\circ$ dip angle northwards (J_{r1}); (ii) $>50^\circ$ angle
153 northwards ($J_{r1'}$); (iii) $<30^\circ$ dip angle southwards (J_{r2}); (iv) $>50^\circ$ angle southwards ($J_{r2'}$).

154 Calcite cements, interfusing blocks and pebbles in the oldest rock-avalanches were
155 collected at eight sampling localities and treated in the laboratory to extract the calcite for
156 U/Th dating. Five of the eight samples processed exhibited calcitic cement pure enough
157 for radiometric analysis. Calcite crystals were selected under the microscope to minimize
158 detrital contamination from detrital fine sediment matrix. U/Th dating was completed at
159 the University of Minnesota by Inductively Coupled Plasma Mass Spectrometry (ICP-
160 MS) as described by Shen et al. (2002). Sample RB_02 was replicated by sample RB_9
161 and sample RB_03 by sample RB_10 by the U/Th facility at the Institute of Earth
162 Sciences Jaume Almera (ICTJA-CSIC; Barcelona). The replicates provided purer calcite
163 cements which reduced the age uncertainties previously obtained, likely due to a Th
164 excess of detrital origin. The chemical separation and purification of the radioisotopes
165 followed Bischoff et al. (1988). The isotope electrode position followed Talvitie (1972)

166 and was modified following Hallstadius (1984). Age calculations were based on
167 Rosenbauer (1991). Results are compiled in Table 3.

168 **4. Results**

169 Three structural domains have been distinguished in Sierra de la Sobia. The northern
170 domain extends southward to the Marabio Mountain Pass. The MSF outcrops within the
171 Westphalian shale, superposing the Teverga coal basin (Middle and Upper Westphalian
172 formations in Figs. 3 and 4) onto the Sobia Nappe. The Tameza Thrust and MS converge
173 progressively northwards (Fig. 3). The western hillslope of Sierra de la Sobia is separated
174 by >1 km of MS-trace (Fig. 4B), and it lacks rock-avalanches. Minor parallel faults trend
175 NNE, and transverse faults define three sets trending NE, E, and SE. A reverse parallel-
176 fault superposes Carboniferous limestone westward onto recently cemented talus-scrree
177 deposits, with up to 6 m net slip (Fernández et al., 2018). A fault splay also cuts the
178 Caranga fault-propagation anticline (Figs. 3, 4B, and 6). It shows a reverse displacement
179 with anticlockwise rotation from SW to S. The kinematic agrees with the Alpine
180 inversion, but also with the NNW-trend of the current regional SHmax. The stress
181 inversion obtained for Sierra de la Sobia, after excluding some of the latest transverse
182 fault kinematics that gave inconsistent solutions, gives a similar SHmax, and the
183 limestone outcrop has a joint fracture network with similar strikes to faults belonging to
184 this domain (Fig. 6).

185 The hinge domain extends southward from Marabio Pass to Sobrevilla (Fig. 3). The
186 arcuate MSF-trace lies progressively closer to the western hillslope of Sierra de la Sobia.
187 The slope has a convex shape and has recorded several rock-avalanches. The limestone
188 outcrops' width decreases progressively as the curvature of the arcuate range increases
189 (Fig. 3). Deformation has been accommodated by normal faults that transect the hinge of
190 the range, some of them cut MSF. Southward, MSF is covered by the Entrago rock-

191 avalanche. The outcrop of limestone is strongly fractured, and the fracture network is
192 formed by joint sets parallel to the main fault strikes (Fig. 6).

193 The southern domain extends from the Entrago to the Villa de Sub rock-avalanches (Fig.
194 3). The South-Western hillslope of the range between the Entrago and the Carrea rock-
195 avalanches is a structural form controlled by the orientation of the limestone bedding and
196 MSF. Both mechanical discontinuities run parallel to the slope, and dip in the same
197 direction but are more pronounced than the slope. Parallel faults run SE, with transverse
198 faults and fractures defining three sets trending N, NE, and E, respectively (Fig. 6). The
199 periclinal structure of the Sobia Nappe is exposed on the southern hillslope of Sierra de
200 la Sobia (Fig. 3). The structure consists of folds related to Variscan thrusts in the lateral
201 ramp of the Sobia Nappe and with a transport direction north-eastward. The León Fault
202 thrusts out of sequence towards the NE and accumulates a total displacement of ~9 km in
203 the section shown in Fig. 1C (Alonso et al., 2009). This lateral ramp was shifted 45°NW
204 during the Alpine inversion.

205 More recently, the current re-tightening of the Sobia Nappe was accommodated by right-
206 lateral faults (N150°E-strike). The trace of these faults runs parallel to the Taja Fault
207 segment throughout the southern hillslope of Sierra de la Sobia. Additionally, several
208 active faults trending E-W have exposed their respective fault scarps and have been
209 mapped on the junction of the splay between the Trobaniello Fault segment and the MSF.
210 Most of them are small (widths <7 km) with relative movement frequently attenuated
211 laterally and accommodated by the thickly fractured surficial network of the limestone
212 massif (Fig. 6).

213 Restoration of an eventual continuous RLS-line before its segmentation along the
214 northern and hinge domains of the range results in an extension of ~300 m southward by
215 right-lateral faults N150°E-strike, and potentially by faults trending E-W (Fig. 6). The

216 current re-tightening of the arc described by the hinge domain of Sierra de la Sobia has
217 been measured, assuming that the extension of the western convex hillslope was created
218 by tangential longitudinal folding (Ramsay, 1967). The finite neutral surface is on
219 longitudinal section A (Fig. 3) and runs along the RLS (Fig 4). The result is an
220 incremental longitudinal strain $e_l = 0.031$ that produces a strain ellipse on the outer arc of
221 aspect ratio $R = 1.42$ (Fig. 6), therefore an angular extension of 3.32° along the western
222 convex hillslope. However, the kinematics of the current faults suggest that the parallel
223 shear could be progressively more significant toward the northern and southern domains
224 respectively, according to the orientation of their finite strain ellipses (Fig. 6).

225 **4.1. Rock-avalanche geometry**

226 Multiple rock-avalanche deposits are within the hinge and southern domains of Sierra de
227 la Sobia (Figs. 3 and 6). The largest occurred on the south-western hillslope, and the
228 smallest on the southern hillslope of the mountain range. Frequently, rock-avalanches
229 result from the superposition of multiple destabilizing events. Rock-avalanches in the
230 vicinity of Villa de Sub could have been triggered by a recent re-activation of the right-
231 lateral faults of N150°E-strike (Fig. 6).

232 The geometry and volume estimated for the nine selected rock-avalanche deposits were
233 compared with their respective source areas (Table 1). All these proxies have a reasonable
234 correlation. Avalanches with deposit-volumes $>3 \times 10^6 \text{ m}^3$ have similar vertical drops of
235 $\sim 0.7 \text{ km}$ on average, whereas avalanches with deposit-volumes $<3 \times 10^6 \text{ m}^3$ have lower
236 vertical drops. Assumptions used in the estimation of areas and volumes result in both
237 being undervalued. This misrepresentation is significant for the source area because the
238 rupture surfaces are usually on high, steep hillslopes. For instance, the rupture scarp of
239 Cueva Güerta is above vertical crags at the outlet of the Páramo River canyon (cross-
240 section D, Fig.4). A maximum depth of $\sim 65 \text{ m}$ has been measured at this deposit,

241 anomalously high compared to other deposits due to its confinement between the crags
242 of the Páramo River canyon (Table 1; Fig. 3). Geometrical features of the most
243 representative rock-avalanches have allowed the distinguishing of two types relative to
244 size. A detailed analysis of BSD and rock slope mechanics are presented for the rock-
245 avalanches of the Entrago and Carrea (largest) and the Villa de Sub and Cueva Güerta
246 (smallest).

247 **4.2. Structural control and BSD analysis of selected rock-avalanches**

248 The Entrago rock-avalanche is at the boundary between the hinge and southern domains.
249 Its source area lies between 800 and 1100 m above the villages of Entrago and La Plaza
250 (Fig. 7). Rock-slope failure occurred by direct toppling and planar slides, triggered in
251 multiple events. Roughly mapped rupture scars define a triangular planar surface of ~70
252 ha dipping 68° toward $N71^\circ W$. The crown of the avalanche is bound by a right-lateral
253 fault $N19^\circ E$ -strike (Fig. 8). The southern fault tip has 72 m of horizontal strike. The
254 conical accumulation zone (40.75 ha) extends down to the Teverga River. It slopes to
255 $\sim 47^\circ NW$ and the landslide accumulation consists of four superposed minor deposits: an
256 earth flow overlaid by three conic bodies of block accumulations (early, middle, and
257 recent) that still preserve their transverse ridges (Fig. 7). The fracture pattern mapped in
258 the depletion zone of this rock-avalanche (Figs. 6 and 7) allowed the outlining of 612
259 wedges (Fig. 9). A bi-modal BSD is observed, with two size-fractions of wedges. The
260 fine fraction includes wedges with diameters of <20 m, mostly on the rock-buttress failure
261 and usually of triangular shape. However, a large proportion of wedges are rhomboidal.
262 The major axis of the rhomboids is parallel to the active fault ($N19^\circ E$ -strike). In contrast,
263 the wedges of the fine fraction show an anticlockwise rotation (Fig. 9B), with uniform
264 dispersion onto the rupture slope. Rotation is a consequence of the slight obliquity
265 between the wedge orientation and the rupture plane (Fig. 10). The diagram of S against

266 the wedge eccentricity shows small differences between both fractions (Fig. 9C). Wedges
267 of eccentricity 2.5 have $S=0.64$ if triangular or $S=0.46$ when rhomboidal. Wedges run out
268 from the depletion zone, and consequently their roundness tends to increase as indicated
269 by parameter S and their eccentricity. Diagram C (Fig. 9) shows both effects, the
270 difference in shape of each fraction size, and the effect of incipient sliced wedges within
271 the unstable residual relief.

272 The total range of block size r_i is <10 cm to >10 m. However, pebbles <20 cm were not
273 considered in the analysis because of their unrealistic statistical significance. The size
274 distribution of 4805 blocks (the total outlined blocks within the accumulation zone) is
275 presented in a frequency histogram of the normal distribution (Fig. 11A). BSD is not
276 fractal, with a slope change in the best fit regression line of the corresponding log
277 (frequency)-log (radius) histograms at block radius $r_k \sim 1$ m (Fig. 11B). The block sizes
278 $r_k > 1$ m yield $D=2.35$, the usual fractal dimension of limestone fault-rocks and the damage
279 zone of strike-slip and extensional fault zones (Storti et al., 2003). Conversely, the block
280 sizes $r_k < 1$ m yield $D=1.42$, a value frequently observed in small grain size fractions of
281 cataclastic fault rocks (Keulen et al., 2007). Both have an eccentricity of ~ 1.9 and yield
282 $S \sim 0.65$ ($r_k > 1$ m) and $S \sim 0.68$ ($r_k < 1$ m; Fig. 12B), accordingly with increasing block
283 roundness. A comparative BSD analysis between the three overlapped bodies has allowed
284 us to understand the specific contribution of each rock-avalanche outbreak to the total
285 BSD. ~ 1400 blocks in each body were analysed, and all show normal distributions (aspect
286 ratio ~ 0.7). It therefore follows that the early deposit yields a D value that compares better
287 than the latest rock avalanches with the BSD of the total accumulation zone (Fig. 11C).
288 Moreover, D appears time dependent. So, the fractal dimension in large blocks reduces
289 as the relative age of the deposit increases (Fig. 11D-F). Consequently, BSD becomes
290 fractal in the early deposit because the slope rupture at r_k is highly attenuated (Fig. 11F).

291 South of the Entrago rock-avalanche, there are two accumulation bodies of limestone
292 blocks above the villages of Sobrevilla and Carrea, between 650 and 1200 m (Figs. 7, 12
293 and 13). They correspond to medium sized rock-avalanches (Table 1). The current active
294 right-lateral faults that triggered both avalanches are trending NNE and NE respectively,
295 and their kinematics are accommodate the extension along the outer arc as the curvature
296 of the mountain range increases (Fig. 6). These faults create a downthrown block with
297 200 m of maximum vertical slip (longitudinal section A in Fig. 4) with maximum strike
298 separations raised in their respective southern tips. Both faults displace the MSF trace,
299 which cut out of sequence an earlier Variscan thrust, possibly the Tameza Thrust (Fig.
300 1C). The early cemented deposit accumulated about 600 m east of Sobrevilla has its origin
301 in a rockfall (Fig. 13). The number of tension cracks easily visible on Google Earth
302 suggest that more rockfalls are likely to happen.

303 The southern hillslope of Sierra de la Sobia presented three small rock-avalanches: Villa
304 de Sub, Sabariegos, and Busbigre (Table 1). The structure consists of an asymmetric
305 cuscate-lobate anticline-syncline of N-shape folding related to two faults (Fig. 3 and
306 cross-section D in Fig. 4). The Sobia Syncline is a Variscan fault propagation fold related
307 to the Sobia Thrust and then thrust out sequence by the León Fault toward the NE (Fig.
308 4; Alonso et al., 2009). The cuscate anticline is an ESE-verging fault-propagation fold
309 related to a small back thrust that crops out upslope of Villa de Sub (Fig. 14). The structure
310 probably formed to accommodate the tightening within the MSF footwall (Fig. 15 and
311 cross-section D in Fig. 4). Since the Alpine inversion, the structure of the southern domain
312 tilted northward $\sim 30^\circ$. The occurrence of small rock-avalanches seems to be related to
313 Quaternary deformation. The rock-avalanches are controlled by penetrative vertical
314 planes (J_{p1}) trending N125-150°E, parallel to the general trend of the most significant
315 structures (Fig. 3). Some fractures have sub-horizontal slickenlines according to right-

316 lateral kinematics (F_{p1}), and they control the rupture scarps of rock-avalanches. Such local
317 kinematics are consistent with the whole kinematic model proposed for Sierra de la Sobia
318 (Fig. 6). The main accumulation of the Villa de Sub rock-avalanche has three overlapped
319 deposits, with the lowest composed of calcite-coated limestone blocks. The middle and
320 upper deposits have two overlapped fans. Additional blocks were incorporated during the
321 last instability events with little change in the fan shape (Fig. 15A): a rock-fall triggered
322 in 2004, synchronously with an earthquake of Ms 2; and a co-seismic 4.1 Ms rock-fall in
323 1996 (Fig. 1B). BSD of the Villa de Sub rock-avalanche is not fractal, with a slope change
324 also at block radius $r_k \sim 1$ m (Fig. 12A). The block sizes $r_k > 1$ m yield $D=2.53$ ($R^2=0.92$ to
325 the fitted regression line). Conversely, the block sizes $r_k < 1$ m yield $D=1.25$ ($R^2=0.98$).
326 Both sizes have similar low eccentricity of ~ 1.6 and roundness of $S \sim 0.73$ (Fig. 12B)
327 respectively, with a relatively lower vertical drop of rock-fall and a lower impact
328 compared to larger rock-avalanches (Table 1).

329 Finally, a small rock-avalanche located at the northern entrance of Cueva Güerta at the
330 spring of Foz de la Estruchura has been analysed in detail. Most accumulation bodies
331 triggered along this canyon are confined by two opposite facing crags that bound the
332 narrow course of the river. Both the cave conduits and the river course lie parallel,
333 trending N-S along the damage zone of the MSF (Fig. 14). BSD in the accumulation body
334 of Cueva Güerta is not fractal, with a slope change also at $r_k < 1$ m (Fig. 12A). The block
335 sizes $r_k > 1$ m yield $D=2.70$. Conversely, the block sizes $r_k < 1$ m yield $D=0.54$, but with low
336 confidence. Both sizes have a low eccentricity of ~ 1.6 , but the coarse fraction includes
337 less rounded blocks ($S \sim 0.68$), than the finer fraction ($S \sim 0.72$). The coarse fraction has the
338 highest D among the populations analysed in Sierra de la Sobia. It shows lower particle
339 fragmentation (higher D) than the other unconfined accumulation bodies. Low

340 fragmentation is consistent with a progressive increment of relatively fine blocks towards
341 the top of the confined accumulation, caused by gravity selection.

342 **4.3. Slope stability analysis**

343 The stability models for all the slopes analysed assumed a conservative friction angle of
344 35° on the joint surfaces. The slope stability above the Entrago rock-avalanche was
345 analysed based on the orientation of 85 fractures measured along the rupture scarp,
346 controlled by the right-lateral fault of N19°E-strike. The mechanical instability of the
347 rupture scarp was evaluated under different dynamic failure modes (Fig. 10). Visual
348 estimates indicate <6% risk for planar sliding, <16% direct toppling risk for joint sets J_{r1} ,
349 and J_{r2} , <16% flexural toppling risk for joint sets J_{r1} and <13% wedge sliding risk.
350 Although the dynamic analysis gives a low risk of instability, the slope records at least
351 four superposed landslide deposits (Fig. 7). The models have a slope safety factor of <1.3
352 only when running with horizontal peak ground accelerations (PGA)>0.10-0.15 g, within
353 the prediction of the 2013 European Seismic Hazard Map for north-western Iberia
354 (Giardini et al., 2014).

355 84 mechanical discontinuities (25 S_0 , 3 F_r , 1 F_p , 23 J_p , 18 J_{r1} , 6 J_{r1} , 6 J_{r2} and 2 J_{r2})
356 measured on the rupture plane of the Carrea rock-avalanche have been considered for the
357 slope stability analysis. The fracture pattern lies parallel to both the Variscan thrusts and
358 an active transverse fault, and a rupture slope with dip direction 237/50 is considered for
359 the stability models. Considering these surface conditions there is a 0% risk for flexural
360 toppling, <4% risk for planar sliding, <11% risk for direct toppling and wedge sliding.
361 All these models indicate slightly higher safety factors than for the Entrago rock-
362 avalanche, even though a safety factor of <1.3 may arise with horizontal PGA>0.15 g.

363 123 mechanical discontinuities (45 S₀, 1 F_r, 7 F_p, 35 J_p, 23 J_{r1}, 8 J_{r1'}, 1 J_{r2} and 3 J_{r2'})
364 measured on the rupture plane of Villa de Sub were considered for the slope stability
365 analysis. A penetrative fracture pattern lies parallel to the active right-lateral fault and
366 normal to the S₀ trend. The rupture slope modelled has a 173/80 dip direction and tilts
367 opposite to S₀. The dynamic analysis gives risks of <8% for flexural toppling, <9% for
368 planar sliding, <24 % for direct toppling and <19% for wedge sliding. The models
369 provided lower safety factors than for the Entrago rock-avalanche, even though a safety
370 factor of <1.3 may arise with horizontal PGA>0.10 g.

371 Only a dynamical slope stability analysis has been carried on the external Cueva Güerta
372 avalanche. 52 discontinuities (5 S₀, 8 F_r, 18 F_p, 6 J_p, 9 J_{r1}, 1 J_{r1'}, 4 J_{r2}, and 1 J_{r2'}) measured
373 around the north cave entrance were considered in the slope stability analysis. Two planes
374 with dip directions 20/90 and 87/90 define the rupture slope, and consequently two
375 dynamic analyses of the respective slope stability risk have been considered. These
376 indicate risks of <14 and 25% for flexural toppling, <8 and 14% for planar sliding, <21
377 and 27% for direct toppling, and <24 and 26% for wedge sliding, with dip directions
378 20/90 and 87/90 respectively. Slope stability models created with the dip direction 87/90
379 give lower safety factors than those for 20/90. Both models have lower safety factors than
380 any other rock-avalanche case studies, even though >1.3 has been obtained for all rupture
381 slopes modelled in this work.

382 **4.4. Timing of rock-avalanche events**

383 Calcite coating the blocks within the oldest calcareous rock-avalanche of the Entrago
384 deposit was successfully dated in samples RB_5, RB_6, and RB_7 (Fig. 7, Table 2).
385 Samples RB_5 and RB_6 taken along the transverse frontal ridge of the conical cemented
386 deposit, yielded ages of 13.7±0.9 and 278.3±32.9 ka coeval to marine isotope stages MIS-

387 1 and MIS-9a, respectively. Sample RB_7 from the toe of the deposit, yields 194.3 ± 70.2
388 ka, indicating cementation during MIS-7a.

389 In the case of the Sobrevilla deposit, a minimum U/Th age of ~ 100 ka has been reported
390 (Fig. 13; Rodríguez-Pérez, 2012). Sample RB_2 taken at the accumulation body of the
391 Carrea avalanche yields an age of 58.8 ± 14.6 ka, coeval to MIS 3-4 (Table 2), while RB_9
392 yields a minimum age of 38.3 ± 2.8 ka, coeval to MIS 3 (Table 3). Based on the U/Th
393 dates, the Sobrevilla rock-avalanche occurred earlier than the Carrea rock-avalanche, but
394 later than the main event that caused the Entrago rock-avalanche. Radiometric ages are
395 consistent with the evolution of the BSD observed between the three overlapped deposits
396 in the avalanche. So, the Carrea rock-avalanche has BSD with a sharper slope break than
397 the Entrago one (Fig. 12A). The blocks within the accumulation body are also more
398 irregular than those in the Entrago avalanche, as shown by parameter S (Fig. 12B).

399 Sample RB_03 taken from a calcite cement coating a block at the Cueva Güerta rock
400 failed to provide a reliable age (Table 2). A replica of that sample, RB_10, yields a
401 minimum age of 9.9 ± 1.2 ka (Table 3). Based on the U/Th results, Cueva Güerta is the
402 youngest dated rock-avalanche until now in Sierra de la Sobia. Its bi-log frequency-size
403 diagram shows a greater slope rupture between the two block fractions (Fig. 12A).
404 According to the tendency observed between the diagrams in the Entrago rock-avalanche
405 (Figs. 11D, E, and F), the slope rupture (Fig. 12A) is also consistent with the young age
406 obtained in the Cueva Güerta avalanche.

407 **5. Discussion**

408 The impact of our results is discussed below, addressing the following: 1) current
409 tectonics in Sierra de la Sobia; 2) origin and recurrence of rock-avalanches; 3) Quaternary
410 geomorphological evolution of the landscape.

411 **5.1 Current tectonics in Sierra de la Sobia**

412 The kinematic analysis of active faults, as well as their slip inversion, is consistent with
413 a re-tightening by horizontal shortening accordingly with a N-S trending SH_{max} (Fig. 6).
414 Current strain gave rise to the stretching along the western outer arc of the range,
415 throughout the activation of strike-slip faults but also reverse and minor normal-scissor
416 faults that accommodate deformation at the surface. In contrast, at depth, this intensely
417 fractured zone is probably linked to the León Fault as indicated by the fracture network,
418 the fault trends and their distribution compared to the trace of the León Fault. However,
419 some of the minor active faults also displace the main trace of the León Fault (Figs. 3 and
420 4). These structural features might raise questions about the current activity of this fault.
421 However, we have observed that current tectonics related to the León Fault likely
422 triggered the slope failures recurrently, both in the outer arc of Sierra de la Sobia and
423 along the whole southern branch of this fault (Figs. 1B and 2). Moreover, several low
424 seismic signals have recently been recorded at a depth of ~15 km near the intersection of
425 the León and Ventaniella Faults (López- Fernández et al., 2018). Therefore, we consider
426 that the most recent minor faults showing cut off relationships with the León Fault trace
427 are a consequence of the growth fracture density along the main fault trace and the
428 dissipation of the current differential stress along such new fault planes.

429 The summit elevation in Sierra de la Sobia progressively increases southwards, showing
430 a constant slope of 1.5° from 1350-1776 m (Saleras peak; Figs. 2 and 5). The restored
431 section A (Fig. 4) has given a maximum current extension of 300 m of the outer arc of
432 the range. The progressive uplift of the range southward led to the reactivation of the
433 Variscan lateral ramp and the development of several high angle faults trending E-W at
434 the junction between the MSF and the Trobaniello segment fault (Fig. 6). Finally, the
435 current brittle strain partition in the southern domain of Sierra de la Sobia accommodated

436 right-lateral minor faults N150°E-strike as well as other conjugated faults that likely
437 caused smaller avalanches (Fig. 6). The larger avalanches triggered northward suggest
438 that Quaternary seismicity is higher in the hinge domain of Sierra de la Sobia and
439 diminishes southward.

440 It is reasonable to extend the current tectonics of Sierra de la Sobia to CZ, as a working
441 hypothesis. Because this arcuate mountain range lies parallel to the León Fault, the fault
442 trace eastward prolonged according to CA orocline (Fig.1), and along the whole trace of
443 the León Fault has recorded rock-avalanches and complex flows like those described
444 above (Fig. 2). Moreover, CZ has other active structures that support this statement. One
445 is the Variscan Tineo Thrust, westward of the Cenozoic basin of Oviedo. This trends NE-
446 SW accordingly with the CA, and it was reactivated, thrusting over Cenozoic sediments
447 south-eastward (Fig. 1B; Pulgar et al., 1999). Another case is the Boinás Thrust (Fig. 1B;
448 de Vicente Muñoz et al., 2007). It trends parallel to the Tineo Thrust but back thrusts
449 north-westward 350 m. The Tineo Thrust and the reverse fault described in the Marabio
450 Pass (Fig. 6; Fernández et al., 2018) have the same kinematics. In both cases, tectonics
451 seem to accommodate the deformation after the unfolding limb section of regional
452 Variscan folds parallel to the CA by horizontal shortening parallel to their respective axes
453 accordingly with the regional trends of SH_{max} (de Vicente et al., 2008; Custódio et al.,
454 2015). Eastward, the fault junction between the León and Ventaniella faults (Fig. 1B)
455 recorded recent low-magnitude earthquakes (López- Fernández et al., 2018). The
456 clustering of earthquakes along these faults coincides spatially at depth with the transition
457 zone. The seismicity of the Ventaniella fault is fragmented, having only moderate seismic
458 records at the northern onshore segment and south of the fault's junction, whereas the
459 central segment is aseismic.

460 CA is divided into two tectonic units by the Ventaniella Fault. The current deformation
461 in the western tectonic unit appears controlled by the arcuate shape of the orocline.
462 Normal faults accommodate stretching, parallel to the arc. Strike-slip faults transverse to
463 the arc accommodate the N-S shortening, and back-thrusts towards the outer-arc
464 accommodate the subsequent migration of the neutral surface predicted for the
465 longitudinal tangential folding mechanism (Fig. 1B). Variscan and Alpine structures east
466 of the Ventaniella Fault have a linear trend E-W and they can accommodate the current
467 regional SH_{max} easily with straight displacement southward. However, because the CA
468 controls the Quaternary reactivation, deformation is partitioned in transtensive basins
469 controlled by right faults trending NW-SE parallel to the Ventaniella Fault. Finally,
470 according to the crustal thickness variation, the aseismic central segment might be
471 interpreted as the current strain rate, progressing more efficiently toward the flanks of the
472 orocline than in its core (Díaz et al., 2016; Díaz and Gallart, 2009).

473 The topography of the crust-mantle boundary is also interpreted as evidence of a passive
474 margin (Cadenas et al., 2018; Fernández-Viejo et al., 2000; López-Fernández et al., 2020)
475 or as the earliest initiation of ocean-continent subduction (Álvarez-Marron et al., 1997;
476 Ayarza et al., 2004; Díaz and Gallart, 2009; Gallastegui et al., 2016). In our opinion,
477 surface topographic features such as marine terraces are not only dependent on the crust
478 thickness as postulated in López-Fernández et al. (2020) but also on the elastic thickness
479 of the whole lithosphere (Burov and Diament, 1995; François et al., 2013). It is
480 noteworthy that the Quaternary kinematics of the active fault analysed in Sierra de la
481 Sobia consist of tangential deformation (Fig. 6), although normal faulting is associated
482 with isostatic balance in passive margins (Conway-Jones et al., 2019; Pederson et al.,
483 2002). The reverse and strike-slip fault kinematics prevail against the current normal
484 faults, mostly locate radially to the outer-arc at the hinge domain of Sierra de la Sobia.

485 Most of the active fault mapped along the Cantabrian wave-cut paleo-platform by
486 Álvarez-Marrón et al. (2008) indicate consistent kinematics with our study area.

487 **5.2 Rock-avalanches: origin and recurrence**

488 Rock fragmentation, weathering, climatic factors, and geomorphological factors, during the
489 withdrawal of glaciers and associated debuttrressing have been described as the triggers of large
490 rock-avalanches (Ambrosi and Crosta, 2011; Ballantyne et al., 2014; Turcotte, 1986).
491 Additionally, in many rock-avalanches, seismicity is the main triggering factor: avalanches
492 triggered by recent (Wasowski et al., 2021) or historical earthquakes (Martin et al., 2014; Zeng et
493 al., 2020) or polyphase rock-avalanches that are consistent with sedimentological paleoseismic
494 records (Grämiger et al., 2016).

495 Slope failure analyses demonstrate that under static conditions the main rupture scarps of
496 the rock-avalanches on the Sierra de la Sobia are mechanically stable (Fig.10) and
497 consequently differential stress must be increased for dynamic fragmentation. Moreover,
498 the BSD analysis shows $r_k > 1$ m for all the rock-avalanche deposits yield D ranging
499 between 2.24 and 2.70 (Table 1), into the usual range of dynamic fragmentation (Storti et
500 al., 2003). Therefore, similar two-stage breakage dynamic processes caused the block
501 fragmentation within all rock-avalanches: (i) dynamic and ballistic fragmentation from
502 the aftershock rupture scarp; and (ii) fragmentation by wear and attrition from the scar
503 slope to the accumulation body, causing the BSD-homogenization within the block size
504 fractions $r_i < 1$ m. The block size at the slope change (r_k) seems to represent a change in
505 the dominant fragmentation mechanism from (i) to (ii). D variations can be interpreted
506 because of the percentage weight of fine to coarse fragments in each respective fraction.
507 So, decreasing particle fragmentation occurred in confined accumulation bodies only
508 because the surface of the accumulation body is considered for the BSD analysis (see
509 methods), where the percentage weight of fine fragments is higher than at the bottom.

510 Consequently, D for $\text{Logr}_k > 1$ is higher in the accumulation body of Cueva Güerta
511 compared to other avalanches (Fig. 12, Table 1). Selection can also be evaluated
512 indirectly by the difference of the roundness versus eccentricity between the fine and
513 coarse fractions of each BSD (Fig. 12B). More selection is expected at the top of the
514 accumulation body than at the tip. For instance, the BSD of Carrea avalanche shows the
515 greatest segregation because only the top sector of the accumulation body is considered,
516 whereas in other avalanches the whole accumulation body is well exposed and
517 consequently used for BSD analysis. This feature is also consistent with the relative ages
518 inferred from BSD. The accumulation body of the largest avalanches is composed of
519 several superposed deposits of horizontal conic shape, where the most recent deposit is
520 located at the top of the accumulation body. The detailed BSD of the Entrago avalanche
521 shows a progressive attenuation of the logr_k -slope rupture as the relative age of the BSD
522 deposit increases (Fig. 11). If the BSD of the analysed avalanches is compared, according
523 to this criterion, Entrago is the oldest rock-avalanche in the Sierra de la Sobia and Cueva
524 Güerta the youngest (Fig. 12A). This relative chronology is consistent with the U/Th ages
525 obtained from the coated calcite blocks sampled in these accumulation bodies (Tables 2
526 and 3).

527 At least three superposed deposits of blocks have been differentiated at the map-scale on
528 the massive avalanches of Sierra de la Sobia (Figs. 7 and 13), along a fault segment ~4.5
529 km length, suggesting that such avalanches record the same seismic events. Moreover,
530 co-seismic rock-falls have been recorded near Villa de Sub (Fig. 14). However,
531 destructive to very destructive events, ranging between VIII to X in the environmental
532 seismic intensity scale (Michetti et al., 2007) could be inferred accordingly, with: (i) the
533 offset and length of the active faults; (ii) the evaluated tectonic uplift and subsidence
534 (Figs. 3, 4, 6); (iii) the length and width of the ground cracks and the reach of slope

535 movements (Figs. 7, 13, 14, Table 1); and (iv) the affected area and type of record
536 (Reicherter et al., 2009). Recently, the empirical power-law relationships between the
537 total volume of the avalanche and the seismic magnitude (Keefe, 1999) were validated
538 (Croissant et al., 2017). However, this approach is challenging to apply in this study area
539 because it is impossible to evaluate which avalanche volume corresponds to each
540 paleoseismic event. Also, for short-term recurrence, the total volume could decrease as
541 the rupture scarp becomes more stable during aftershocks. Currently, the slope stability
542 analyses indicate that a horizontal PGA ranging between 0.10-0.15 g is required to disrupt
543 such scarps again. Sierra de la Sobia experiences moderate seismicity, characterized by
544 frequent $M_s < 6$ events, because of its geodynamic setting (Álvarez-Marrón et al., 1997;
545 Ayarza et al., 2004; Díaz and Gallart, 2009; Gallastegui et al., 2016). In this context, the
546 largest earthquakes generated in the past might occur within recurrence intervals much
547 longer than the period covered by both the historical and instrumental local records (Fig.
548 1B) and could be conditioned by the reactivation of the long-lived crustal León Fault at a
549 slow slip rate during the re-tightening of the CA under NNW-SSE compression. Further
550 work is necessary for insight into the standard $\log r_k = 1$ for all the BSDs analysed (Fig.
551 12A). Samples have been collected from the non-cemented rock-avalanches at Entrago
552 and Carrea to broaden the chronological framework presented here by ^{36}Cl cosmic-ray
553 exposure dating. The accurate date of the latest avalanche-events might help forecast
554 future massive earthquakes in the region.

555 Based on the oldest calcite cement, a reference age of 278.3 ± 32.9 ka is inferred for the
556 oldest cementation episode affecting the Entrago deposit, and hence a minimum age for
557 the oldest rock-avalanche event. Subsequent avalanche cementation occurred thereafter,
558 spanning the last 200 ka, potentially conditioned by Quaternary climate changes. Calcite
559 growth took place preferentially during the interglacials, and during the warm periods

560 that bounded the MIS-3 glacial advance of the Cantabrian Mountains (Rodríguez-
561 Rodríguez et al., 2015).

562 **5.3 Quaternary geomorphological evolution of the landscape**

563 The western hillslope of the Sierra de la Sobia is a structural form controlled by the
564 arcuate orientation of the limestone bedding and MSF. Compression of this mountain
565 range according to the current regional NNW SH_{max} (de Vicente et al., 2008; Custódio et
566 al., 2015) triggered several rock-avalanches with recurrent avenues along the Quaternary
567 period. This active tectonic process strongly conditioned the geomorphology of the
568 Teverga Valley.

569 In this period, the incision rate of the Páramo River may have accelerated as suggested
570 by the cusate shape of the river valley throughout the Foz de la Estrechura canyon (Fig.
571 14). The current course is incised ca 30 m from the paleo-epiphreatic sediment deposited
572 on the upper entrance of Cueva Güerta. The current phreatic level runout ca 100 m below
573 the paleo-phreatic level is defined along the low gradient of the longest gallery in this
574 cave (Ferrerías et al., 2015). However, the accumulation of the rock avalanche confined
575 at the spring of the canyon did not dam the stream. This is because, at that time, the flow
576 of water was underground, and its runout was at a deeper level.

577 Downstream is the old village of Fresneu, which was destroyed on June the 25th 1522.
578 Canon Tirso de Avilés of Oviedo Cathedral tells of an earthquake event, after which a
579 new village was built at the current site (Fig. 14). Moreover, the Entrago avalanche
580 dammed the Val de Cazana, Taja and Páramo Rivers (Fig. 3), deviated the resultant course
581 of the Teverga River at the entrance of the Val de Cerezales canyon, and developed the
582 only floodplains present in this valley (Fig. 7).

583 A detailed analysis of this river sub-basin extended to the whole Nalón basin that would
584 give new insights into understanding the Quaternary geomorphology and tectonics of the
585 Cantabrian Mountains is currently underway.

586 **6. Conclusions**

587 The Quaternary reactivation of minor faults lying along the MSF-trace has
588 accommodated ~300 m uplift of the summits in Sierra de la Sobia. Their slip inversion is
589 consistent with a current N-S trend of the SH_{max} that contributes to the re-tightening of
590 this arcuated mountain range and the stretch of its outer arc also ~300 m by longitudinal
591 tangential deformation.

592 The largest rock-avalanches are distributed along the hinge domain of Sierra de la Sobia,
593 while the smallest are in the southern domain. The sizes of rock-accumulation bodies are
594 proportional to the corresponding vertical drop. BSDs of the accumulation bodies are not
595 fractal. The largest block size fractions ($r_i > 1$ m) have slope D-values ranging between
596 2.70 and 2.24, whereas the block size fractions $r_i < 1$ m have lower D-values.

597 The mechanical slope stability analysis of relevant rupture scarps reported safety factors
598 > 1.3 under static boundary conditions. However, all rupture scarps become unstable if
599 horizontal seismic acceleration rises 0.10-0.15 g.

600 Chronological U/Th data obtained from calcium carbonate cements bounding limestone
601 blocks in the Entrago, Carrea and Cueva Güerta rock-avalanches suggest recurrent
602 instability events for at least the last 300 ka, with episodic cementation occurring during
603 the last five interglacials.

604 Geomorphological and structural data gathered on the western flank of Sierra de la Sobia
605 reveal unambiguously a clear relationship between current tectonics and recurrent
606 catastrophic rock-avalanches.

607 **Acknowledgments**

608 Research funded by the Spanish Ministry of Education and Science, through project
609 CGL2015-66997-R from the National Research plan, and by the FC-GRUPIN-
610 IDI72018/000216 project of the Principado de Asturias government. We thank Lawrence
611 Edwards and Hai Cheng for allowing the use of their facilities to perform the U/Th dating,
612 completed at the University of Minnesota. We would also like to thank for the review of
613 paleo-stress by Gerardo de Vicente, the structural discussion and field reviews with Juan
614 Luis Alonso, and the review of the English text by Andy Whitehead. Finally, we also
615 thank the Editor and the two anonymous reviewers for their valuable comments and
616 remarks.

617

618 **References**

- 619 Alonso, J.L., Marcos, A., Suárez, A., 2009. Paleogeographic inversion resulting from large out
620 of sequence breaching thrusts: The León Faults (Cantabrian Zone, NW Iberia). A new
621 picture of the external Variscan Thrust Belt in the Ibero-Armorican Arc. *Geol. Acta* 7,
622 451–473. <https://doi.org/10.1344/105.000001449>
- 623 Alonso, J.L., Martínez-Abad, I., García-Ramos, J.C., 2007. Nota sobre la presencia de una
624 sucesión cretácica en el Macizo de Las Ubiñas (Cordillera Cantábrica). *Implicaciones*
625 *tectónicas y geomorfológicas. Geogaceta* 47–50.
- 626 Álvarez-Marrón, J., Hetzel, R., Niedermann, S., Menéndez, R., Marquínez, J., 2008. Origin,
627 structure and exposure history of a wave-cut platform more than 1 Ma in age at the coast
628 of northern Spain: A multiple cosmogenic nuclide approach. *Geomorphology* 93, 316–
629 334. <https://doi.org/10.1016/j.geomorph.2007.03.005>
- 630 Álvarez-Marron, J., Rubio, E., Torne, M., 1997. Subduction-related structures in the North
631 Iberian Margin. *J. Geophys. Res. Solid Earth* 102, 22497–22511.
632 <https://doi.org/10.1029/97jb01425>
- 633 Ambrosi, C., Crosta, G.B., 2011. Valley shape influence on deformation mechanisms of rock
634 slopes. *Geol. Soc. London, Spec. Publ.* 351, 215 LP – 233.
635 <https://doi.org/10.1144/SP351.12>
- 636 Ayarza, P., Catalán, J.R.M., Alvarez-Marrón, J., Zeyen, H., Juhlin, C., 2004. Geophysical
637 constraints on the deep structure of a limited ocean-continent subduction zone at the North
638 Iberian Margin. *Tectonics* 23, TC1010. <https://doi.org/10.1029/2002TC001487>
- 639 Ballantyne, C.K., Sandeman, G.F., Stone, J.O., Wilson, P., 2014. Rock-slope failure following
640 Late Pleistocene deglaciation on tectonically stable mountainous terrain. *Quat. Sci. Rev.*
641 86, 144–157. <https://doi.org/10.1016/j.quascirev.2013.12.021>
- 642 Bastida, F., Castro, S., 1988. Estructura del sector septentrional de la Escama de Tameza (Zona
643 Cantábrica, NW de España). *Trab. Geol.* 17, 67–85.
- 644 Bischoff, J.L., Julia, R., Mora, R., 1988. Uranium-series dating of the Mousterian occupation at
645 Abric Romani, Spain. *Nature* 332, 68–70. <https://doi.org/10.1038/332068a0>
- 646 Bulnes, M., Aller, J., 2002. Three-dimensional geometry of large-scale fault-propagation folds
647 in the Cantabrian Zone, NW Iberian Peninsula. *J. Struct. Geol.* 24, 827–846.
648 [https://doi.org/10.1016/S0191-8141\(01\)00114-6](https://doi.org/10.1016/S0191-8141(01)00114-6)
- 649 Bulnes, M.T., 1994. La estructura geológica del Valle del Rio Trubia (Zona Cantábrica, NO de
650 España). Unpubl. PhD Thesis. Universidad de Oviedo.
- 651 Burov, E.B., Diament, M., 1995. The effective elastic thickness (T_e) of continental lithosphere:
652 What does it really mean? *J. Geophys. Res. Solid Earth* 100, 3905–3927.
653 <https://doi.org/10.1029/94JB02770>
- 654 Cadenas, P., Manatschal, G., Fernández-Viejo, G., Welford, J.K., 2018. Margin segmentation
655 during polyphase rifting in the southern Bay of Biscay. *Atl. Geol.* 54, 409–470.
656 <https://doi.org/10.4138/atlgeol.2018.014>
- 657 Conway-Jones, B.W., Roberts, G.G., Fichtner, A., Hoggard, M., 2019. Neogene Epeirogeny of
658 Iberia. *Geochemistry, Geophys. Geosystems* 20, 1138–1163.
659 <https://doi.org/10.1029/2018GC007899>
- 660 Croissant, T., Lague, D., Steer, P., Davy, P., 2017. Rapid post-seismic landslide evacuation
661 boosted by dynamic river width. *Nat. Geosci.* 10, 680–684.

- 662 <https://doi.org/10.1038/ngeo3005>
- 663 Custódio, S., Dias, N.A., Carrilho, F., Góngora, E., Rio, I., Marreiros, C., Morais, I., Alves, P.,
664 Matias, L., 2015. Earthquakes in western Iberia: Improving the understanding of
665 lithospheric deformation in a slowly deforming region. *Geophys. J. Int.* 203, 127–145.
666 <https://doi.org/10.1093/gji/ggv285>
- 667 de Vicente, G., Cloetingh, S., Muñoz-Martín, A., Olaiz, A., Stich, D., Vegas, R., Galindo-
668 Zaldívar, J., Fernández-Lozano, J., 2008. Inversion of moment tensor focal mechanisms
669 for active stresses around the microcontinent Iberia: Tectonic implications. *Tectonics* 27,
670 1–22. <https://doi.org/10.1029/2006TC002093>
- 671 de Vicente Muñoz, G., González-Nistal, S., Muñoz-Martín, A., Vegas, R., Olaiz, A., Fernández-
672 Lozano, J., de Vicente, R., 2007. El cabalgamiento cenozoico de Boinás (Cordillera
673 Cantábrica, España). *Geogaceta* 42, 7–10.
- 674 Delavaud, E., Cotton, F., Akkar, S., Scherbaum, F., Danciu, L., Beauval, C., Drouet, S.,
675 Douglas, J., Basili, R., Sandikkaya, M.A., Segou, M., Faccioli, E., Theodoulidis, N., 2012.
676 Toward a ground-motion logic tree for probabilistic seismic hazard assessment in Europe.
677 *J. Seismol.* 16, 451–473. <https://doi.org/10.1007/s10950-012-9281-z>
- 678 Díaz, J., Gallart, J., 2009. Crustal structure beneath the Iberian Peninsula and surrounding
679 waters: A new compilation of deep seismic sounding results. *Phys. Earth Planet. Inter.*
680 173, 181–190. <https://doi.org/10.1016/j.pepi.2008.11.008>
- 681 Díaz, J., Gallart, J., Carbonell, R., 2016. Moho topography beneath the Iberian-Western
682 Mediterranean region mapped from controlled-source and natural seismicity surveys.
683 *Tectonophysics* 692, 74–85. <https://doi.org/10.1016/j.tecto.2016.08.023>
- 684 Epstein, B., 1947. The mathematical description of certain breakage mechanisms leading to the
685 logarithmico-normal distribution. *J. Franklin Inst.* 244, 471–477.
686 [https://doi.org/10.1016/0016-0032\(47\)90465-1](https://doi.org/10.1016/0016-0032(47)90465-1)
- 687 Fernández-Viejo, G., Gallart, J., Pulgar, J.A., Córdoba, D., Dañobeitia, J.J., 2000. Seismic
688 signature of Variscan and Alpine tectonics in NW Iberia: crustal structure of the
689 Cantabrian Mountains and Duero basin. *J. Geophys. Res.* 105, 3001–3018.
- 690 Fernández-Viejo, G., López-Fernández, C., Domínguez-Cuesta, M., Cadenas, P., 2014. How
691 much confidence can be conferred on tectonic maps of continental shelves? the
692 Cantabrian-Fault case. *Sci. Rep.* 4, 1–7. <https://doi.org/10.1038/srep03661>
- 693 Fernández, F.J., Alonso, J.L., Pando, L., 2018. Evidence for quaternary tectonic activity in the
694 western cantabrian Zone (Passes of Marabio, Sobia nappe). *Geogaceta* 64, 1–3.
- 695 Fernández, F.J., Menéndez-Duarte, R., Aller, J., Bastida, F., 2005. Application of Geographical
696 Information Systems to shape-fabric analysis, in: Bruhn, D., Burlini, L. (Eds.), *High-Strain*
697 *Zones: Structure and Physical Properties*. Geological Society, London, Special
698 Publications, London, pp. 409–420. <https://doi.org/10.1144/GSL.SP.2005.245.01.20>
- 699 Ferreras, S., Franco, J., Fresnadiello, A., Rojo, D., Turmo, A., Álvarez, A., Álvarez, M.,
700 Ballesteros, D., Cañón, G., 2015. Avance en 2015 al estudio espeleológico de Cueva
701 Güerta. *Frenéu*, Concejo de Terverga. Asturias. Colectivo Asturiano de Espeleólogos.
- 702 Fillon, C., Pedreira, D., Van Der Beek, P.A., Huisman, R.S., Barbero, L., Pulgar, J.A., 2016.
703 Alpine exhumation of the central Cantabrian Mountains, Northwest Spain. *Tectonics* 35,
704 339–356. <https://doi.org/10.1002/2015TC004050>
- 705 François, T., Burov, E., Meyer, B., Agard, P., 2013. Surface topography as key constraint on
706 thermo-rheological structure of stable cratons. *Tectonophysics* 602, 106–123.
707 <https://doi.org/10.1016/j.tecto.2012.10.009>

- 708 Gallastegui, J., Pulgar, J.A., Gallart, J., 2016. Alpine tectonic wedging and crustal delamination
709 in the Cantabrian Mountains (NW Spain). *Solid Earth* 7, 1043–1057.
710 <https://doi.org/10.5194/se-7-1043-2016>
- 711 Giardini, D., Wössner, J., Danciu, L., 2014. Mapping Europe's Seismic Hazard. EOS,
712 *Transactions. Am. Geophys. Union* 95, 261–268. <https://doi.org/10.1002/2014EO290001>
- 713 Goodman, R.E., 1989. *Introduction to rock mechanics*. John Wiley & Sons, Toronto.
- 714 Grämiger, L.M., Moore, J.R., Vockenhuber, C., Aaron, J., Hajdas, I., Ivy-Ochs, S., 2016. Two
715 early Holocene rock avalanches in the Bernese Alps (Rinderhorn, Switzerland).
716 *Geomorphology* 268, 207–221. <https://doi.org/10.1016/j.geomorph.2016.06.008>
- 717 Hallstadius, L., 1984. A method for the electrodeposition of actinides. *Nucl. Instruments*
718 *Methods Phys. Res.* 223, 266–267. [https://doi.org/10.1016/0167-5087\(84\)90659-8](https://doi.org/10.1016/0167-5087(84)90659-8)
- 719 Heim, A., 1932. *Bergsturz und Menschenleben*, Fretz und Wasmuth. Zürich, 218 pp.
- 720 Hudson, J.A., Harrison, J.P., 1997. *Engineering rock mechanics: an introduction to the*
721 *principles*. Elsevier, Oxford.
- 722 Keefer, D.K., 1999. Earthquake-induced landslides and their effects on alluvial fans. *J.*
723 *Sediment. Res.* 69, 84–104. <https://doi.org/10.2110/jsr.69.84>
- 724 Keulen, N., Heilbronner, R., Stünitz, H., Boullier, A.M., Ito, H., 2007. Grain size distributions
725 of fault rocks: A comparison between experimentally and naturally deformed granitoids. *J.*
726 *Struct. Geol.* 29, 1282–1300. <https://doi.org/10.1016/j.jsg.2007.04.003>
- 727 Lefort, J.-P., 1989. *Basement correlation across the North Atlantic*. Springer-Verlag Berlin
728 Heidelberg. <https://doi.org/10.1007/978-3-642-73350-5>
- 729 López-Fernández, C., Llana-Fúnez, S., Fernández-Viejo, G., Domínguez-Cuesta, M.J., Díaz-
730 Díaz, L.M., 2020. Comprehensive characterization of elevated coastal platforms in the
731 north Iberian margin: A new template to quantify uplift rates and tectonic patterns.
732 *Geomorphology* 364. <https://doi.org/10.1016/j.geomorph.2020.107242>
- 733 López- Fernández, C., Fernández- Viejo, G., Olona, J., Llana- Fúnez, S., 2018. Intraplate
734 Seismicity in Northwest Iberia along the Trace of the Ventaniella Fault: A Case for Fault
735 Intersection at Depth. *Bull. Seismol. Soc. Am.* 108, 604–618.
736 <https://doi.org/10.1785/0120170215>
- 737 Lotze, F., 1945. Zur Gliederung der Varisziden der Iberischen Meseta. *Geotektonische*
738 *Forschungen* 6, 78–92.
- 739 Marcos, A., Pulgar, J.A., 1982. An approach to the tectonostratigraphic evolution of the
740 Cantabrian foreland thrust and fold belt, Hercynian Cordillera of NW Spain. *Neues Jahrb.*
741 *für Geol. und Paläontologie Abhandlungen* 163, 256–260.
- 742 Martin, S., Campedel, P., Ivy-Ochs, S., Viganò, A., Alfimov, V., Vockenhuber, C., Andreotti,
743 E., Carugati, G., Pasqual, D., Rigo, M., 2014. Lavini di Marco (Trentino, Italy): 36Cl
744 exposure dating of a polyphase rock avalanche. *Quat. Geochronol.* 19, 106–116.
745 <https://doi.org/10.1016/j.quageo.2013.08.003>
- 746 Menéndez-Duarte, R., Marquínez, J., Fernández-Menéndez, S., Santos, R., 2007. Incised
747 channels and gully erosion in Northern Iberian Peninsula: Controls and geomorphic
748 setting. *Catena* 71, 267–278. <https://doi.org/10.1016/j.catena.2007.01.002>
- 749 Merino-Tomé, O., Suárez, Á., Alonso, J.L., González-Menéndez, L., Heredia, N., Marcos-
750 Vallauré, A., 2011. Mapa Geológico Digital continuo E. 1:50000, Principado de Asturias
751 (Zonas: 1100-1000-1600) , in: Navas, J. (Ed.), GEODE. Mapa Geológico Digital Continuo
752 de España. Sistema de Información Continua: SIGECO. IGME, Madrid.

- 753 Michetti, A.M., Esposito, E., Guerrieri, L., Porfido, S., Serva, L., Tatevossian, R., Vittori, E.,
754 Audemard, F., Azuma, T., Clague, J., Comerci, V., Gurpinar, A., McCalpin, J.,
755 Mohammadioun, B., Morner, N.A., Ota, Y., R., 2007. Intensity Scale ESI 2007. Mem.
756 Descr. della Cart. Geol. d'Italia, Spec. Vol. 74 7–54.
- 757 Pederson, J.L., Mackley, R.D., Eddleman, J.L., 2002. Colorado Plateau uplift and erosion
758 evaluated using GIS. *GSA Today* 12, 4–10. [https://doi.org/10.1130/1052-
759 5173\(2002\)012<0004:CPUAEE>2.0.CO;2](https://doi.org/10.1130/1052-5173(2002)012<0004:CPUAEE>2.0.CO;2)
- 760 Pulgar, J.A., Alonso, J.L., Espina, R.G., Marín, J.A., 1999. La deformación alpina en el
761 basamento varisco de la Zona Cantábrica. *Trab. Geol.* 21, 283–294.
- 762 Ramsay, J.G., 1967. *Folding and fracturing of rocks*. McGraw-Hill, New York.
- 763 Reicherter, K., Michetti, A.M., Barroso, P.G.S., 2009. Palaeoseismology: Historical and
764 prehistorical records of earthquake ground effects for seismic hazard assessment. *Geol.*
765 *Soc. Spec. Publ.* 316, 1–10. <https://doi.org/10.1144/SP316.1>
- 766 Rodríguez-Pérez, C., 2012. La evolución antigua del relieve en el área central de la Cordillera
767 Cantábrica. *Eria* 89, 203–230.
- 768 Rodríguez-Rodríguez, L., Jiménez-Sánchez, M., Domínguez-Cuesta, M.J., Aranburu, A., 2015.
769 Research history on glacial geomorphology and geochronology of the Cantabrian
770 Mountains, north Iberia (43-42°N/7-2°W). *Quat. Int.* 364.
771 <https://doi.org/10.1016/j.quaint.2014.06.007>
- 772 Rosenbauer, R.J., 1991. UDATE1: A computer program for the calculation of uranium-series
773 isotopic ages. *Comput. Geosci.* 17, 45–75. [https://doi.org/https://doi.org/10.1016/0098-
774 3004\(91\)90079-S](https://doi.org/https://doi.org/10.1016/0098-3004(91)90079-S)
- 775 Shen, C.C., Lawrence Edwards, R., Cheng, H., Dorale, J.A., Thomas, R.B., Bradley Moran, S.,
776 Weinstein, S.E., Edmonds, H.N., 2002. Uranium and thorium isotopic and concentration
777 measurements by magnetic sector inductively coupled plasma mass spectrometry. *Chem.*
778 *Geol.* 185, 165–178. [https://doi.org/10.1016/S0009-2541\(01\)00404-1](https://doi.org/10.1016/S0009-2541(01)00404-1)
- 779 Stich, D., Martínez-solares, J.M., Custódio, S., Batlló, J., Martín, R., Teves-costa, P., Morales,
780 J., 2020. Seismicity of the Iberian Peninsula, in: Quesada, C., Oliveira, J. (Eds.), *The*
781 *Geology of Iberia: A Geodynamic Approach*. Springer International Publishing, pp. 11–
782 32. <https://doi.org/10.1007/978-3-030-10931-8>
- 783 Storti, F., Billi, A., Salvini, F., 2003. Particle size distributions in natural carbonate fault rocks:
784 Insights for non-self-similar cataclasis. *Earth Planet. Sci. Lett.* 206, 173–186.
785 [https://doi.org/10.1016/S0012-821X\(02\)01077-4](https://doi.org/10.1016/S0012-821X(02)01077-4)
- 786 Talvitie, N., 1972. Electrodeposition of actinides for alpha spectrometric determination. *Anal.*
787 *Chem.* 44, 280–283.
- 788 Turcotte, D.L., 1986. Fractals and fragmentation. *J. Geophys. Res. Solid Earth* 91, 1921–1926.
789 <https://doi.org/10.1029/JB091iB02p01921>
- 790 Wasowski, J., McSaveney, M.J., Pisano, L., Del Gaudio, V., Li, Y., Hu, W., 2021. Recurrent
791 rock avalanches progressively dismantle a mountain ridge in Beichuan County, Sichuan,
792 most recently in the 2008 Wenchuan earthquake. *Geomorphology* 374.
793 <https://doi.org/10.1016/j.geomorph.2020.107492>
- 794 Weil, A.B., Voo, R. Van der, van der Pluijm, B.A., 2001. Oroclinal bending and evidence
795 against the Pangea megashear: The Cantabria-Asturias arc (northern Spain). *Geology* 29,
796 991. [https://doi.org/10.1130/0091-7613\(2001\)029<0991:OBAEAT>2.0.CO;2](https://doi.org/10.1130/0091-7613(2001)029<0991:OBAEAT>2.0.CO;2)
- 797 Zeng, Q., Yuan, G., McSaveney, M., Ma, F., Wei, R., Liao, L., Du, H., 2020. Timing and

798 seismic origin of Nixu rock avalanche in southern Tibet and its implications on Nimu
799 active fault. Eng. Geol. 268, 105522. <https://doi.org/10.1016/j.enggeo.2020.105522>
800

801 **Figure and table captions**

802 Fig. 1: (A) Overview map of NW Spain presenting the evidence for the main Alpine exhumation
803 phase in the Cantabrian Mountain and Basque-Cantabrian Basin. (B) Geological map of the
804 Cantabrian Zone. Available seismic records are indicated with stars, and the trace of the
805 geological section (C). Inset shows the location of Fig. 2. The Somiedo (SoT) and Sobia (ST)
806 thrusts.

807 Fig. 2: Aerial image of Sierra de la Sobia and Macizo de Ubiña. Main segments of the northern
808 León Fault sector, rock-avalanches and the highest summits are highlighted (orange lines). The
809 orange arrow shows the NNW trends of the current regional maximum horizontal stress (SHmax;
810 de Vicente et al. 2008).

811 Fig. 3: Geological map of the Sobia Nappe showing the relationships between rock-avalanche,
812 Quaternary sediments, mechanical contacts and relief. Traces of the geological section
813 represented in Fig. 4 are also shown.

814 Fig. 4: Longitudinal-section (A) and three cross-sections (B, C, and D) to Sierra de la Sobia.
815 Traces of the transversal cross-sections and the range level of summits (RLS) line are located on
816 the longitudinal-section A.

817 Fig. 5: Panoramic view of a 15km-long segment of Sierra de la Sobia, including the hinge and
818 southern domains. Carboniferous limestone outcrop exposes MS, thrusting out of sequence the
819 earliest Variscan syncline and thrust. Minor normal and strike-slip faults cut the MS-trace, also
820 folded by the Foz de la Estrechura anticline, southward. RLS have small steps controlled by the
821 vertical slip of both later-normal and strike-slip faults as the mountain chain increases in height
822 southward (see also Fig. 4A).

823 Fig. 6: Structural map of Sierra de la Sobia showing the relationship between the León Fault, the
824 latest faults and the fracture network imposed on the limestone massif. The stereonet plots
825 represent the equal area and lower hemisphere projections of fault planes and slickenlines. Arrows
826 represent the direction of displacement inferred from slickenlines. Blue lines and symbols

827 represent fault segments reactivated during the Quaternary and their respective kinematics.
828 Orange finite strain ellipse is scaled to $R=1.42$, strain ellipse orientation is consistent with the
829 kinematic of most current active faults.

830 Fig. 7: Detailed geomorphological map of the Gradura and Entrago rock-avalanches including
831 earth flow, slope dynamic and river deposits. Stars show the location of U/Th samples.

832 Fig. 8: Entrago rock-avalanche. (A) Details of the rupture scarp where a rotational rockslide (rock
833 slump) rests atop. The Sobia spire is a buttress 125 m in height separated by less than 50 m from
834 the rupture scarp. A huge rock-topple was triggered at the southern scarp tip. Note that
835 discontinuities have the same pattern into the rupture scarp than in the rock-slump. (B) Behind
836 the Sobia spire a transverse fault N5°E-strike with slickenlines indicating sub-horizontal right-
837 lateral displacement (North is on the left-hand side) is exposed.

838 Figure 9: Dynamic analysis of slope instability risk considering four failure modes for the rupture
839 scarp of Entrago. Flexural toppling analysis following Goodman (1989) and direct toppling
840 following Hudson and Harrison (1997). Pole planes are plotted in lower hemispheres and equal
841 angle stereonets. Contour density at constant intervals of 0.7%.

842 Fig. 10: Shape-fabric analysis of the depletion zone for the Entrago rock-avalanche (612 wedges).
843 (A) Diagram showing the size frequency (black line) and the area percentage (dashed line) versus
844 wedge size. (B) Histogram showing the frequency of the orientation of the major ellipse inscribed
845 in each wedge. Fine fraction (white bars) of wedges was sketched from the thickly fractured rock-
846 slump of the unstable residual relief (Fig. 7A) and it preserves the same orientation than the coarse
847 fraction (black bars). (C) Shape parameter (S ; Fernández et al., 2005) versus eccentricity diagram.
848 Triangular wedges, defined by the intersection of joint sets, dominate within the fine fraction
849 (white dot), and rhomboidal wedges dominate within the coarse fraction (black dot). Error bars
850 represent standard deviations.

851 Fig. 11: Block size analysis of the Entrago rock-avalanche. (A) Histogram of equivalent radii
852 (dm) for the whole accumulation body (4805 blocks). (B) Log-log plot of frequency versus

853 equivalent radius (20 bins per order of magnitude). The slope of the fitting lines yields two D -
854 values which intersect at r_k . (C) Histogram of equivalent radii (dm) for the three superimposed
855 bodies mapped (Fig. 7). (D) Log-log plot of frequency versus equivalent radius for the earliest,
856 (E) middle and (D) the apical bodies.

857 Fig. 12: Shape-fabric analysis of blocks for the four accumulation bodies studied in detail. (A)
858 Log-log plot of frequency versus equivalent radius (20 bins per order of magnitude). The slope
859 of the fitting lines yields two D -values which intersect at r_k . (B) Shape parameter (S ; Fernández
860 et al., 2005) versus eccentricity diagram. Error bars are their respective standard deviations. Block
861 sizes plotted for each fine fraction is larger than $\text{Log}(r_i)=0.5$ (dm).

862 Fig. 13: Detailed geomorphological map of the Sobrevilla and Carrea rock-avalanches (left and
863 right, respectively). Start indicates the location of U/Th samples.

864 Fig. 14: Detailed geomorphological map of rock-avalanches occurred at Fresneu, Cueva Güerta,
865 Villa de Sub, Sabariegos and Busbigre. Stars indicate the location of U/Th samples of calcite
866 cements coating the blocks of the Cueva Güerta rock-avalanche deposit. Cave plan view modified
867 after Ferreras et al. (2015).

868 Fig. 15: South-Eastern Sierra de la Sobia. Villa de Sub is located down hillslope at the tip of the
869 accumulation body. (A) Geology sketched onto the picture highlights the effect of the current
870 right-lateral faults (F_{p1}) and fold-related onto the back-thrust structure of the basement. One of
871 such fault is the rupture plane of the Villa de Sub rock-avalanche. (B) The picture shows the
872 regular and penetrative joint set J_{p1} associated with faults F_{p1} . Limestone bedding surfaces (S_0)
873 dip in the opposite direction to the SE hillslope, enhancing the risk for direct toppling. Width of
874 view is ~ 500 m in A, and ~ 50 m in B.

875 Table 1: Geometrical features of rock-avalanches located at the northern domain (Marabio); the
876 hinge domain (Gradura, Entrago and Sobrevilla); and the southern domain of Sierra de la Sobia
877 (Carrea, Cueva Güerta, Villa de Sub, Sabariegos and Busbigre). Sites are in Figs. 3 and 5. H is
878 the vertical drop and L is the length of fall. H/L ratio is the Fahrböschung parameter of Heim

879 (1932) and ϕ is the corresponding angle. Dimension fractal (D) for the block size distribution
880 (BSD) within the accumulation bodies are obtained from the slope line fit yield values $> r_k$ (Fig.
881 12 A).

882 Table 2 U/Th isotopic compositions and ^{230}Th ages for samples analysed by α -spectrometry.
883 Analytical errors are 2σ of the mean. Samples, UTM coordinates ETRS-89, 29T.

884 Table 3: U/Th isotopic compositions and ^{230}Th ages for samples analysed by Alpha spectrometry.
885 Analytical errors are 2σ . UTM coordinates ETRS-89, 29T.

1 **Gravitational slope processes triggered by past earthquakes on the Western**
2 **Cantabrian Mountains (Sierra de la Sobia, Northern Spain)**

3 Francisco José Fernández ^{*a}, Rosana Menéndez-Duarte ^a, Luis Pando ^a, Laura
4 Rodríguez-Rodríguez ^b, Miguel Iglesias ^a

5 ^a Departamento de Geología, Universidad de Oviedo, c/ Jesús Arias de Velasco s/n,
6 33005 Oviedo, Asturias, Spain.

7 ^b Departamento de Ciencias de la Tierra y Física de la Materia Condensada, Universidad
8 de Cantabria, Av. Los Castros s/n, 39005 Santander, Spain.

9 ^{*}Corresponding author. E-mail address: fjfernandez@uniovi.es

10 **Abstract**

11 Sierra de la Sobia is a linear mountain range of arcuate shape, located West of the
12 Cantabrian Mountains. The long-lived crustal León Fault runs along its western hillslope,
13 and its trace is partially covered by multiple rock-avalanches. Here we discuss if recurrent
14 paleo-earthquakes in the M₆+ range could have acted as the triggering factor for rock-
15 avalanches in a region where the historical and instrumental seismic records only include
16 seismic events up to M_s 4.6. Evidence concurring with a coseismic origin includes: (i)
17 kinematic of current minor transverse and parallel faults to Sierra de la Sobia being
18 consistent with a horizontal North-South compression of the Cantabrian Arc; (ii) slopes
19 of the depletion zones that would become unstable if horizontal seismic ground rose 0.10–
20 0.15 g; and (iii) block size-reduction by dynamic fragmentation creating block size
21 distribution with fractal dimension, ranging between 2.24 and 2.70. U/Th dating of seven
22 calcite precipitates coating the blocks of cemented rock-avalanche deposits suggesting

23 that cementation has taken place in multiple episodes since MIS-9a. Neotectonics of
24 Sierra de la Sobia are expressed in subtle changes in relief after extremely rapid co-
25 seismic events, with average recurrence intervals much longer than the time covered by
26 the regional historical and instrumental period.

27 *Keywords:* Rock-avalanche; U/Th dating; Quaternary tectonics; Cantabrian Mountains;
28 Northern Iberia plate, paleo-seismicity.

29 **1. Introduction**

30 The Cantabrian Arc (CA), also known as Ibero-Armorican Arc (Lefort, 1989), is the
31 largest structure of the Variscan orogeny in Western Europe. The CA deformed an
32 initially linear foreland thrust and fold belt, formally defined as the Cantabrian Zone (CZ;
33 Lotze, 1945) in the latest Stephanian to the earliest Permian (Weil et al., 2001). Later, the
34 CA also controlled the reactivation of the basement during the Alpine cycle, when the
35 Cantabrian Mountains were raised (Gallastegui et al., 2016). Alpine deformation
36 produced the inversion of the northern Iberian plate, and it migrated and decreased
37 progressively from the Pyrenees, westward to the CA (Fig. 1A). Alpine sedimentation
38 ceased after the Late Oligocene (Álvarez-Marron et al., 1997), and Alpine exhumation of
39 the central part of the Cantabrian Mountains occurred from 39 to 29 Ma, at a rate of 2.4–
40 3 mm yr⁻¹ (Fillon et al., 2016). Little is known about the post-Oligocene tectonics of the
41 Cantabrian Mountains due to the scarcity of Tertiary outcrops, the limited size of surficial
42 formations formed since the late Quaternary glaciations, and the later slope dynamics
43 controlled by fluvial incision (Menéndez-Duarte et al., 2007; Rodríguez-Rodríguez et al.,
44 2015). Consequently, we might wonder if evidence of Quaternary deformation exists in
45 the Cantabrian Mountains, and what traces correspond to active landscape processes.

46 Nowadays, northern Iberia is considered a passive margin, hundreds of kilometres away
47 from the interaction of the Nubia Plate with the Iberian microplate. This overall tectonic
48 setting engenders a stress field in the Iberian Peninsula, characterized by a predominately
49 NNW to NW trending maximum horizontal stress (SHmax; de Vicente et al., 2008;
50 Custódio et al., 2015). In this context, the Cantabrian Mountains are considered a
51 seismically active shallow crust (Delavaud et al., 2012) with earthquakes of low to
52 moderate magnitude (Stich et al., 2020). During the 2015–2017 instrumental period, the
53 CZ recorded 40 seismic events of surface wave magnitude (M_s)>2 at depths of between
54 9 and 18 km at the intersection between the León and Ventaniella faults and the biggest
55 recorded was an M_s 3.7 event (Fig. 1B; López- Fernández et al., 2018). The León Fault
56 is a breaching fault (Alonso et al., 2009) buckled by the CA, and cut northwards by the
57 younger Permo-Triassic right-lateral Ventaniella Fault. Large submarine avalanche
58 deposits have recently been found, along with the northwest offshore extension of the
59 Ventaniella Fault-scarp (Fernández-Viejo et al., 2014), near to the location of the
60 historical earthquakes of 1522 and 1861 (Fig. 1B). East-west trending uplifted wave-cut
61 platforms extend along the Cantabrian coastline for more than 400 km, tectonically
62 uplifted since at least 1–2 Ma (Álvarez-Marrón et al., 2008).

63 These tectonic geomorphology imprints might result from the ongoing slow convergence
64 and inversion extending along the Cantabrian coast, where the CA may reactivate. To test
65 this hypothesis, we studied the recent tectonic geomorphology of Sierra de la Sobia, a
66 Carboniferous limestone mountain range of arcuate shape, buckled according to the
67 curvature of the CA to the west of the Ventaniella Fault. The northern branch of the León
68 Fault lies along the western flank of Sierra de la Sobia (Figs. 1B and 1C), and an unusually
69 high number of rock-avalanches never previously described or analysed overlie the fault
70 trace. In 1996 an earthquake of M_s 4.1 (Fig. 1B) struck the Villa de Sub village on the

71 southern slope of Sierra de la Sobia, triggering a rock-fall. North-westward, El Canto
72 district was built atop the most massive rock-avalanche, composed of several superposed
73 deposits. The higher parts of this avalanche still represent a severe risk for the citizens of
74 Entrago and La Plaza. Moreover, an early cemented deposit accumulated about 600 m
75 east of Sobrevilla has its origin in a rockfall from the deposit. The number of tension
76 cracks easily visible on Google Earth suggest that more rockfalls are likely to happen. In
77 addition, a reverse fault superposing Carboniferous limestone onto cemented talus scree
78 deposits has also been described (Fernández et al., 2018). At first sight, Sierra de la Sobia
79 is among the best places to shed new light on the Quaternary tectonic geomorphology in
80 the CZ.

81 **2. Regional setting**

82 Sierra de la Sobia is in the eastern nappe of the Somiedo Unit (Figs. 1B, C; Alonso et al.,
83 2009). From a geomorphological standpoint, it is an arcuate mountain range ~16 km long
84 and 2-5 km wide with a Range Level of Summits (RLS) dipping 1.5° northward (Figs. 2,
85 3, 4 and 5). It is formed by a continuously well-exposed outcrop of Carboniferous
86 limestone. The highest elevations of these mountains are south of Sierra de la Sobia, at
87 the Ubiña Massif with peaks 400 m higher than the regional-RLS. It is noteworthy that
88 the León Fault is bent around the Ubiña Peak (2417 m), accordingly with CA orocline
89 and such a footwall corner gives relief to a syntaxial shape (Fig. 2). Carboniferous
90 limestone overrides the Lower Cretaceous cover south of the Ubiña Peak, evidencing the
91 Alpine reactivation of the León Fault (Alonso et al., 2007). The long-lived León Fault has
92 been active in different tectonic cycles, and it remains seismically active (Fig. 1B;
93 López- Fernández et al., 2018).

94 **2.1 Variscan structure**

95 The Paleozoic basement of the Sobia Nappe involves an ~2500 m and a 500 m-thick syn-
96 orogenic sequence (Fig. 3; Marcos and Pulgar, 1982). During the Variscan orogeny the
97 oldest thrusts, such as the Sobia, Tameza, and Somiedo, accommodated most of the
98 shortening in deep levels (Figs. 1C and 3). Upwards, the shortening was accommodated
99 stratigraphically by fault-propagation folds, like the Caranga Antiform (Figs. 3 and 4B;
100 Bulnes and Aller, 2002). It consists of a stack of at least three thrusts of Ordovician
101 quartzite and sandstone formed to facilitate accommodation for shortening northwards
102 due to the presence of lateral thrust ramps (Bastida and Castro, 1988).

103 Later, the León Fault cut the sequence, superposing the Somiedo and the Tameza Nappes
104 onto the Sobia Nappe (Fig. 1C). The primary displacement of the León Thrust occurred
105 before the CA, and kinematic markers indicate an ENE transport direction (Alonso et al.,
106 2009). Since the CA bends the León Fault, it trends along with two main strikes N30°W
107 and N100°E, respectively, from the Ubiña Massif (Fig. 2). Its North-Western termination
108 consists of a splay fault formed by three main segments. The Marabio Segment-Fault
109 (MSF; Figs. 1C, 2, 4) is the longest at 48 km, its trace being partially covered by rock
110 avalanches triggered along the western flank of Sierra de la Sobia.

111 **3. Materials and methods**

112 The geology of Sierra de la Sobia was entirely reviewed based on the latest regional study
113 (Alonso et al., 2009) and the analysis of previous geological maps of the northern and
114 eastern areas (Bastida and Castro, 1988; Bulnes, 1994), and the online version of the
115 continuous digital geological map of the CZ, scale 1:50,000 (Merino-Tomé et al., 2011).
116 This map differentiates the unconformable Quaternary, Tertiary, and Stephanian outcrops
117 from the Paleozoic underlying basement, as well as the Variscan mechanical contact from
118 the latterly developed structures (Fig. 3). Quaternary deposits and fracture networks
119 within the limestone massif have been tracked from fieldwork and ortho-photographs,

120 scale 1:50,000 (PNOA series, IGN). Due to the difficulties inherent to discriminating
121 Quaternary faults from other earlier Cenozoic faults, both have been grouped as “late
122 faults” when cut-off relationships with the earlier Variscan faults can be established.
123 However, most of these later faults do not show relative displacements at our working
124 scale, because fault slips are frequently <10 m.

125 A selection of nine rock-avalanches was quantitatively characterized. The vertical drop
126 (H) measures the difference in height between the crown of the depletion zone and the
127 toe of the accumulation body, and the length (L) is the horizontal distance between both
128 points. The rock-avalanche volume was estimated multiplying its surface area by the
129 mean thickness of the accumulation body. The average thickness of rock-avalanche
130 deposits was indirectly estimated as half of the possible maximum thickness of the
131 deposit, calculated from the topographic expression of the accumulation body.

132 Analyses of Block Size Distribution (BSD) were completed in four representative
133 deposits of rock-avalanches using high-resolution drone imagery to compile maps of
134 block sizes >10 cm. Ortho-photographs were acquired from a drone, ATYGES FV-8,
135 using pre-planned flight lines of the mapped areas and geo-referenced with a GPS,
136 LEYCA GS14 GNSS. The fractal dimension (D , Epstein, 1947) was calculated in such
137 deposits easily, using the BSD of >14k blocks as the slope of the lineal fit in log
138 frequency/log equivalent radius diagrams; they were plotted showing 20 bins per order
139 of magnitude. The shape parameter S calculated as $S = \frac{4\pi A}{P^2}$ (1) (Fernández et al., 2005),
140 where the area A and perimeter P of wedges were measured in pixel^2 and pixel ,
141 respectively. Wedges <20 pixel^2 were removed. S is not wedge-size dependent, and
142 ranges between 1 (wedge-shape is a perfect circle) and 0 as irregularities of the wedge-

143 shape increase. Block size measures by the radii equivalent (r_i) of each block, where $r_i =$

144 $\sqrt{\frac{(A+P)}{\pi}}$ (2).

145 The rock mechanics of the residual slope were analysed where the rupture scarps were
146 mapped. Slope stability was calculated based on over 350 measurements of joint and fault
147 plain orientations using the advanced computational tools for geometrical, kinematical,
148 and mechanical analysis of the Dips 7.0, Rocplane, and Swedge programs, respectively.

149 Mechanical discontinuities were heuristically classified as: (i) bedding planes (S_0); (ii)
150 faults parallel (F_p) or transverse (F_r) to the range trend; and (iii) joints parallel (J_p) or
151 transverse (J_r) to the range trend. Joints transverse to the range were subdivided according
152 to the direction and angle of dip in: (i) $<30^\circ$ dip angle northwards (J_{r1}); (ii) $>50^\circ$ angle
153 northwards ($J_{r1'}$); (iii) $<30^\circ$ dip angle southwards (J_{r2}); (iv) $>50^\circ$ angle southwards ($J_{r2'}$).

154 Calcite cements, interfusing blocks and pebbles in the oldest rock-avalanches were
155 collected at eight sampling localities and treated in the laboratory to extract the calcite for
156 U/Th dating. Five of the eight samples processed exhibited calcitic cement pure enough
157 for radiometric analysis. Calcite crystals were selected under the microscope to minimize
158 detrital contamination from detrital fine sediment matrix. U/Th dating was completed at
159 the University of Minnesota by Inductively Coupled Plasma Mass Spectrometry (ICP-
160 MS) as described by Shen et al. (2002). Sample RB_02 was replicated by sample RB_9
161 and sample RB_03 by sample RB_10 by the U/Th facility at the Institute of Earth
162 Sciences Jaume Almera (ICTJA-CSIC; Barcelona). The replicates provided purer calcite
163 cements which reduced the age uncertainties previously obtained, likely due to a Th
164 excess of detrital origin. The chemical separation and purification of the radioisotopes
165 followed Bischoff et al. (1988). The isotope electrode position followed Talvitie (1972)

166 and was modified following Hallstadius (1984). Age calculations were based on
167 Rosenbauer (1991). Results are compiled in Table 3.

168 **4. Results**

169 Three structural domains have been distinguished in Sierra de la Sobia. The northern
170 domain extends southward to the Marabio Mountain Pass. The MSF outcrops within the
171 Westphalian shale, superposing the Teverga coal basin (Middle and Upper Westphalian
172 formations in Figs. 3 and 4) onto the Sobia Nappe. The Tameza Thrust and MS converge
173 progressively northwards (Fig. 3). The western hillslope of Sierra de la Sobia is separated
174 by >1 km of MS-trace (Fig. 4B), and it lacks rock-avalanches. Minor parallel faults trend
175 NNE, and transverse faults define three sets trending NE, E, and SE. A reverse parallel-
176 fault superposes Carboniferous limestone westward onto recently cemented talus-scrree
177 deposits, with up to 6 m net slip (Fernández et al., 2018). A fault splay also cuts the
178 Caranga fault-propagation anticline (Figs. 3, 4B, and 6). It shows a reverse displacement
179 with anticlockwise rotation from SW to S. The kinematic agrees with the Alpine
180 inversion, but also with the NNW-trend of the current regional SHmax. The stress
181 inversion obtained for Sierra de la Sobia, after excluding some of the latest transverse
182 fault kinematics that gave inconsistent solutions, gives a similar SHmax, and the
183 limestone outcrop has a joint fracture network with similar strikes to faults belonging to
184 this domain (Fig. 6).

185 The hinge domain extends southward from Marabio Pass to Sobrevilla (Fig. 3). The
186 arcuate MSF-trace lies progressively closer to the western hillslope of Sierra de la Sobia.
187 The slope has a convex shape and has recorded several rock-avalanches. The limestone
188 outcrops' width decreases progressively as the curvature of the arcuate range increases
189 (Fig. 3). Deformation has been accommodated by normal faults that transect the hinge of
190 the range, some of them cut MSF. Southward, MSF is covered by the Entrago rock-

191 avalanche. The outcrop of limestone is strongly fractured, and the fracture network is
192 formed by joint sets parallel to the main fault strikes (Fig. 6).

193 The southern domain extends from the Entrago to the Villa de Sub rock-avalanches (Fig.
194 3). The South-Western hillslope of the range between the Entrago and the Carrea rock-
195 avalanches is a structural form controlled by the orientation of the limestone bedding and
196 MSF. Both mechanical discontinuities run parallel to the slope, and dip in the same
197 direction but are more pronounced than the slope. Parallel faults run SE, with transverse
198 faults and fractures defining three sets trending N, NE, and E, respectively (Fig. 6). The
199 periclinal structure of the Sobia Nappe is exposed on the southern hillslope of Sierra de
200 la Sobia (Fig. 3). The structure consists of folds related to Variscan thrusts in the lateral
201 ramp of the Sobia Nappe and with a transport direction north-eastward. The León Fault
202 thrusts out of sequence towards the NE and accumulates a total displacement of ~9 km in
203 the section shown in Fig. 1C (Alonso et al., 2009). This lateral ramp was shifted 45°NW
204 during the Alpine inversion.

205 More recently, the current re-tightening of the Sobia Nappe was accommodated by right-
206 lateral faults (N150°E-strike). The trace of these faults runs parallel to the Taja Fault
207 segment throughout the southern hillslope of Sierra de la Sobia. Additionally, several
208 active faults trending E-W have exposed their respective fault scarps and have been
209 mapped on the junction of the splay between the Trobaniello Fault segment and the MSF.
210 Most of them are small (widths <7 km) with relative movement frequently attenuated
211 laterally and accommodated by the thickly fractured surficial network of the limestone
212 massif (Fig. 6).

213 Restoration of an eventual continuous RLS-line before its segmentation along the
214 northern and hinge domains of the range results in an extension of ~300 m southward by
215 right-lateral faults N150°E-strike, and potentially by faults trending E-W (Fig. 6). The

216 current re-tightening of the arc described by the hinge domain of Sierra de la Sobia has
217 been measured, assuming that the extension of the western convex hillslope was created
218 by tangential longitudinal folding (Ramsay, 1967). The finite neutral surface is on
219 longitudinal section A (Fig. 3) and runs along the RLS (Fig 4). The result is an
220 incremental longitudinal strain $e_l = 0.031$ that produces a strain ellipse on the outer arc of
221 aspect ratio $R = 1.42$ (Fig. 6), therefore an angular extension of 3.32° along the western
222 convex hillslope. However, the kinematics of the current faults suggest that the parallel
223 shear could be progressively more significant toward the northern and southern domains
224 respectively, according to the orientation of their finite strain ellipses (Fig. 6).

225 **4.1. Rock-avalanche geometry**

226 Multiple rock-avalanche deposits are within the hinge and southern domains of Sierra de
227 la Sobia (Figs. 3 and 6). The largest occurred on the south-western hillslope, and the
228 smallest on the southern hillslope of the mountain range. Frequently, rock-avalanches
229 result from the superposition of multiple destabilizing events. Rock-avalanches in the
230 vicinity of Villa de Sub could have been triggered by a recent re-activation of the right-
231 lateral faults of N150°E-strike (Fig. 6).

232 The geometry and volume estimated for the nine selected rock-avalanche deposits were
233 compared with their respective source areas (Table 1). All these proxies have a reasonable
234 correlation. Avalanches with deposit-volumes $>3 \times 10^6 \text{ m}^3$ have similar vertical drops of
235 ~ 0.7 km on average, whereas avalanches with deposit-volumes $<3 \times 10^6 \text{ m}^3$ have lower
236 vertical drops. Assumptions used in the estimation of areas and volumes result in both
237 being undervalued. This misrepresentation is significant for the source area because the
238 rupture surfaces are usually on high, steep hillslopes. For instance, the rupture scarp of
239 Cueva Güerta is above vertical crags at the outlet of the Páramo River canyon (cross-
240 section D, Fig.4). A maximum depth of ~ 65 m has been measured at this deposit,

241 anomalously high compared to other deposits due to its confinement between the crags
242 of the Páramo River canyon (Table 1; Fig. 3). Geometrical features of the most
243 representative rock-avalanches have allowed the distinguishing of two types relative to
244 size. A detailed analysis of BSD and rock slope mechanics are presented for the rock-
245 avalanches of the Entrago and Carrea (largest) and the Villa de Sub and Cueva Güerta
246 (smallest).

247 **4.2. Structural control and BSD analysis of selected rock-avalanches**

248 The Entrago rock-avalanche is at the boundary between the hinge and southern domains.
249 Its source area lies between 800 and 1100 m above the villages of Entrago and La Plaza
250 (Fig. 7). Rock-slope failure occurred by direct toppling and planar slides, triggered in
251 multiple events. Roughly mapped rupture scars define a triangular planar surface of ~70
252 ha dipping 68° toward $N71^\circ W$. The crown of the avalanche is bound by a right-lateral
253 fault $N19^\circ E$ -strike (Fig. 8). The southern fault tip has 72 m of horizontal strike. The
254 conical accumulation zone (40.75 ha) extends down to the Teverga River. It slopes to
255 $\sim 47^\circ NW$ and the landslide accumulation consists of four superposed minor deposits: an
256 earth flow overlaid by three conic bodies of block accumulations (early, middle, and
257 recent) that still preserve their transverse ridges (Fig. 7). The fracture pattern mapped in
258 the depletion zone of this rock-avalanche (Figs. 6 and 7) allowed the outlining of 612
259 wedges (Fig. 9). A bi-modal BSD is observed, with two size-fractions of wedges. The
260 fine fraction includes wedges with diameters of <20 m, mostly on the rock-buttress failure
261 and usually of triangular shape. However, a large proportion of wedges are rhomboidal.
262 The major axis of the rhomboids is parallel to the active fault ($N19^\circ E$ -strike). In contrast,
263 the wedges of the fine fraction show an anticlockwise rotation (Fig. 9B), with uniform
264 dispersion onto the rupture slope. Rotation is a consequence of the slight obliquity
265 between the wedge orientation and the rupture plane (Fig. 10). The diagram of S against

266 the wedge eccentricity shows small differences between both fractions (Fig. 9C). Wedges
267 of eccentricity 2.5 have $S=0.64$ if triangular or $S=0.46$ when rhomboidal. Wedges run out
268 from the depletion zone, and consequently their roundness tends to increase as indicated
269 by parameter S and their eccentricity. Diagram C (Fig. 9) shows both effects, the
270 difference in shape of each fraction size, and the effect of incipient sliced wedges within
271 the unstable residual relief.

272 The total range of block size r_i is <10 cm to >10 m. However, pebbles <20 cm were not
273 considered in the analysis because of their unrealistic statistical significance. The size
274 distribution of 4805 blocks (the total outlined blocks within the accumulation zone) is
275 presented in a frequency histogram of the normal distribution (Fig. 11A). BSD is not
276 fractal, with a slope change in the best fit regression line of the corresponding log
277 (frequency)-log (radius) histograms at block radius $r_k \sim 1$ m (Fig. 11B). The block sizes
278 $r_k > 1$ m yield $D=2.35$, the usual fractal dimension of limestone fault-rocks and the damage
279 zone of strike-slip and extensional fault zones (Storti et al., 2003). Conversely, the block
280 sizes $r_k < 1$ m yield $D=1.42$, a value frequently observed in small grain size fractions of
281 cataclastic fault rocks (Keulen et al., 2007). Both have an eccentricity of ~ 1.9 and yield
282 $S \sim 0.65$ ($r_k > 1$ m) and $S \sim 0.68$ ($r_k < 1$ m; Fig. 12B), accordingly with increasing block
283 roundness. A comparative BSD analysis between the three overlapped bodies has allowed
284 us to understand the specific contribution of each rock-avalanche outbreak to the total
285 BSD. ~ 1400 blocks in each body were analysed, and all show normal distributions (aspect
286 ratio ~ 0.7). It therefore follows that the early deposit yields a D value that compares better
287 than the latest rock avalanches with the BSD of the total accumulation zone (Fig. 11C).
288 Moreover, D appears time dependent. So, the fractal dimension in large blocks reduces
289 as the relative age of the deposit increases (Fig. 11D-F). Consequently, BSD becomes
290 fractal in the early deposit because the slope rupture at r_k is highly attenuated (Fig. 11F).

291 South of the Entrago rock-avalanche, there are two accumulation bodies of limestone
292 blocks above the villages of Sobrevilla and Carrea, between 650 and 1200 m (Figs. 7, 12
293 and 13). They correspond to medium sized rock-avalanches (Table 1). The current active
294 right-lateral faults that triggered both avalanches are trending NNE and NE respectively,
295 and their kinematics are accommodate the extension along the outer arc as the curvature
296 of the mountain range increases (Fig. 6). These faults create a downthrown block with
297 200 m of maximum vertical slip (longitudinal section A in Fig. 4) with maximum strike
298 separations raised in their respective southern tips. Both faults displace the MSF trace,
299 which cut out of sequence an earlier Variscan thrust, possibly the Tameza Thrust (Fig.
300 1C). The early cemented deposit accumulated about 600 m east of Sobrevilla has its origin
301 in a rockfall (Fig. 13). The number of tension cracks easily visible on Google Earth
302 suggest that more rockfalls are likely to happen.

303 The southern hillslope of Sierra de la Sobia presented three small rock-avalanches: Villa
304 de Sub, Sabariegos, and Busbigre (Table 1). The structure consists of an asymmetric
305 cuscate-lobate anticline-syncline of N-shape folding related to two faults (Fig. 3 and
306 cross-section D in Fig. 4). The Sobia Syncline is a Variscan fault propagation fold related
307 to the Sobia Thrust and then thrust out sequence by the León Fault toward the NE (Fig.
308 4; Alonso et al., 2009). The cuscate anticline is an ESE-verging fault-propagation fold
309 related to a small back thrust that crops out upslope of Villa de Sub (Fig. 14). The structure
310 probably formed to accommodate the tightening within the MSF footwall (Fig. 15 and
311 cross-section D in Fig. 4). Since the Alpine inversion, the structure of the southern domain
312 tilted northward $\sim 30^\circ$. The occurrence of small rock-avalanches seems to be related to
313 Quaternary deformation. The rock-avalanches are controlled by penetrative vertical
314 planes (J_{p1}) trending N125-150°E, parallel to the general trend of the most significant
315 structures (Fig. 3). Some fractures have sub-horizontal slickenlines according to right-

316 lateral kinematics (F_{p1}), and they control the rupture scarps of rock-avalanches. Such local
317 kinematics are consistent with the whole kinematic model proposed for Sierra de la Sobia
318 (Fig. 6). The main accumulation of the Villa de Sub rock-avalanche has three overlapped
319 deposits, with the lowest composed of calcite-coated limestone blocks. The middle and
320 upper deposits have two overlapped fans. Additional blocks were incorporated during the
321 last instability events with little change in the fan shape (Fig. 15A): a rock-fall triggered
322 in 2004, synchronously with an earthquake of Ms 2; and a co-seismic 4.1 Ms rock-fall in
323 1996 (Fig. 1B). BSD of the Villa de Sub rock-avalanche is not fractal, with a slope change
324 also at block radius $r_k \sim 1$ m (Fig. 12A). The block sizes $r_k > 1$ m yield $D=2.53$ ($R^2=0.92$ to
325 the fitted regression line). Conversely, the block sizes $r_k < 1$ m yield $D=1.25$ ($R^2=0.98$).
326 Both sizes have similar low eccentricity of ~ 1.6 and roundness of $S \sim 0.73$ (Fig. 12B)
327 respectively, with a relatively lower vertical drop of rock-fall and a lower impact
328 compared to larger rock-avalanches (Table 1).

329 Finally, a small rock-avalanche located at the northern entrance of Cueva Güerta at the
330 spring of Foz de la Estruchura has been analysed in detail. Most accumulation bodies
331 triggered along this canyon are confined by two opposite facing crags that bound the
332 narrow course of the river. Both the cave conduits and the river course lie parallel,
333 trending N-S along the damage zone of the MSF (Fig. 14). BSD in the accumulation body
334 of Cueva Güerta is not fractal, with a slope change also at $r_k < 1$ m (Fig. 12A). The block
335 sizes $r_k > 1$ m yield $D=2.70$. Conversely, the block sizes $r_k < 1$ m yield $D=0.54$, but with low
336 confidence. Both sizes have a low eccentricity of ~ 1.6 , but the coarse fraction includes
337 less rounded blocks ($S \sim 0.68$), than the finer fraction ($S \sim 0.72$). The coarse fraction has the
338 highest D among the populations analysed in Sierra de la Sobia. It shows lower particle
339 fragmentation (higher D) than the other unconfined accumulation bodies. Low

340 fragmentation is consistent with a progressive increment of relatively fine blocks towards
341 the top of the confined accumulation, caused by gravity selection.

342 **4.3. Slope stability analysis**

343 The stability models for all the slopes analysed assumed a conservative friction angle of
344 35° on the joint surfaces. The slope stability above the Entrago rock-avalanche was
345 analysed based on the orientation of 85 fractures measured along the rupture scarp,
346 controlled by the right-lateral fault of N19°E-strike. The mechanical instability of the
347 rupture scarp was evaluated under different dynamic failure modes (Fig. 10). Visual
348 estimates indicate <6% risk for planar sliding, <16% direct toppling risk for joint sets J_{r1},
349 and J_{r2}, <16% flexural toppling risk for joint sets J_{r1} and <13% wedge sliding risk.
350 Although the dynamic analysis gives a low risk of instability, the slope records at least
351 four superposed landslide deposits (Fig. 7). The models have a slope safety factor of <1.3
352 only when running with horizontal peak ground accelerations (PGA)>0.10-0.15 g, within
353 the prediction of the 2013 European Seismic Hazard Map for north-western Iberia
354 (Giardini et al., 2014).

355 84 mechanical discontinuities (25 S₀, 3 F_r, 1 F_p, 23 J_p, 18 J_{r1}, 6 J_{r1}, 6 J_{r2} and 2 J_{r2})
356 measured on the rupture plane of the Carrea rock-avalanche have been considered for the
357 slope stability analysis. The fracture pattern lies parallel to both the Variscan thrusts and
358 an active transverse fault, and a rupture slope with dip direction 237/50 is considered for
359 the stability models. Considering these surface conditions there is a 0% risk for flexural
360 toppling, <4% risk for planar sliding, <11% risk for direct toppling and wedge sliding.
361 All these models indicate slightly higher safety factors than for the Entrago rock-
362 avalanche, even though a safety factor of <1.3 may arise with horizontal PGA>0.15 g.

363 123 mechanical discontinuities (45 S₀, 1 F_r, 7 F_p, 35 J_p, 23 J_{r1}, 8 J_{r1'}, 1 J_{r2} and 3 J_{r2'})
364 measured on the rupture plane of Villa de Sub were considered for the slope stability
365 analysis. A penetrative fracture pattern lies parallel to the active right-lateral fault and
366 normal to the S₀ trend. The rupture slope modelled has a 173/80 dip direction and tilts
367 opposite to S₀. The dynamic analysis gives risks of <8% for flexural toppling, <9% for
368 planar sliding, <24 % for direct toppling and <19% for wedge sliding. The models
369 provided lower safety factors than for the Entrago rock-avalanche, even though a safety
370 factor of <1.3 may arise with horizontal PGA>0.10 g.

371 Only a dynamical slope stability analysis has been carried on the external Cueva Güerta
372 avalanche. 52 discontinuities (5 S₀, 8 F_r, 18 F_p, 6 J_p, 9 J_{r1}, 1 J_{r1'}, 4 J_{r2}, and 1 J_{r2'}) measured
373 around the north cave entrance were considered in the slope stability analysis. Two planes
374 with dip directions 20/90 and 87/90 define the rupture slope, and consequently two
375 dynamic analyses of the respective slope stability risk have been considered. These
376 indicate risks of <14 and 25% for flexural toppling, <8 and 14% for planar sliding, <21
377 and 27% for direct toppling, and <24 and 26% for wedge sliding, with dip directions
378 20/90 and 87/90 respectively. Slope stability models created with the dip direction 87/90
379 give lower safety factors than those for 20/90. Both models have lower safety factors than
380 any other rock-avalanche case studies, even though >1.3 has been obtained for all rupture
381 slopes modelled in this work.

382 **4.4. Timing of rock-avalanche events**

383 Calcite coating the blocks within the oldest calcareous rock-avalanche of the Entrago
384 deposit was successfully dated in samples RB_5, RB_6, and RB_7 (Fig. 7, Table 2).
385 Samples RB_5 and RB_6 taken along the transverse frontal ridge of the conical cemented
386 deposit, yielded ages of 13.7±0.9 and 278.3±32.9 ka coeval to marine isotope stages MIS-

387 1 and MIS-9a, respectively. Sample RB_7 from the toe of the deposit, yields 194.3 ± 70.2
388 ka, indicating cementation during MIS-7a.

389 In the case of the Sobrevilla deposit, a minimum U/Th age of ~ 100 ka has been reported
390 (Fig. 13; Rodríguez-Pérez, 2012). Sample RB_2 taken at the accumulation body of the
391 Carrea avalanche yields an age of 58.8 ± 14.6 ka, coeval to MIS 3-4 (Table 2), while RB_9
392 yields a minimum age of 38.3 ± 2.8 ka, coeval to MIS 3 (Table 3). Based on the U/Th
393 dates, the Sobrevilla rock-avalanche occurred earlier than the Carrea rock-avalanche, but
394 later than the main event that caused the Entrago rock-avalanche. Radiometric ages are
395 consistent with the evolution of the BSD observed between the three overlapped deposits
396 in the avalanche. So, the Carrea rock-avalanche has BSD with a sharper slope break than
397 the Entrago one (Fig. 12A). The blocks within the accumulation body are also more
398 irregular than those in the Entrago avalanche, as shown by parameter S (Fig. 12B).

399 Sample RB_03 taken from a calcite cement coating a block at the Cueva Güerta rock
400 failed to provide a reliable age (Table 2). A replica of that sample, RB_10, yields a
401 minimum age of 9.9 ± 1.2 ka (Table 3). Based on the U/Th results, Cueva Güerta is the
402 youngest dated rock-avalanche until now in Sierra de la Sobia. Its bi-log frequency-size
403 diagram shows a greater slope rupture between the two block fractions (Fig. 12A).
404 According to the tendency observed between the diagrams in the Entrago rock-avalanche
405 (Figs. 11D, E, and F), the slope rupture (Fig. 12A) is also consistent with the young age
406 obtained in the Cueva Güerta avalanche.

407 **5. Discussion**

408 The impact of our results is discussed below, addressing the following: 1) current
409 tectonics in Sierra de la Sobia; 2) origin and recurrence of rock-avalanches; 3) Quaternary
410 geomorphological evolution of the landscape.

411 **5.1 Current tectonics in Sierra de la Sobia**

412 The kinematic analysis of active faults, as well as their slip inversion, is consistent with
413 a re-tightening by horizontal shortening accordingly with a N-S trending SH_{max} (Fig. 6).
414 Current strain gave rise to the stretching along the western outer arc of the range,
415 throughout the activation of strike-slip faults but also reverse and minor normal-scissor
416 faults that accommodate deformation at the surface. In contrast, at depth, this intensely
417 fractured zone is probably linked to the León Fault as indicated by the fracture network,
418 the fault trends and their distribution compared to the trace of the León Fault. However,
419 some of the minor active faults also displace the main trace of the León Fault (Figs. 3 and
420 4). These structural features might raise questions about the current activity of this fault.
421 However, we have observed that current tectonics related to the León Fault likely
422 triggered the slope failures recurrently, both in the outer arc of Sierra de la Sobia and
423 along the whole southern branch of this fault (Figs. 1B and 2). Moreover, several low
424 seismic signals have recently been recorded at a depth of ~15 km near the intersection of
425 the León and Ventaniella Faults (López- Fernández et al., 2018). Therefore, we consider
426 that the most recent minor faults showing cut off relationships with the León Fault trace
427 are a consequence of the growth fracture density along the main fault trace and the
428 dissipation of the current differential stress along such new fault planes.

429 The summit elevation in Sierra de la Sobia progressively increases southwards, showing
430 a constant slope of 1.5° from 1350-1776 m (Saleras peak; Figs. 2 and 5). The restored
431 section A (Fig. 4) has given a maximum current extension of 300 m of the outer arc of
432 the range. The progressive uplift of the range southward led to the reactivation of the
433 Variscan lateral ramp and the development of several high angle faults trending E-W at
434 the junction between the MSF and the Trobaniello segment fault (Fig. 6). Finally, the
435 current brittle strain partition in the southern domain of Sierra de la Sobia accommodated

436 right-lateral minor faults N150°E-strike as well as other conjugated faults that likely
437 caused smaller avalanches (Fig. 6). The larger avalanches triggered northward suggest
438 that Quaternary seismicity is higher in the hinge domain of Sierra de la Sobia and
439 diminishes southward.

440 It is reasonable to extend the current tectonics of Sierra de la Sobia to CZ, as a working
441 hypothesis. Because this arcuate mountain range lies parallel to the León Fault, the fault
442 trace eastward prolonged according to CA orocline (Fig.1), and along the whole trace of
443 the León Fault has recorded rock-avalanches and complex flows like those described
444 above (Fig. 2). Moreover, CZ has other active structures that support this statement. One
445 is the Variscan Tineo Thrust, westward of the Cenozoic basin of Oviedo. This trends NE-
446 SW accordingly with the CA, and it was reactivated, thrusting over Cenozoic sediments
447 south-eastward (Fig. 1B; Pulgar et al., 1999). Another case is the Boinás Thrust (Fig. 1B;
448 de Vicente Muñoz et al., 2007). It trends parallel to the Tineo Thrust but back thrusts
449 north-westward 350 m. The Tineo Thrust and the reverse fault described in the Marabio
450 Pass (Fig. 6; Fernández et al., 2018) have the same kinematics. In both cases, tectonics
451 seem to accommodate the deformation after the unfolding limb section of regional
452 Variscan folds parallel to the CA by horizontal shortening parallel to their respective axes
453 accordingly with the regional trends of SH_{max} (de Vicente et al., 2008; Custódio et al.,
454 2015). Eastward, the fault junction between the León and Ventaniella faults (Fig. 1B)
455 recorded recent low-magnitude earthquakes (López- Fernández et al., 2018). The
456 clustering of earthquakes along these faults coincides spatially at depth with the transition
457 zone. The seismicity of the Ventaniella fault is fragmented, having only moderate seismic
458 records at the northern onshore segment and south of the fault's junction, whereas the
459 central segment is aseismic.

460 CA is divided into two tectonic units by the Ventaniella Fault. The current deformation
461 in the western tectonic unit appears controlled by the arcuate shape of the orocline.
462 Normal faults accommodate stretching, parallel to the arc. Strike-slip faults transverse to
463 the arc accommodate the N-S shortening, and back-thrusts towards the outer-arc
464 accommodate the subsequent migration of the neutral surface predicted for the
465 longitudinal tangential folding mechanism (Fig. 1B). Variscan and Alpine structures east
466 of the Ventaniella Fault have a linear trend E-W and they can accommodate the current
467 regional SH_{max} easily with straight displacement southward. However, because the CA
468 controls the Quaternary reactivation, deformation is partitioned in transtensive basins
469 controlled by right faults trending NW-SE parallel to the Ventaniella Fault. Finally,
470 according to the crustal thickness variation, the aseismic central segment might be
471 interpreted as the current strain rate, progressing more efficiently toward the flanks of the
472 orocline than in its core (Díaz et al., 2016; Díaz and Gallart, 2009).

473 The topography of the crust-mantle boundary is also interpreted as evidence of a passive
474 margin (Cadenas et al., 2018; Fernández-Viejo et al., 2000; López-Fernández et al., 2020)
475 or as the earliest initiation of ocean-continent subduction (Álvarez-Marron et al., 1997;
476 Ayarza et al., 2004; Díaz and Gallart, 2009; Gallastegui et al., 2016). In our opinion,
477 surface topographic features such as marine terraces are not only dependent on the crust
478 thickness as postulated in López-Fernández et al. (2020) but also on the elastic thickness
479 of the whole lithosphere (Burov and Diament, 1995; François et al., 2013). It is
480 noteworthy that the Quaternary kinematics of the active fault analysed in Sierra de la
481 Sobia consist of tangential deformation (Fig. 6), although normal faulting is associated
482 with isostatic balance in passive margins (Conway-Jones et al., 2019; Pederson et al.,
483 2002). The reverse and strike-slip fault kinematics prevail against the current normal
484 faults, mostly locate radially to the outer-arc at the hinge domain of Sierra de la Sobia.

485 Most of the active fault mapped along the Cantabrian wave-cut paleo-platform by
486 Álvarez-Marrón et al. (2008) indicate consistent kinematics with our study area.

487 **5.2 Rock-avalanches: origin and recurrence**

488 Rock fragmentation, weathering, climatic factors, and geomorphological factors, during the
489 withdrawal of glaciers and associated debuttrressing have been described as the triggers of large
490 rock-avalanches (Ambrosi and Crosta, 2011; Ballantyne et al., 2014; Turcotte, 1986).
491 Additionally, in many rock-avalanches, seismicity is the main triggering factor: avalanches
492 triggered by recent (Wasowski et al., 2021) or historical earthquakes (Martin et al., 2014; Zeng et
493 al., 2020) or polyphase rock-avalanches that are consistent with sedimentological paleoseismic
494 records (Grämiger et al., 2016).

495 Slope failure analyses demonstrate that under static conditions the main rupture scarps of
496 the rock-avalanches on the Sierra de la Sobia are mechanically stable (Fig.10) and
497 consequently differential stress must be increased for dynamic fragmentation. Moreover,
498 the BSD analysis shows $r_k > 1$ m for all the rock-avalanche deposits yield D ranging
499 between 2.24 and 2.70 (Table 1), into the usual range of dynamic fragmentation (Storti et
500 al., 2003). Therefore, similar two-stage breakage dynamic processes caused the block
501 fragmentation within all rock-avalanches: (i) dynamic and ballistic fragmentation from
502 the aftershock rupture scarp; and (ii) fragmentation by wear and attrition from the scar
503 slope to the accumulation body, causing the BSD-homogenization within the block size
504 fractions $r_i < 1$ m. The block size at the slope change (r_k) seems to represent a change in
505 the dominant fragmentation mechanism from (i) to (ii). D variations can be interpreted
506 because of the percentage weight of fine to coarse fragments in each respective fraction.
507 So, decreasing particle fragmentation occurred in confined accumulation bodies only
508 because the surface of the accumulation body is considered for the BSD analysis (see
509 methods), where the percentage weight of fine fragments is higher than at the bottom.

510 Consequently, D for $\text{Logr}_k > 1$ is higher in the accumulation body of Cueva Güerta
511 compared to other avalanches (Fig. 12, Table 1). Selection can also be evaluated
512 indirectly by the difference of the roundness versus eccentricity between the fine and
513 coarse fractions of each BSD (Fig. 12B). More selection is expected at the top of the
514 accumulation body than at the tip. For instance, the BSD of Carrea avalanche shows the
515 greatest segregation because only the top sector of the accumulation body is considered,
516 whereas in other avalanches the whole accumulation body is well exposed and
517 consequently used for BSD analysis. This feature is also consistent with the relative ages
518 inferred from BSD. The accumulation body of the largest avalanches is composed of
519 several superposed deposits of horizontal conic shape, where the most recent deposit is
520 located at the top of the accumulation body. The detailed BSD of the Entrago avalanche
521 shows a progressive attenuation of the logr_k -slope rupture as the relative age of the BSD
522 deposit increases (Fig. 11). If the BSD of the analysed avalanches is compared, according
523 to this criterion, Entrago is the oldest rock-avalanche in the Sierra de la Sobia and Cueva
524 Güerta the youngest (Fig. 12A). This relative chronology is consistent with the U/Th ages
525 obtained from the coated calcite blocks sampled in these accumulation bodies (Tables 2
526 and 3).

527 At least three superposed deposits of blocks have been differentiated at the map-scale on
528 the massive avalanches of Sierra de la Sobia (Figs. 7 and 13), along a fault segment ~4.5
529 km length, suggesting that such avalanches record the same seismic events. Moreover,
530 co-seismic rock-falls have been recorded near Villa de Sub (Fig. 14). However,
531 destructive to very destructive events, ranging between VIII to X in the environmental
532 seismic intensity scale (Michetti et al., 2007) could be inferred accordingly, with: (i) the
533 offset and length of the active faults; (ii) the evaluated tectonic uplift and subsidence
534 (Figs. 3, 4, 6); (iii) the length and width of the ground cracks and the reach of slope

535 movements (Figs. 7, 13, 14, Table 1); and (iv) the affected area and type of record
536 (Reicherter et al., 2009). Recently, the empirical power-law relationships between the
537 total volume of the avalanche and the seismic magnitude (Keefe, 1999) were validated
538 (Croissant et al., 2017). However, this approach is challenging to apply in this study area
539 because it is impossible to evaluate which avalanche volume corresponds to each
540 paleoseismic event. Also, for short-term recurrence, the total volume could decrease as
541 the rupture scarp becomes more stable during aftershocks. Currently, the slope stability
542 analyses indicate that a horizontal PGA ranging between 0.10-0.15 g is required to disrupt
543 such scarps again. Sierra de la Sobia experiences moderate seismicity, characterized by
544 frequent $M_s < 6$ events, because of its geodynamic setting (Álvarez-Marrón et al., 1997;
545 Ayarza et al., 2004; Díaz and Gallart, 2009; Gallastegui et al., 2016). In this context, the
546 largest earthquakes generated in the past might occur within recurrence intervals much
547 longer than the period covered by both the historical and instrumental local records (Fig.
548 1B) and could be conditioned by the reactivation of the long-lived crustal León Fault at a
549 slow slip rate during the re-tightening of the CA under NNW-SSE compression. Further
550 work is necessary for insight into the standard $\log r_k = 1$ for all the BSDs analysed (Fig.
551 12A). Samples have been collected from the non-cemented rock-avalanches at Entrago
552 and Carrea to broaden the chronological framework presented here by ^{36}Cl cosmic-ray
553 exposure dating. The accurate date of the latest avalanche-events might help forecast
554 future massive earthquakes in the region.

555 Based on the oldest calcite cement, a reference age of 278.3 ± 32.9 ka is inferred for the
556 oldest cementation episode affecting the Entrago deposit, and hence a minimum age for
557 the oldest rock-avalanche event. Subsequent avalanche cementation occurred thereafter,
558 spanning the last 200 ka, potentially conditioned by Quaternary climate changes. Calcite
559 growth took place preferentially during the interglacials, and during the warm periods

560 that bounded the MIS-3 glacial advance of the Cantabrian Mountains (Rodríguez-
561 Rodríguez et al., 2015).

562 **5.3 Quaternary geomorphological evolution of the landscape**

563 The western hillslope of the Sierra de la Sobia is a structural form controlled by the
564 arcuate orientation of the limestone bedding and MSF. Compression of this mountain
565 range according to the current regional NNW SH_{max} (de Vicente et al., 2008; Custódio et
566 al., 2015) triggered several rock-avalanches with recurrent avenues along the Quaternary
567 period. This active tectonic process strongly conditioned the geomorphology of the
568 Teverga Valley.

569 In this period, the incision rate of the Páramo River may have accelerated as suggested
570 by the cusate shape of the river valley throughout the Foz de la Estrechura canyon (Fig.
571 14). The current course is incised ca 30 m from the paleo-epiphreatic sediment deposited
572 on the upper entrance of Cueva Güerta. The current phreatic level runout ca 100 m below
573 the paleo-phreatic level is defined along the low gradient of the longest gallery in this
574 cave (Ferrerías et al., 2015). However, the accumulation of the rock avalanche confined
575 at the spring of the canyon did not dam the stream. This is because, at that time, the flow
576 of water was underground, and its runout was at a deeper level.

577 Downstream is the old village of Fresneu, which was destroyed on June the 25th 1522.
578 Canon Tirso de Avilés of Oviedo Cathedral tells of an earthquake event, after which a
579 new village was built at the current site (Fig. 14). Moreover, the Entrago avalanche
580 dammed the Val de Cazana, Taja and Páramo Rivers (Fig. 3), deviated the resultant course
581 of the Teverga River at the entrance of the Val de Cerezales canyon, and developed the
582 only floodplains present in this valley (Fig. 7).

583 A detailed analysis of this river sub-basin extended to the whole Nalón basin that would
584 give new insights into understanding the Quaternary geomorphology and tectonics of the
585 Cantabrian Mountains is currently underway.

586 **6. Conclusions**

587 The Quaternary reactivation of minor faults lying along the MSF-trace has
588 accommodated ~300 m uplift of the summits in Sierra de la Sobia. Their slip inversion is
589 consistent with a current N-S trend of the SH_{max} that contributes to the re-tightening of
590 this arcuated mountain range and the stretch of its outer arc also ~300 m by longitudinal
591 tangential deformation.

592 The largest rock-avalanches are distributed along the hinge domain of Sierra de la Sobia,
593 while the smallest are in the southern domain. The sizes of rock-accumulation bodies are
594 proportional to the corresponding vertical drop. BSDs of the accumulation bodies are not
595 fractal. The largest block size fractions ($r_i > 1$ m) have slope D-values ranging between
596 2.70 and 2.24, whereas the block size fractions $r_i < 1$ m have lower D-values.

597 The mechanical slope stability analysis of relevant rupture scarps reported safety factors
598 > 1.3 under static boundary conditions. However, all rupture scarps become unstable if
599 horizontal seismic acceleration rises 0.10-0.15 g.

600 Chronological U/Th data obtained from calcium carbonate cements bounding limestone
601 blocks in the Entrago, Carrea and Cueva Güerta rock-avalanches suggest recurrent
602 instability events for at least the last 300 ka, with episodic cementation occurring during
603 the last five interglacials.

604 Geomorphological and structural data gathered on the western flank of Sierra de la Sobia
605 reveal unambiguously a clear relationship between current tectonics and recurrent
606 catastrophic rock-avalanches.

607 **Acknowledgments**

608 Research funded by the Spanish Ministry of Education and Science, through project
609 CGL2015-66997-R from the National Research plan, and by the FC-GRUPIN-
610 IDI72018/000216 project of the Principado de Asturias government. We thank Lawrence
611 Edwards and Hai Cheng for allowing the use of their facilities to perform the U/Th dating,
612 completed at the University of Minnesota. We would also like to thank for the review of
613 paleo-stress by Gerardo de Vicente, the structural discussion and field reviews with Juan
614 Luis Alonso, and the review of the English text by Andy Whitehead. Finally, we also
615 thank the Editor and the two anonymous reviewers for their valuable comments and
616 remarks.

617

618 **References**

- 619 Alonso, J.L., Marcos, A., Suárez, A., 2009. Paleogeographic inversion resulting from large out
620 of sequence breaching thrusts: The León Faults (Cantabrian Zone, NW Iberia). A new
621 picture of the external Variscan Thrust Belt in the Ibero-Armorican Arc. *Geol. Acta* 7,
622 451–473. <https://doi.org/10.1344/105.000001449>
- 623 Alonso, J.L., Martínez-Abad, I., García-Ramos, J.C., 2007. Nota sobre la presencia de una
624 sucesión cretácica en el Macizo de Las Ubiñas (Cordillera Cantábrica). *Implicaciones*
625 *tectónicas y geomorfológicas. Geogaceta* 47–50.
- 626 Álvarez-Marrón, J., Hetzel, R., Niedermann, S., Menéndez, R., Marquínez, J., 2008. Origin,
627 structure and exposure history of a wave-cut platform more than 1 Ma in age at the coast
628 of northern Spain: A multiple cosmogenic nuclide approach. *Geomorphology* 93, 316–
629 334. <https://doi.org/10.1016/j.geomorph.2007.03.005>
- 630 Álvarez-Marron, J., Rubio, E., Torne, M., 1997. Subduction-related structures in the North
631 Iberian Margin. *J. Geophys. Res. Solid Earth* 102, 22497–22511.
632 <https://doi.org/10.1029/97jb01425>
- 633 Ambrosi, C., Crosta, G.B., 2011. Valley shape influence on deformation mechanisms of rock
634 slopes. *Geol. Soc. London, Spec. Publ.* 351, 215 LP – 233.
635 <https://doi.org/10.1144/SP351.12>
- 636 Ayarza, P., Catalán, J.R.M., Alvarez-Marrón, J., Zeyen, H., Juhlin, C., 2004. Geophysical
637 constraints on the deep structure of a limited ocean-continent subduction zone at the North
638 Iberian Margin. *Tectonics* 23, TC1010. <https://doi.org/10.1029/2002TC001487>
- 639 Ballantyne, C.K., Sandeman, G.F., Stone, J.O., Wilson, P., 2014. Rock-slope failure following
640 Late Pleistocene deglaciation on tectonically stable mountainous terrain. *Quat. Sci. Rev.*
641 86, 144–157. <https://doi.org/10.1016/j.quascirev.2013.12.021>
- 642 Bastida, F., Castro, S., 1988. Estructura del sector septentrional de la Escama de Tameza (Zona
643 Cantábrica, NW de España). *Trab. Geol.* 17, 67–85.
- 644 Bischoff, J.L., Julia, R., Mora, R., 1988. Uranium-series dating of the Mousterian occupation at
645 Abric Romani, Spain. *Nature* 332, 68–70. <https://doi.org/10.1038/332068a0>
- 646 Bulnes, M., Aller, J., 2002. Three-dimensional geometry of large-scale fault-propagation folds
647 in the Cantabrian Zone, NW Iberian Peninsula. *J. Struct. Geol.* 24, 827–846.
648 [https://doi.org/10.1016/S0191-8141\(01\)00114-6](https://doi.org/10.1016/S0191-8141(01)00114-6)
- 649 Bulnes, M.T., 1994. La estructura geológica del Valle del Rio Trubia (Zona Cantábrica, NO de
650 España). Unpubl. PhD Thesis. Universidad de Oviedo.
- 651 Burov, E.B., Diament, M., 1995. The effective elastic thickness (T_e) of continental lithosphere:
652 What does it really mean? *J. Geophys. Res. Solid Earth* 100, 3905–3927.
653 <https://doi.org/10.1029/94JB02770>
- 654 Cadenas, P., Manatschal, G., Fernández-Viejo, G., Welford, J.K., 2018. Margin segmentation
655 during polyphase rifting in the southern Bay of Biscay. *Atl. Geol.* 54, 409–470.
656 <https://doi.org/10.4138/atlgeol.2018.014>
- 657 Conway-Jones, B.W., Roberts, G.G., Fichtner, A., Hoggard, M., 2019. Neogene Epeirogeny of
658 Iberia. *Geochemistry, Geophys. Geosystems* 20, 1138–1163.
659 <https://doi.org/10.1029/2018GC007899>
- 660 Croissant, T., Lague, D., Steer, P., Davy, P., 2017. Rapid post-seismic landslide evacuation
661 boosted by dynamic river width. *Nat. Geosci.* 10, 680–684.

- 662 <https://doi.org/10.1038/ngeo3005>
- 663 Custódio, S., Dias, N.A., Carrilho, F., Góngora, E., Rio, I., Marreiros, C., Morais, I., Alves, P.,
664 Matias, L., 2015. Earthquakes in western Iberia: Improving the understanding of
665 lithospheric deformation in a slowly deforming region. *Geophys. J. Int.* 203, 127–145.
666 <https://doi.org/10.1093/gji/ggv285>
- 667 de Vicente, G., Cloetingh, S., Muñoz-Martín, A., Olaiz, A., Stich, D., Vegas, R., Galindo-
668 Zaldívar, J., Fernández-Lozano, J., 2008. Inversion of moment tensor focal mechanisms
669 for active stresses around the microcontinent Iberia: Tectonic implications. *Tectonics* 27,
670 1–22. <https://doi.org/10.1029/2006TC002093>
- 671 de Vicente Muñoz, G., González-Nistal, S., Muñoz-Martín, A., Vegas, R., Olaiz, A., Fernández-
672 Lozano, J., de Vicente, R., 2007. El cabalgamiento cenozoico de Boinás (Cordillera
673 Cantábrica, España). *Geogaceta* 42, 7–10.
- 674 Delavaud, E., Cotton, F., Akkar, S., Scherbaum, F., Danciu, L., Beauval, C., Drouet, S.,
675 Douglas, J., Basili, R., Sandikkaya, M.A., Segou, M., Faccioli, E., Theodoulidis, N., 2012.
676 Toward a ground-motion logic tree for probabilistic seismic hazard assessment in Europe.
677 *J. Seismol.* 16, 451–473. <https://doi.org/10.1007/s10950-012-9281-z>
- 678 Díaz, J., Gallart, J., 2009. Crustal structure beneath the Iberian Peninsula and surrounding
679 waters: A new compilation of deep seismic sounding results. *Phys. Earth Planet. Inter.*
680 173, 181–190. <https://doi.org/10.1016/j.pepi.2008.11.008>
- 681 Díaz, J., Gallart, J., Carbonell, R., 2016. Moho topography beneath the Iberian-Western
682 Mediterranean region mapped from controlled-source and natural seismicity surveys.
683 *Tectonophysics* 692, 74–85. <https://doi.org/10.1016/j.tecto.2016.08.023>
- 684 Epstein, B., 1947. The mathematical description of certain breakage mechanisms leading to the
685 logarithmico-normal distribution. *J. Franklin Inst.* 244, 471–477.
686 [https://doi.org/10.1016/0016-0032\(47\)90465-1](https://doi.org/10.1016/0016-0032(47)90465-1)
- 687 Fernández-Viejo, G., Gallart, J., Pulgar, J.A., Córdoba, D., Dañobeitia, J.J., 2000. Seismic
688 signature of Variscan and Alpine tectonics in NW Iberia: crustal structure of the
689 Cantabrian Mountains and Duero basin. *J. Geophys. Res.* 105, 3001–3018.
- 690 Fernández-Viejo, G., López-Fernández, C., Domínguez-Cuesta, M., Cadenas, P., 2014. How
691 much confidence can be conferred on tectonic maps of continental shelves? the
692 Cantabrian-Fault case. *Sci. Rep.* 4, 1–7. <https://doi.org/10.1038/srep03661>
- 693 Fernández, F.J., Alonso, J.L., Pando, L., 2018. Evidence for quaternary tectonic activity in the
694 western cantabrian Zone (Passes of Marabio, Sobia nappe). *Geogaceta* 64, 1–3.
- 695 Fernández, F.J., Menéndez-Duarte, R., Aller, J., Bastida, F., 2005. Application of Geographical
696 Information Systems to shape-fabric analysis, in: Bruhn, D., Burlini, L. (Eds.), *High-Strain*
697 *Zones: Structure and Physical Properties*. Geological Society, London, Special
698 Publications, London, pp. 409–420. <https://doi.org/10.1144/GSL.SP.2005.245.01.20>
- 699 Ferreras, S., Franco, J., Fresnadiello, A., Rojo, D., Turmo, A., Álvarez, A., Álvarez, M.,
700 Ballesteros, D., Cañón, G., 2015. Avance en 2015 al estudio espeleológico de Cueva
701 Güerta. *Frenéu*, Concejo de Terverga. Asturias. Colectivo Asturiano de Espeleólogos.
- 702 Fillon, C., Pedreira, D., Van Der Beek, P.A., Huisman, R.S., Barbero, L., Pulgar, J.A., 2016.
703 Alpine exhumation of the central Cantabrian Mountains, Northwest Spain. *Tectonics* 35,
704 339–356. <https://doi.org/10.1002/2015TC004050>
- 705 François, T., Burov, E., Meyer, B., Agard, P., 2013. Surface topography as key constraint on
706 thermo-rheological structure of stable cratons. *Tectonophysics* 602, 106–123.
707 <https://doi.org/10.1016/j.tecto.2012.10.009>

- 708 Gallastegui, J., Pulgar, J.A., Gallart, J., 2016. Alpine tectonic wedging and crustal delamination
709 in the Cantabrian Mountains (NW Spain). *Solid Earth* 7, 1043–1057.
710 <https://doi.org/10.5194/se-7-1043-2016>
- 711 Giardini, D., Wössner, J., Danciu, L., 2014. Mapping Europe's Seismic Hazard. EOS,
712 *Transactions. Am. Geophys. Union* 95, 261–268. <https://doi.org/10.1002/2014EO290001>
- 713 Goodman, R.E., 1989. *Introduction to rock mechanics*. John Wiley & Sons, Toronto.
- 714 Grämiger, L.M., Moore, J.R., Vockenhuber, C., Aaron, J., Hajdas, I., Ivy-Ochs, S., 2016. Two
715 early Holocene rock avalanches in the Bernese Alps (Rinderhorn, Switzerland).
716 *Geomorphology* 268, 207–221. <https://doi.org/10.1016/j.geomorph.2016.06.008>
- 717 Hallstadius, L., 1984. A method for the electrodeposition of actinides. *Nucl. Instruments*
718 *Methods Phys. Res.* 223, 266–267. [https://doi.org/10.1016/0167-5087\(84\)90659-8](https://doi.org/10.1016/0167-5087(84)90659-8)
- 719 Heim, A., 1932. *Bergsturz und Menschenleben*, Fretz und Wasmuth. Zürich, 218 pp.
- 720 Hudson, J.A., Harrison, J.P., 1997. *Engineering rock mechanics: an introduction to the*
721 *principles*. Elsevier, Oxford.
- 722 Keefer, D.K., 1999. Earthquake-induced landslides and their effects on alluvial fans. *J.*
723 *Sediment. Res.* 69, 84–104. <https://doi.org/10.2110/jsr.69.84>
- 724 Keulen, N., Heilbronner, R., Stünitz, H., Boullier, A.M., Ito, H., 2007. Grain size distributions
725 of fault rocks: A comparison between experimentally and naturally deformed granitoids. *J.*
726 *Struct. Geol.* 29, 1282–1300. <https://doi.org/10.1016/j.jsg.2007.04.003>
- 727 Lefort, J.-P., 1989. *Basement correlation across the North Atlantic*. Springer-Verlag Berlin
728 Heidelberg. <https://doi.org/10.1007/978-3-642-73350-5>
- 729 López-Fernández, C., Llana-Fúnez, S., Fernández-Viejo, G., Domínguez-Cuesta, M.J., Díaz-
730 Díaz, L.M., 2020. Comprehensive characterization of elevated coastal platforms in the
731 north Iberian margin: A new template to quantify uplift rates and tectonic patterns.
732 *Geomorphology* 364. <https://doi.org/10.1016/j.geomorph.2020.107242>
- 733 López- Fernández, C., Fernández- Viejo, G., Olona, J., Llana- Fúnez, S., 2018. Intraplate
734 Seismicity in Northwest Iberia along the Trace of the Ventaniella Fault: A Case for Fault
735 Intersection at Depth. *Bull. Seismol. Soc. Am.* 108, 604–618.
736 <https://doi.org/10.1785/0120170215>
- 737 Lotze, F., 1945. Zur Gliederung der Varisziden der Iberischen Meseta. *Geotektonische*
738 *Forschungen* 6, 78–92.
- 739 Marcos, A., Pulgar, J.A., 1982. An approach to the tectonostratigraphic evolution of the
740 Cantabrian foreland thrust and fold belt, Hercynian Cordillera of NW Spain. *Neues Jahrb.*
741 *für Geol. und Paläontologie Abhandlungen* 163, 256–260.
- 742 Martin, S., Campedel, P., Ivy-Ochs, S., Viganò, A., Alfimov, V., Vockenhuber, C., Andreotti,
743 E., Carugati, G., Pasqual, D., Rigo, M., 2014. Lavini di Marco (Trentino, Italy): 36Cl
744 exposure dating of a polyphase rock avalanche. *Quat. Geochronol.* 19, 106–116.
745 <https://doi.org/10.1016/j.quageo.2013.08.003>
- 746 Menéndez-Duarte, R., Marquínez, J., Fernández-Menéndez, S., Santos, R., 2007. Incised
747 channels and gully erosion in Northern Iberian Peninsula: Controls and geomorphic
748 setting. *Catena* 71, 267–278. <https://doi.org/10.1016/j.catena.2007.01.002>
- 749 Merino-Tomé, O., Suárez, Á., Alonso, J.L., González-Menéndez, L., Heredia, N., Marcos-
750 Vallauré, A., 2011. Mapa Geológico Digital continuo E. 1:50000, Principado de Asturias
751 (Zonas: 1100-1000-1600) , in: Navas, J. (Ed.), GEODE. Mapa Geológico Digital Continuo
752 de España. Sistema de Información Continua: SIGECO. IGME, Madrid.

- 753 Michetti, A.M., Esposito, E., Guerrieri, L., Porfido, S., Serva, L., Tatevossian, R., Vittori, E.,
754 Audemard, F., Azuma, T., Clague, J., Comerci, V., Gurpinar, A., McCalpin, J.,
755 Mohammadioun, B., Morner, N.A., Ota, Y., R., 2007. Intensity Scale ESI 2007. Mem.
756 Descr. della Cart. Geol. d'Italia, Spec. Vol. 74 7–54.
- 757 Pederson, J.L., Mackley, R.D., Eddleman, J.L., 2002. Colorado Plateau uplift and erosion
758 evaluated using GIS. *GSA Today* 12, 4–10. [https://doi.org/10.1130/1052-
759 5173\(2002\)012<0004:CPUAEE>2.0.CO;2](https://doi.org/10.1130/1052-5173(2002)012<0004:CPUAEE>2.0.CO;2)
- 760 Pulgar, J.A., Alonso, J.L., Espina, R.G., Marín, J.A., 1999. La deformación alpina en el
761 basamento varisco de la Zona Cantábrica. *Trab. Geol.* 21, 283–294.
- 762 Ramsay, J.G., 1967. *Folding and fracturing of rocks*. McGraw-Hill, New York.
- 763 Reicherter, K., Michetti, A.M., Barroso, P.G.S., 2009. Palaeoseismology: Historical and
764 prehistorical records of earthquake ground effects for seismic hazard assessment. *Geol.*
765 *Soc. Spec. Publ.* 316, 1–10. <https://doi.org/10.1144/SP316.1>
- 766 Rodríguez-Pérez, C., 2012. La evolución antigua del relieve en el área central de la Cordillera
767 Cantábrica. *Eria* 89, 203–230.
- 768 Rodríguez-Rodríguez, L., Jiménez-Sánchez, M., Domínguez-Cuesta, M.J., Aranburu, A., 2015.
769 Research history on glacial geomorphology and geochronology of the Cantabrian
770 Mountains, north Iberia (43-42°N/7-2°W). *Quat. Int.* 364.
771 <https://doi.org/10.1016/j.quaint.2014.06.007>
- 772 Rosenbauer, R.J., 1991. UDATE1: A computer program for the calculation of uranium-series
773 isotopic ages. *Comput. Geosci.* 17, 45–75. [https://doi.org/https://doi.org/10.1016/0098-
774 3004\(91\)90079-S](https://doi.org/https://doi.org/10.1016/0098-3004(91)90079-S)
- 775 Shen, C.C., Lawrence Edwards, R., Cheng, H., Dorale, J.A., Thomas, R.B., Bradley Moran, S.,
776 Weinstein, S.E., Edmonds, H.N., 2002. Uranium and thorium isotopic and concentration
777 measurements by magnetic sector inductively coupled plasma mass spectrometry. *Chem.*
778 *Geol.* 185, 165–178. [https://doi.org/10.1016/S0009-2541\(01\)00404-1](https://doi.org/10.1016/S0009-2541(01)00404-1)
- 779 Stich, D., Martínez-solares, J.M., Custódio, S., Batlló, J., Martín, R., Teves-costa, P., Morales,
780 J., 2020. Seismicity of the Iberian Peninsula, in: Quesada, C., Oliveira, J. (Eds.), *The*
781 *Geology of Iberia: A Geodynamic Approach*. Springer International Publishing, pp. 11–
782 32. <https://doi.org/10.1007/978-3-030-10931-8>
- 783 Storti, F., Billi, A., Salvini, F., 2003. Particle size distributions in natural carbonate fault rocks:
784 Insights for non-self-similar cataclasis. *Earth Planet. Sci. Lett.* 206, 173–186.
785 [https://doi.org/10.1016/S0012-821X\(02\)01077-4](https://doi.org/10.1016/S0012-821X(02)01077-4)
- 786 Talvitie, N., 1972. Electrodeposition of actinides for alpha spectrometric determination. *Anal.*
787 *Chem.* 44, 280–283.
- 788 Turcotte, D.L., 1986. Fractals and fragmentation. *J. Geophys. Res. Solid Earth* 91, 1921–1926.
789 <https://doi.org/10.1029/JB091iB02p01921>
- 790 Wasowski, J., McSaveney, M.J., Pisano, L., Del Gaudio, V., Li, Y., Hu, W., 2021. Recurrent
791 rock avalanches progressively dismantle a mountain ridge in Beichuan County, Sichuan,
792 most recently in the 2008 Wenchuan earthquake. *Geomorphology* 374.
793 <https://doi.org/10.1016/j.geomorph.2020.107492>
- 794 Weil, A.B., Voo, R. Van der, van der Pluijm, B.A., 2001. Oroclinal bending and evidence
795 against the Pangea megashear: The Cantabria-Asturias arc (northern Spain). *Geology* 29,
796 991. [https://doi.org/10.1130/0091-7613\(2001\)029<0991:OBAEAT>2.0.CO;2](https://doi.org/10.1130/0091-7613(2001)029<0991:OBAEAT>2.0.CO;2)
- 797 Zeng, Q., Yuan, G., McSaveney, M., Ma, F., Wei, R., Liao, L., Du, H., 2020. Timing and

798 seismic origin of Nixu rock avalanche in southern Tibet and its implications on Nimu
799 active fault. Eng. Geol. 268, 105522. <https://doi.org/10.1016/j.enggeo.2020.105522>
800

801 **Figure and table captions**

802 Fig. 1: (A) Overview map of NW Spain presenting the evidence for the main Alpine exhumation
803 phase in the Cantabrian Mountain and Basque-Cantabrian Basin. (B) Geological map of the
804 Cantabrian Zone. Available seismic records are indicated with stars, and the trace of the
805 geological section (C). Inset shows the location of Fig. 2. The Somiedo (SoT) and Sobia (ST)
806 thrusts.

807 Fig. 2: Aerial image of Sierra de la Sobia and Macizo de Ubiña. Main segments of the northern
808 León Fault sector, rock-avalanches and the highest summits are highlighted (orange lines). The
809 orange arrow shows the NNW trends of the current regional maximum horizontal stress (SHmax;
810 de Vicente et al. 2008).

811 Fig. 3: Geological map of the Sobia Nappe showing the relationships between rock-avalanche,
812 Quaternary sediments, mechanical contacts and relief. Traces of the geological section
813 represented in Fig. 4 are also shown.

814 Fig. 4: Longitudinal-section (A) and three cross-sections (B, C, and D) to Sierra de la Sobia.
815 Traces of the transversal cross-sections and the range level of summits (RLS) line are located on
816 the longitudinal-section A.

817 Fig. 5: Panoramic view of a 15km-long segment of Sierra de la Sobia, including the hinge and
818 southern domains. Carboniferous limestone outcrop exposes MS, thrusting out of sequence the
819 earliest Variscan syncline and thrust. Minor normal and strike-slip faults cut the MS-trace, also
820 folded by the Foz de la Estrechura anticline, southward. RLS have small steps controlled by the
821 vertical slip of both later-normal and strike-slip faults as the mountain chain increases in height
822 southward (see also Fig. 4A).

823 Fig. 6: Structural map of Sierra de la Sobia showing the relationship between the León Fault, the
824 latest faults and the fracture network imposed on the limestone massif. The stereonet plots
825 represent the equal area and lower hemisphere projections of fault planes and slickenlines. Arrows
826 represent the direction of displacement inferred from slickenlines. Blue lines and symbols

827 represent fault segments reactivated during the Quaternary and their respective kinematics.
828 Orange finite strain ellipse is scaled to $R=1.42$, strain ellipse orientation is consistent with the
829 kinematic of most current active faults.

830 Fig. 7: Detailed geomorphological map of the Gradura and Entrago rock-avalanches including
831 earth flow, slope dynamic and river deposits. Stars show the location of U/Th samples.

832 Fig. 8: Entrago rock-avalanche. (A) Details of the rupture scarp where a rotational rockslide (rock
833 slump) rests atop. The Sobia spire is a buttress 125 m in height separated by less than 50 m from
834 the rupture scarp. A huge rock-topple was triggered at the southern scarp tip. Note that
835 discontinuities have the same pattern into the rupture scarp than in the rock-slump. (B) Behind
836 the Sobia spire a transverse fault N5°E-strike with slickenlines indicating sub-horizontal right-
837 lateral displacement (North is on the left-hand side) is exposed.

838 Figure 9: Dynamic analysis of slope instability risk considering four failure modes for the rupture
839 scarp of Entrago. Flexural toppling analysis following Goodman (1989) and direct toppling
840 following Hudson and Harrison (1997). Pole planes are plotted in lower hemispheres and equal
841 angle stereonets. Contour density at constant intervals of 0.7%.

842 Fig. 10: Shape-fabric analysis of the depletion zone for the Entrago rock-avalanche (612 wedges).
843 (A) Diagram showing the size frequency (black line) and the area percentage (dashed line) versus
844 wedge size. (B) Histogram showing the frequency of the orientation of the major ellipse inscribed
845 in each wedge. Fine fraction (white bars) of wedges was sketched from the thickly fractured rock-
846 slump of the unstable residual relief (Fig. 7A) and it preserves the same orientation than the coarse
847 fraction (black bars). (C) Shape parameter (S ; Fernández et al., 2005) versus eccentricity diagram.
848 Triangular wedges, defined by the intersection of joint sets, dominate within the fine fraction
849 (white dot), and rhomboidal wedges dominate within the coarse fraction (black dot). Error bars
850 represent standard deviations.

851 Fig. 11: Block size analysis of the Entrago rock-avalanche. (A) Histogram of equivalent radii
852 (dm) for the whole accumulation body (4805 blocks). (B) Log-log plot of frequency versus

853 equivalent radius (20 bins per order of magnitude). The slope of the fitting lines yields two D -
854 values which intersect at r_k . (C) Histogram of equivalent radii (dm) for the three superimposed
855 bodies mapped (Fig. 7). (D) Log-log plot of frequency versus equivalent radius for the earliest,
856 (E) middle and (D) the apical bodies.

857 Fig. 12: Shape-fabric analysis of blocks for the four accumulation bodies studied in detail. (A)
858 Log-log plot of frequency versus equivalent radius (20 bins per order of magnitude). The slope
859 of the fitting lines yields two D -values which intersect at r_k . (B) Shape parameter (S ; Fernández
860 et al., 2005) versus eccentricity diagram. Error bars are their respective standard deviations. Block
861 sizes plotted for each fine fraction is larger than $\text{Log}(r_i)=0.5$ (dm).

862 Fig. 13: Detailed geomorphological map of the Sobrevilla and Carrea rock-avalanches (left and
863 right, respectively). Start indicates the location of U/Th samples.

864 Fig. 14: Detailed geomorphological map of rock-avalanches occurred at Fresneu, Cueva Güerta,
865 Villa de Sub, Sabariegos and Busbigre. Stars indicate the location of U/Th samples of calcite
866 cements coating the blocks of the Cueva Güerta rock-avalanche deposit. Cave plan view modified
867 after Ferreras et al. (2015).

868 Fig. 15: South-Eastern Sierra de la Sobia. Villa de Sub is located down hillslope at the tip of the
869 accumulation body. (A) Geology sketched onto the picture highlights the effect of the current
870 right-lateral faults (F_{p1}) and fold-related onto the back-thrust structure of the basement. One of
871 such fault is the rupture plane of the Villa de Sub rock-avalanche. (B) The picture shows the
872 regular and penetrative joint set J_{p1} associated with faults F_{p1} . Limestone bedding surfaces (S_0)
873 dip in the opposite direction to the SE hillslope, enhancing the risk for direct toppling. Width of
874 view is ~ 500 m in A, and ~ 50 m in B.

875 Table 1: Geometrical features of rock-avalanches located at the northern domain (Marabio); the
876 hinge domain (Gradura, Entrago and Sobrevilla); and the southern domain of Sierra de la Sobia
877 (Carrea, Cueva Güerta, Villa de Sub, Sabariegos and Busbigre). Sites are in Figs. 3 and 5. H is
878 the vertical drop and L is the length of fall. H/L ratio is the Fahrböschung parameter of Heim

879 (1932) and ϕ is the corresponding angle. Dimension fractal (D) for the block size distribution
880 (BSD) within the accumulation bodies are obtained from the slope line fit yield values $> r_k$ (Fig.
881 12 A).

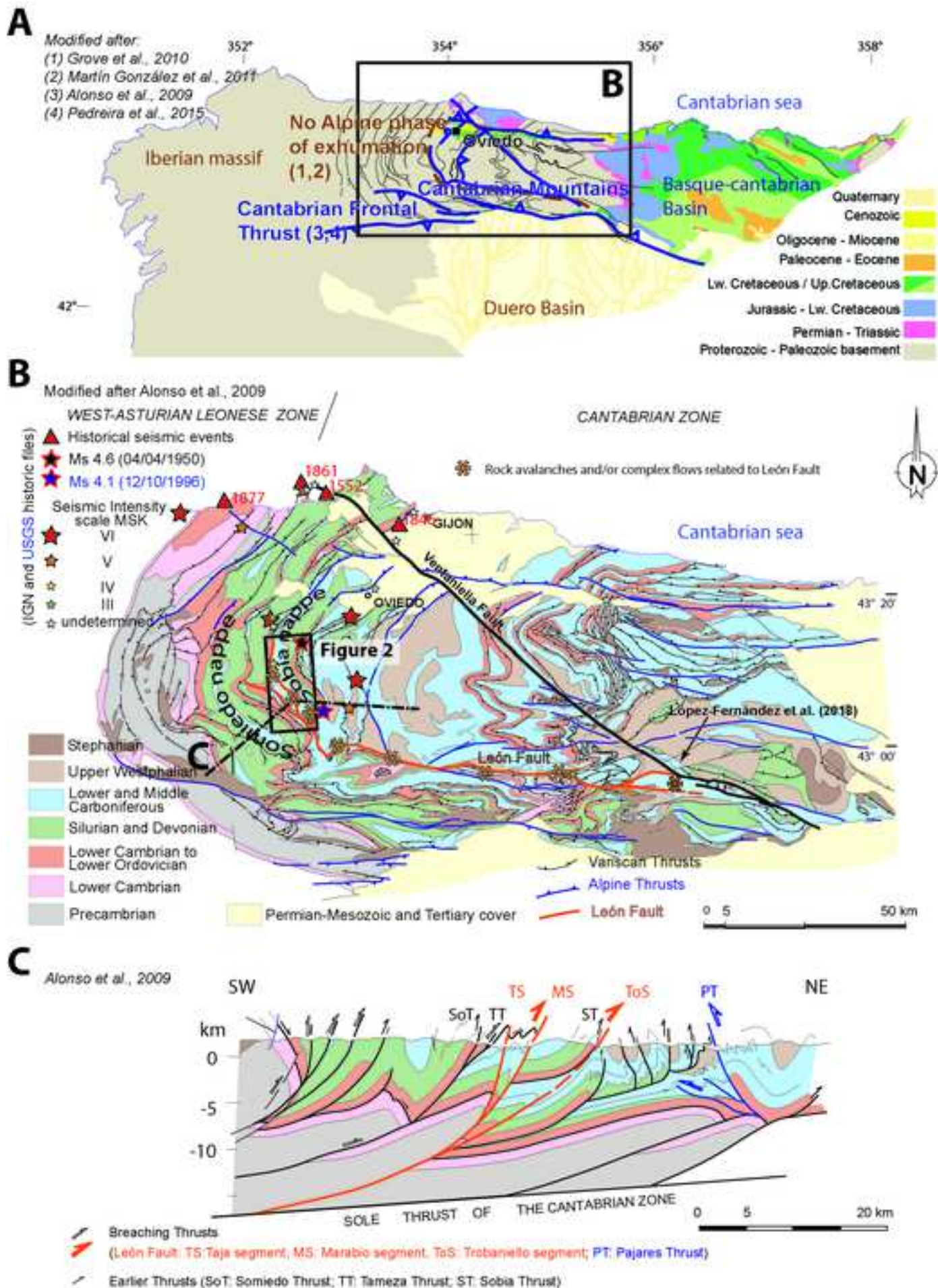
882 Table 2 U/Th isotopic compositions and ^{230}Th ages for samples analysed by α -spectrometry.
883 Analytical errors are 2σ of the mean. Samples, UTM coordinates ETRS-89, 29T.

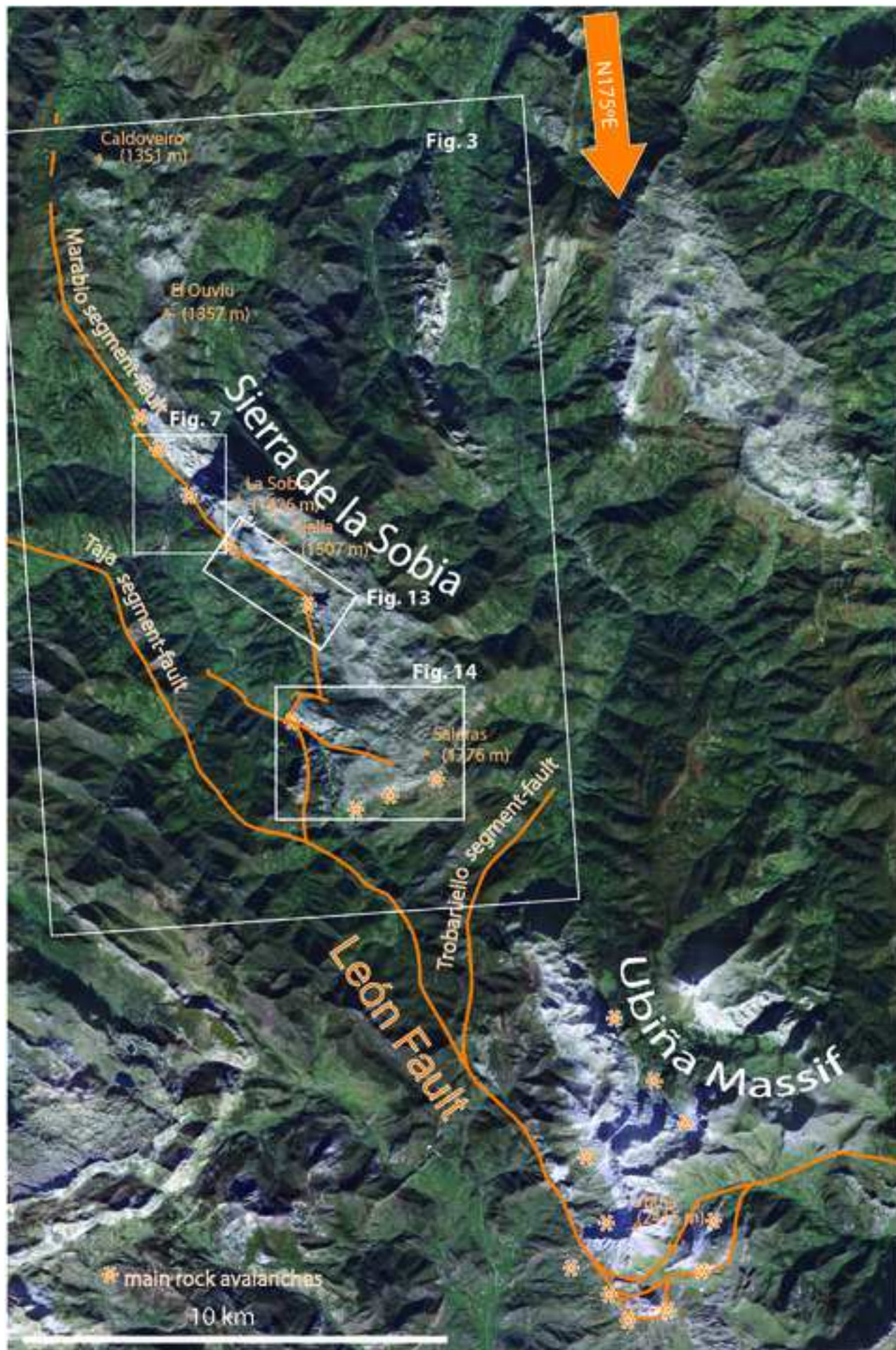
884 Table 3: U/Th isotopic compositions and ^{230}Th ages for samples analysed by Alpha spectrometry.
885 Analytical errors are 2σ . UTM coordinates ETRS-89, 29T.

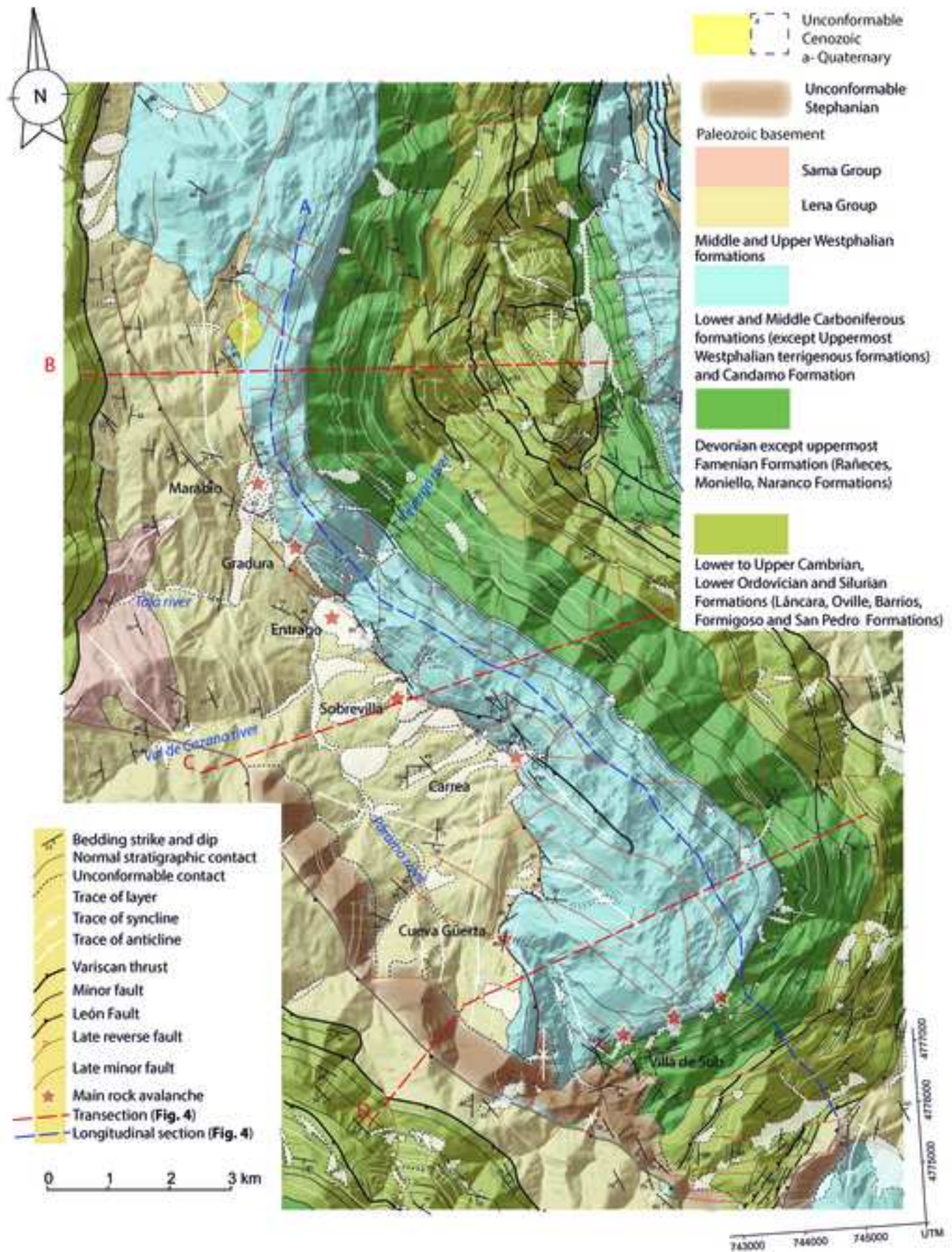
Rock avalanche	H (km)	L (km)	ϕ (degrees)	Deposit Width (km)	Source area (km²)	Deposit area (km²)	Deposit Depth (m)	Volume ($\times 10^6$ m³)	D-BSD (fractal)
Marabio	0.41	1.28	18	0.15	0.0247	0.0715	20	0.07	
Gradura	0.56	0.84	34	0.27	0.1278	0.1698	12	2.03	
Entrago	0.71	1.16	31	0.65	0.1232	0.4315	29	12.5	2.35
Sobrevilla	0.71	1.79	29	0.64	0.1570	0.2268	25	5.67	
Carrea	0.68	1.57	23	0.19	0.1157	0.1312	25	3.28	2.56
Cueva Güerta	0.07	0.07	45	0.07	0.0007	0.0043	30	0.13	2.70
Villa de Sub	0.25	0.39	33	0.11	0.0122	0.0219	5	0.11	2.24
Sabariegos	0.27	0.81	18	0.17	0.0121	0.0325	10	0.16	
Busbigre	0.21	0.53	22	0.10	0.0153	0.0299	5	0.07	
Mean	0.43	0.88	28	0.26	0.0654	0.1244	21.22	2.68	
Standard deviation	± 0.24	± 0.49	± 9	± 0.23	± 0.0634	± 0.1378	± 17.07	± 4.16	
Total					0.5887	1.1194		24.15	

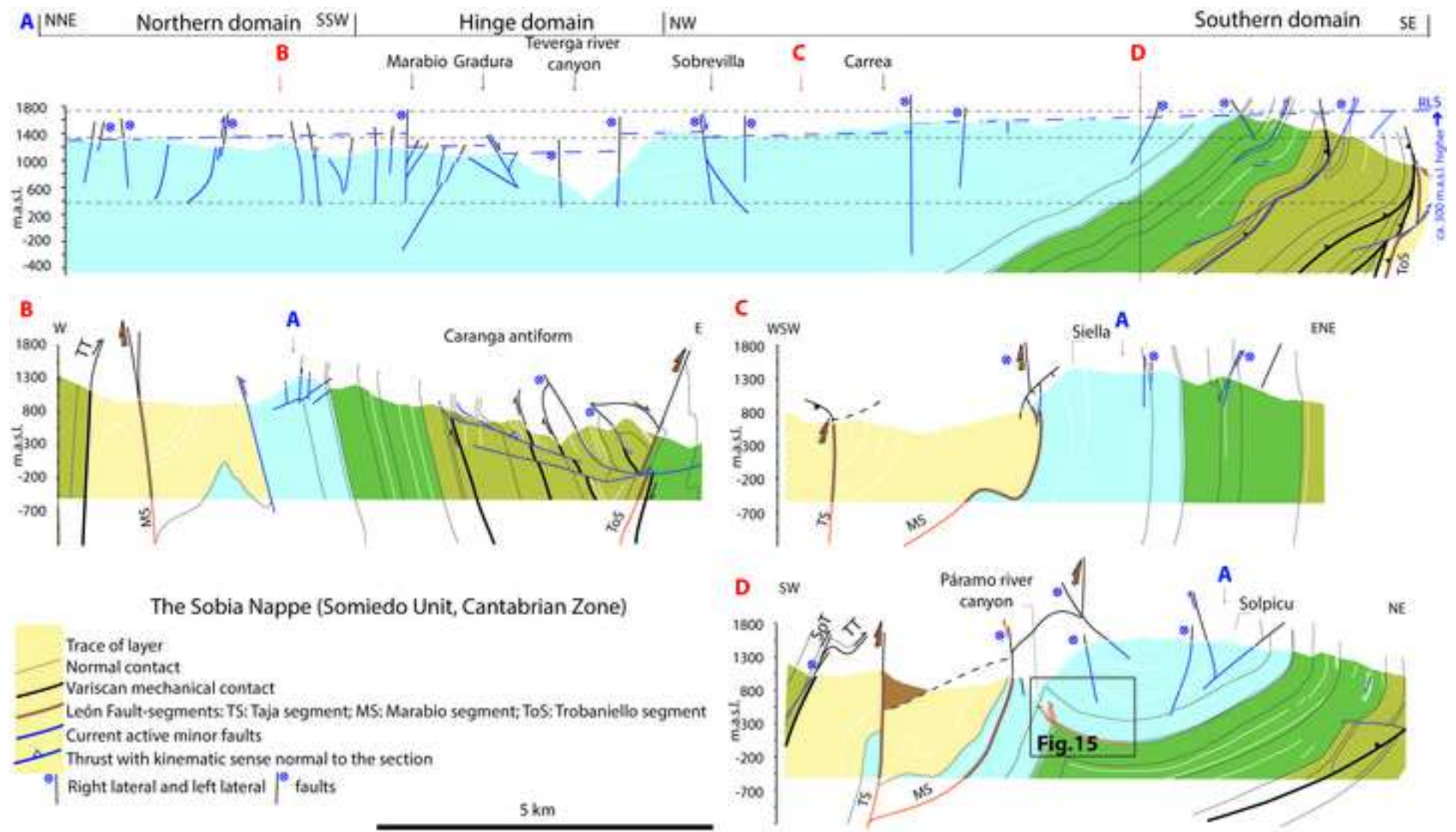
Sample ID	RB_03	RB_05	RB_02	RB_07	RB_06
Weight (g)	0.3498	0.3471	0.3548	0.3532	0.3603
Coord. X	739331.12	736360.02	739319.66	736458.12	736281.16
Coord. Y	4778755.92	4784219.02	4781901.94	4784017.74	4784023.89
Altitude (m.a.s.l)	673.49	445.91	1083.06	492.02	471.67
Rock avalanche	Cueva Güerta	Entrago	Carrea	Entrago	Entrago
^{238}U (ppb)	36.1 ± 0.1	125.7 ± 0.2	441.2 ± 0.9	398.2 ± 1.1	1296.7 ± 6.9
^{232}Th (ppt)	17970 ± 360	2786 ± 56	68918 ± 2123	87155 ± 4086	66395 ± 1575
$\delta^{234}\text{U}_{\text{Measured}}$ ^a	102.2 ± 2.7	-2.2 ± 2.5	2.4 ± 1.6	19.7 ± 2.1	6.7 ± 3.1
$[\text{}^{230}\text{Th}/\text{}^{238}\text{U}]_{\text{Activity}}$ ^b	0.20 ± 0.04	0.123 ± 0.006	0.44 ± 0.07	0.86 ± 0.09	0.93 ± 0.02
$[\text{}^{230}\text{Th}/\text{}^{232}\text{Th}]$ ^c	7 ± 2	91 ± 5	47 ± 8	63 ± 8	300 ± 10
Age Uncorrected (yr)	21519 ± 5822	14317 ± 791	63452 ± 14821	200834 ± 75643	279791 ± 33327
$\delta^{234}\text{U}_{\text{initial}}$ corrected	104 ± 4	-2 ± 3	3 ± 2	34 ± 8	15 ± 7
Age corrected ^{b,d} (yr)	7561 ± 11216	13669 ± 910	58823 ± 14577	194345 ± 70211	278312 ± 32868
Quaternary stage	Holocene	Late Pleistocene	Late Pleistocene	Middle Pleistocene	Middle Pleistocene
MIS stage	1	1	3	7a	9a
After glacial-(ka)	Termination I-14	Termination I-14	Termination II-130	Termination III-243	Termination IV-337

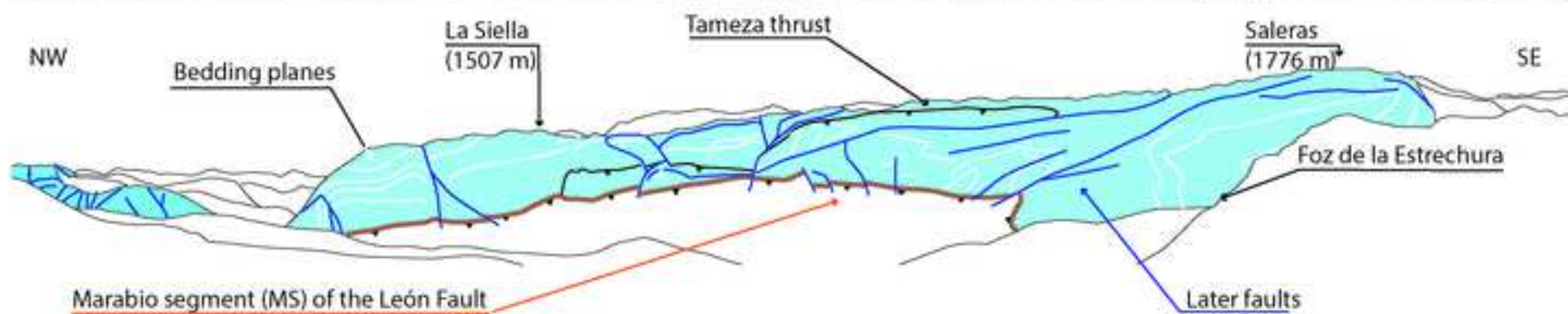
Sample ID	RB_10	RB_09
Weight (g)	19.81	17.16
Coord. X	739331.12	739620.8
Coord. Y	4778755.92	4781818.74
Rock avalanche	Cueva Güerta	Carrea
Altitude (m.a.s.l)	673.49	673.49
²³⁸ U (ppm)	0.05	0.16
²³² Th (ppm)	0.01	0.02
²³⁴ U/ ²³⁸ U	1.24+/-0.08	0.93+/-0.03
²³⁰ Th/ ²³² Th	7.266+/-2.211	8.317+/-1.240
²³⁰ Th/ ²³⁴ U	0.09+/-0.01	0.30+/-0.02
Nominal date (years BP)	9945+1222/-1209	38327+2890/-2820
Quaternary stage	Holocene	Late Pleistocene
MIS stage	1	3
After Glacial-(ka)	Termination I-14	Termination II-130

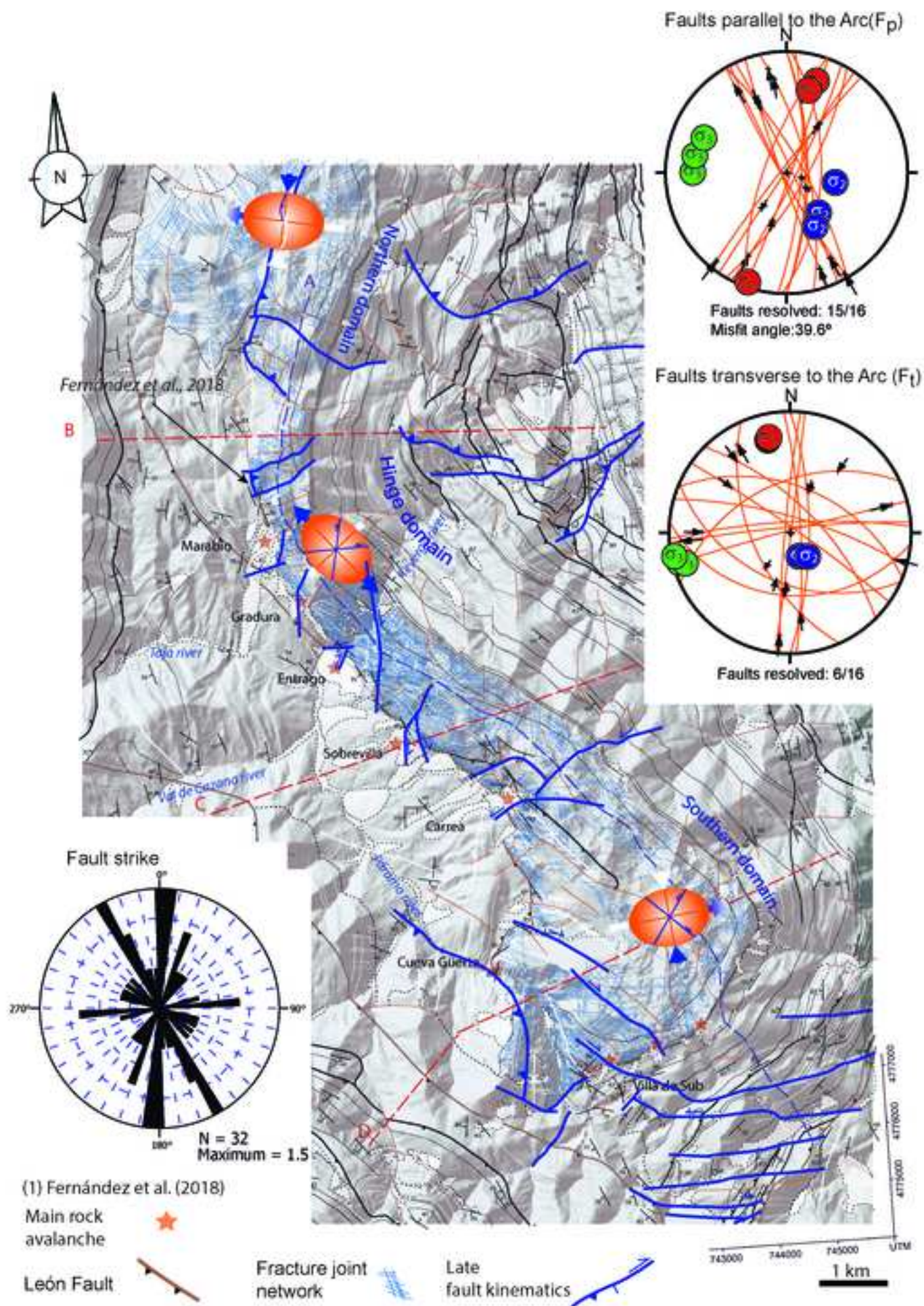


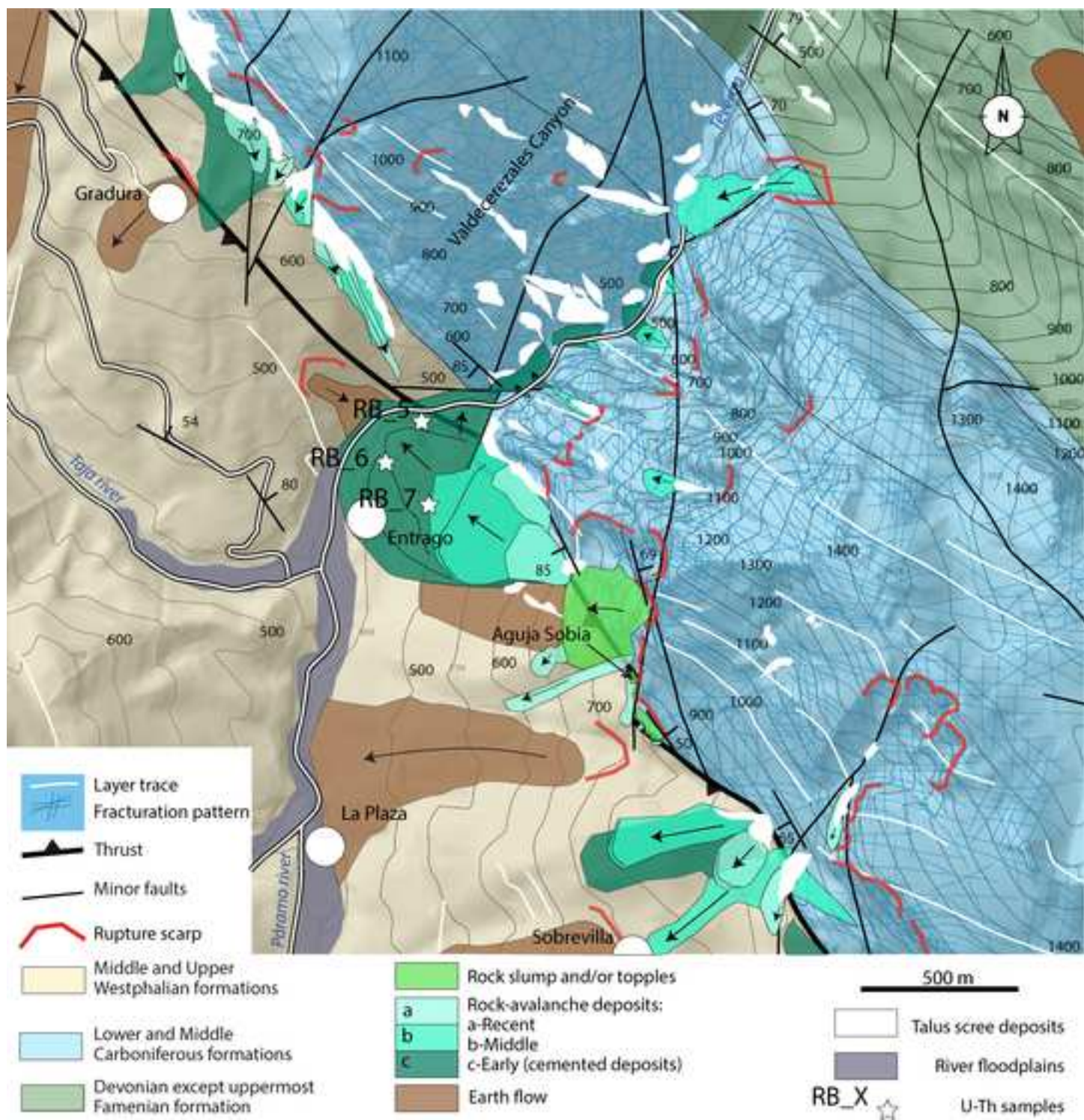


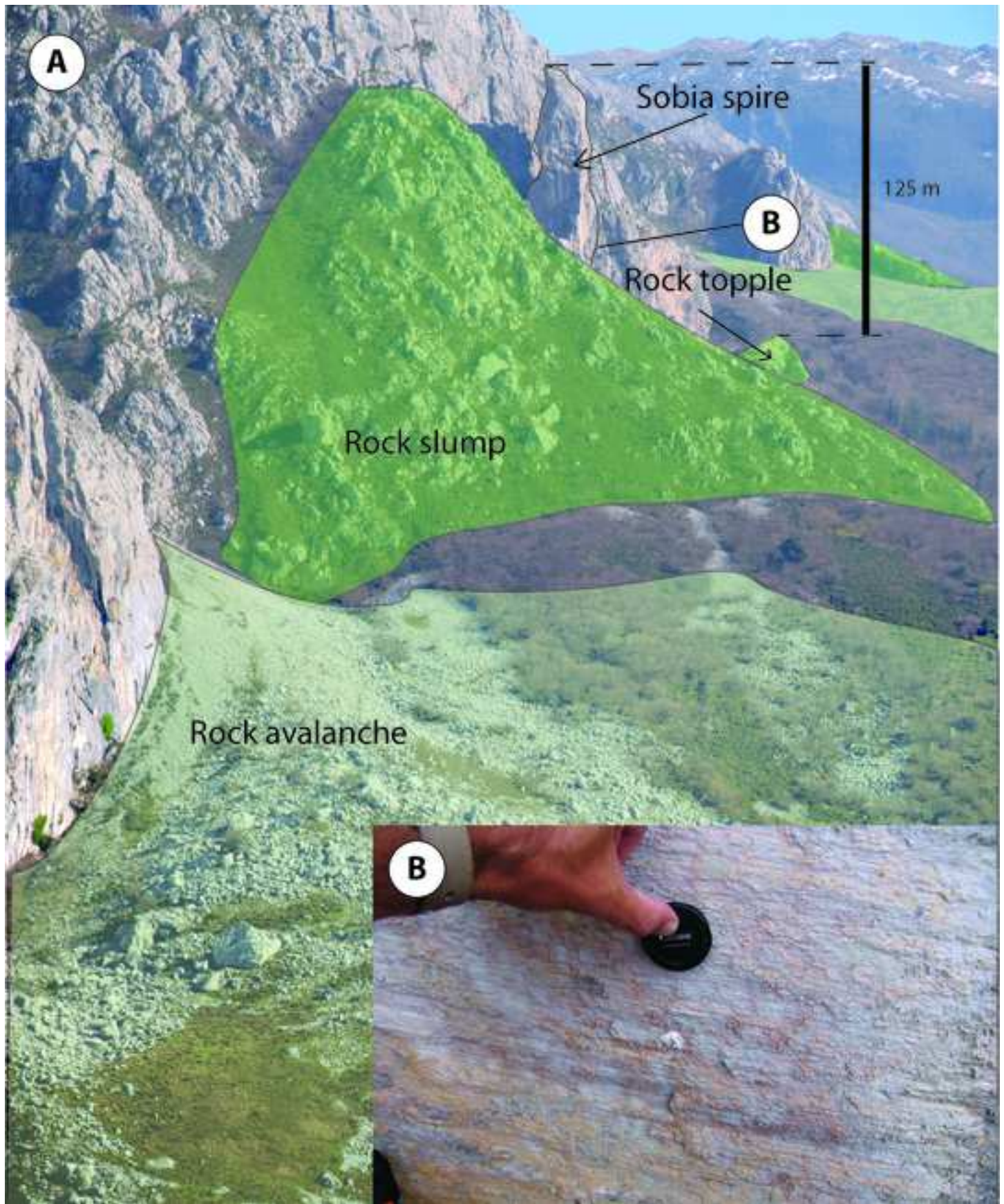




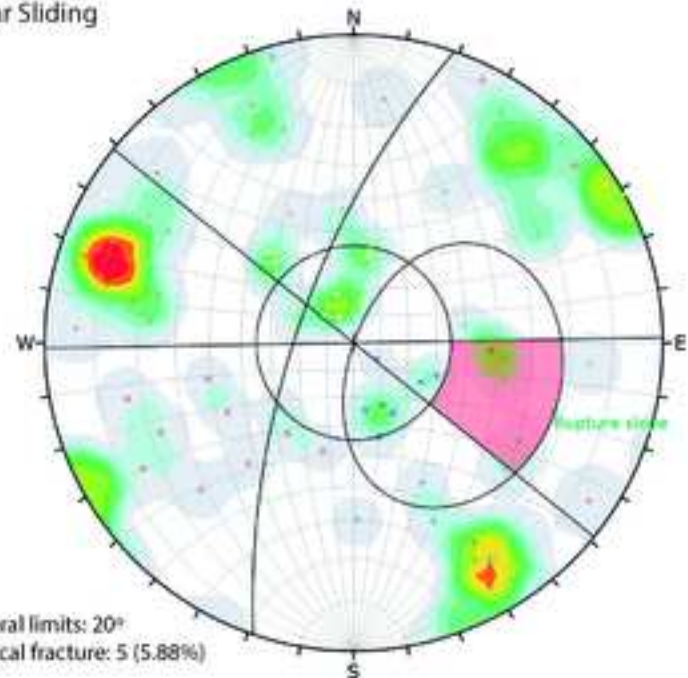








Planar Sliding

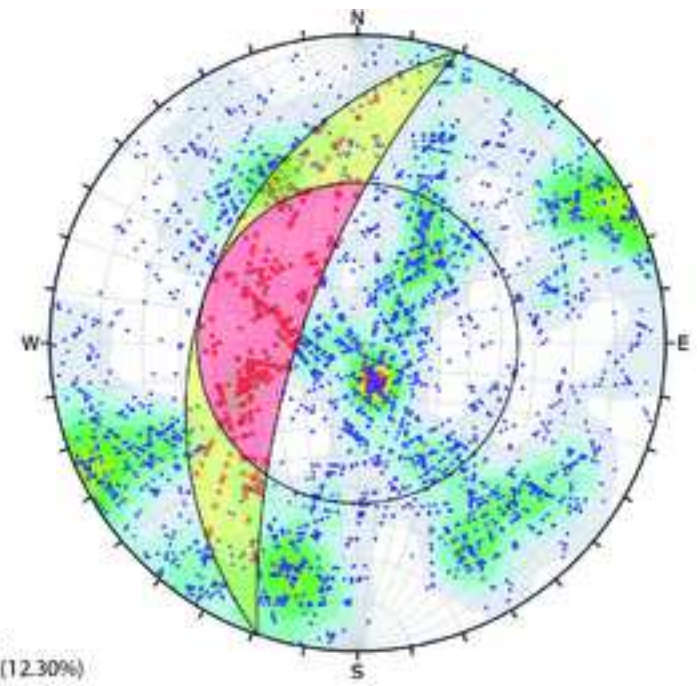


Wedge Sliding

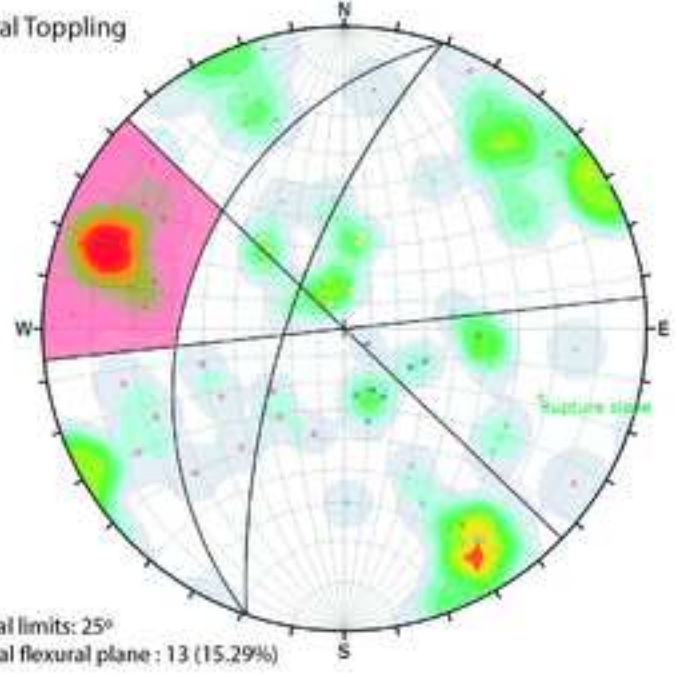
Fracture sets N:

○	Fp	1
×	Fr	5
△	Jp	16
+	Jr1	18
▽	Jr1'	13
□	Jr2	13
◁	Jr2'	7
○	S0	12

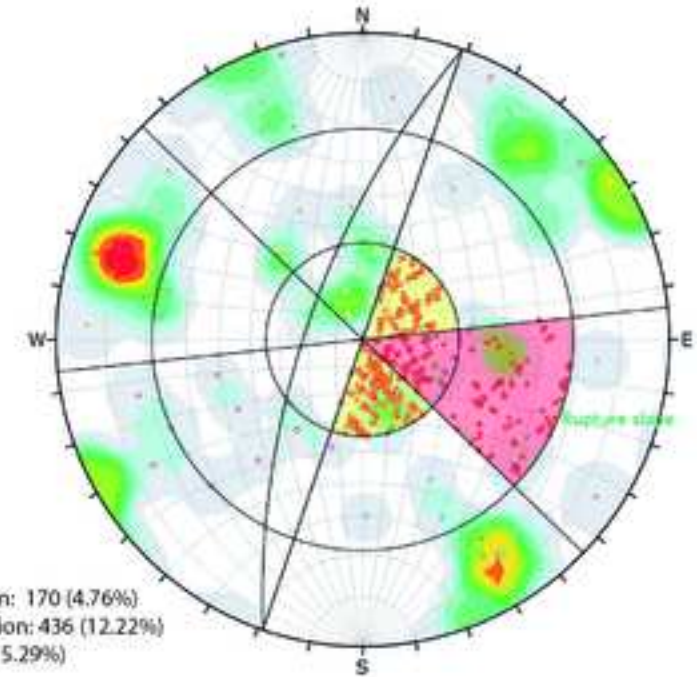
■ Critical intersection
● Intersection

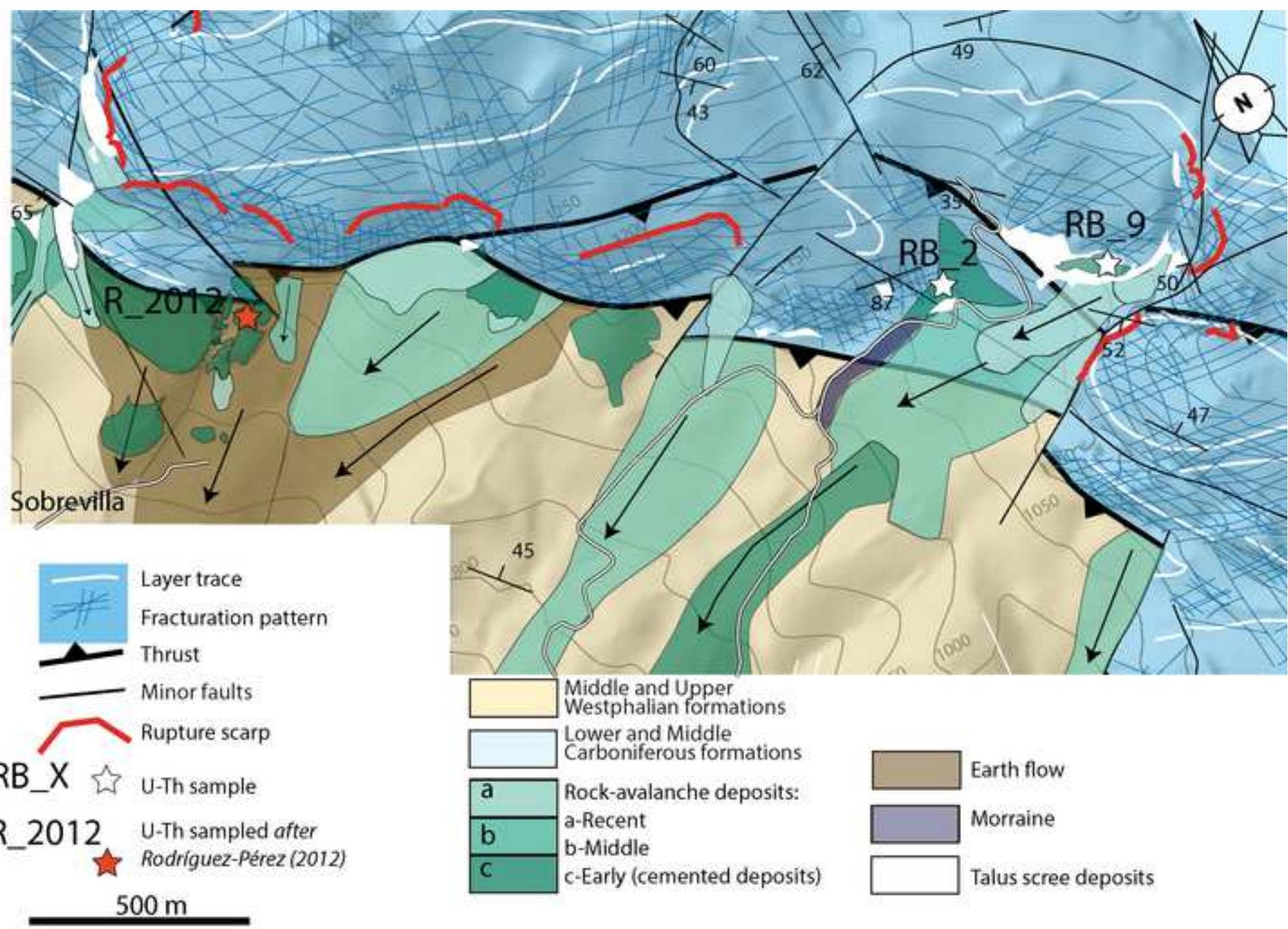


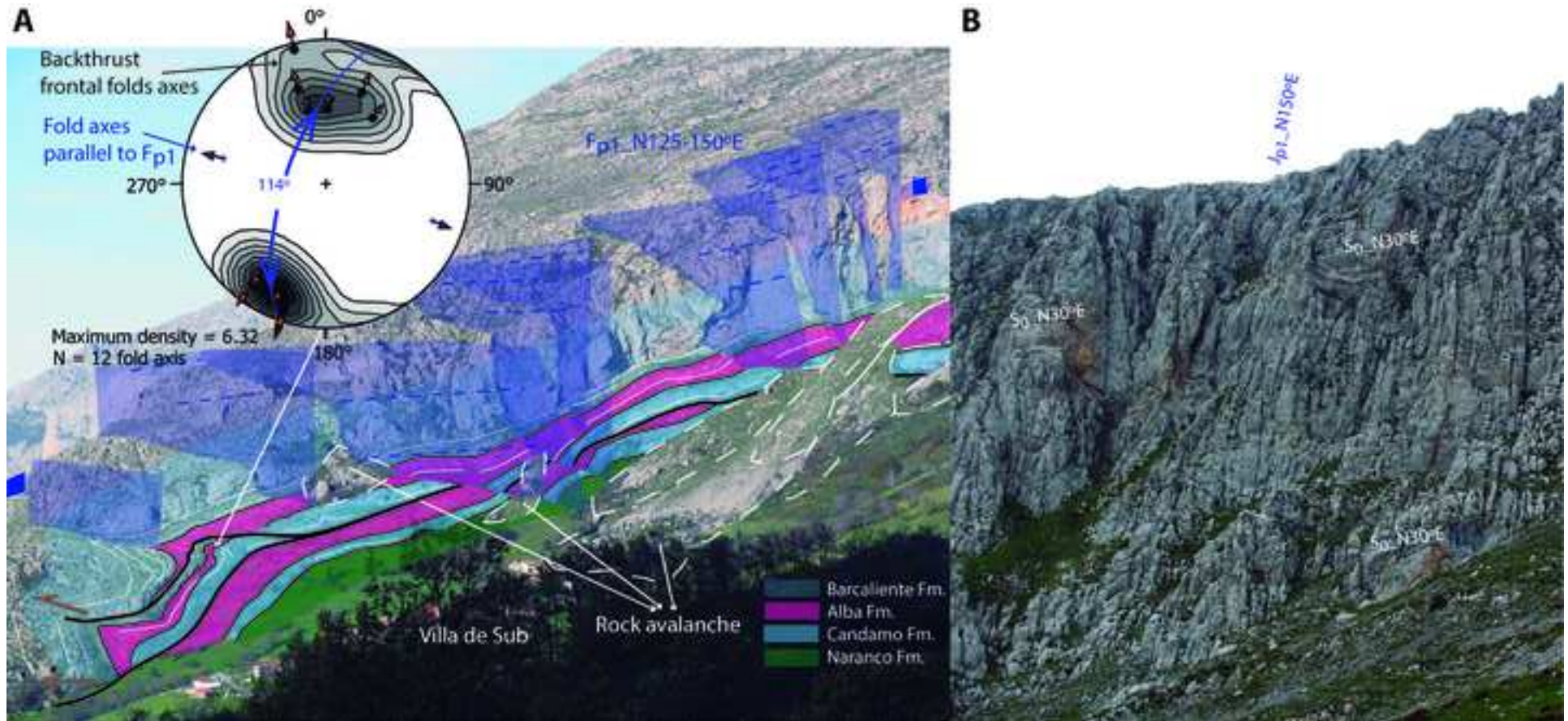
Flexural Toppling

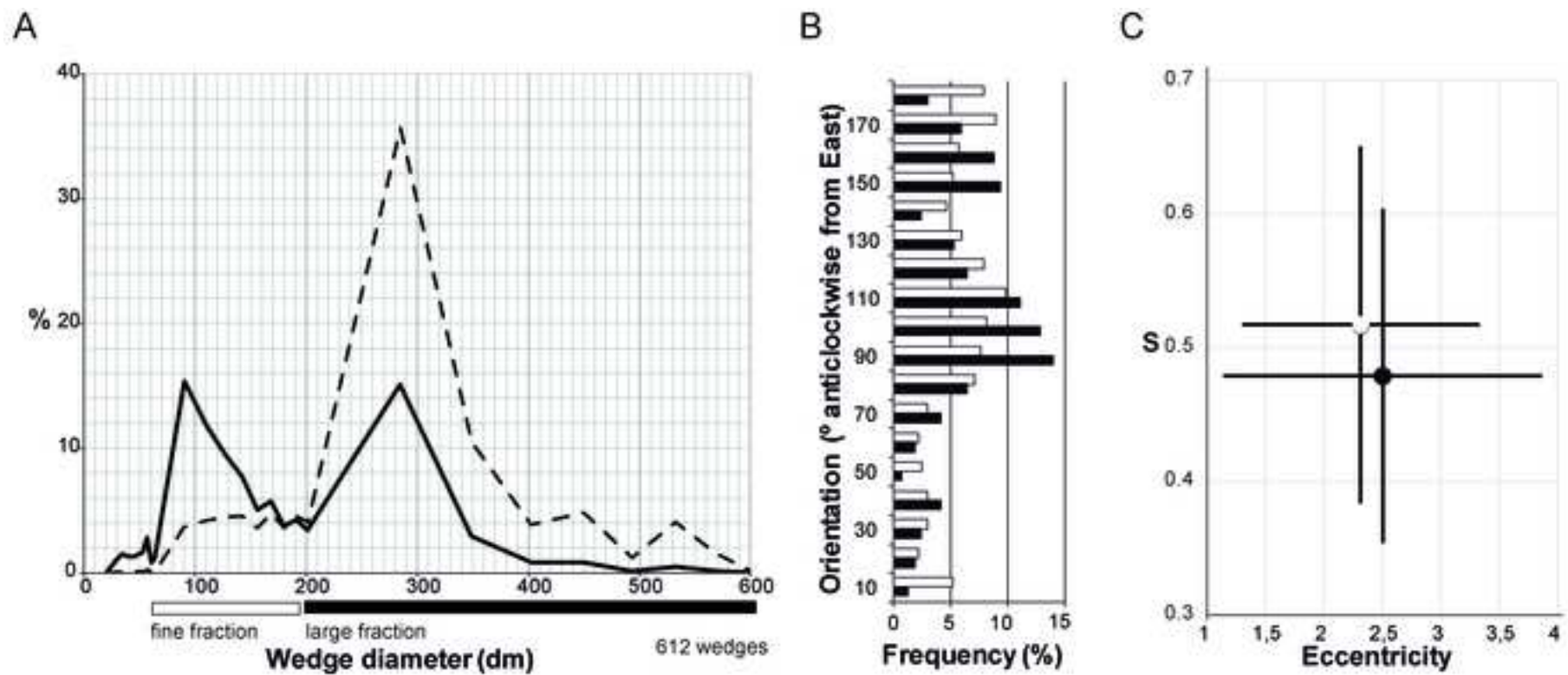


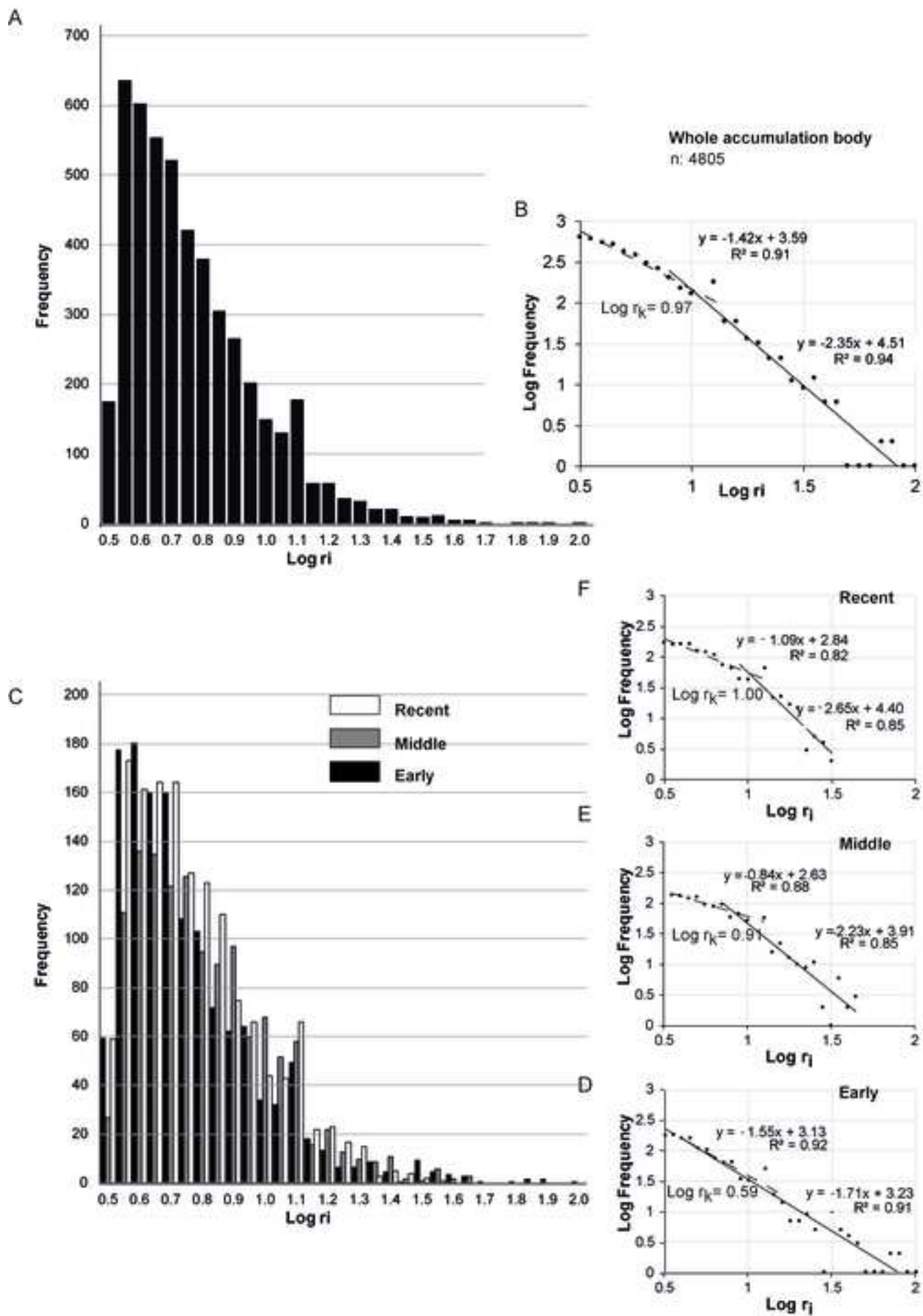
Direct Toppling

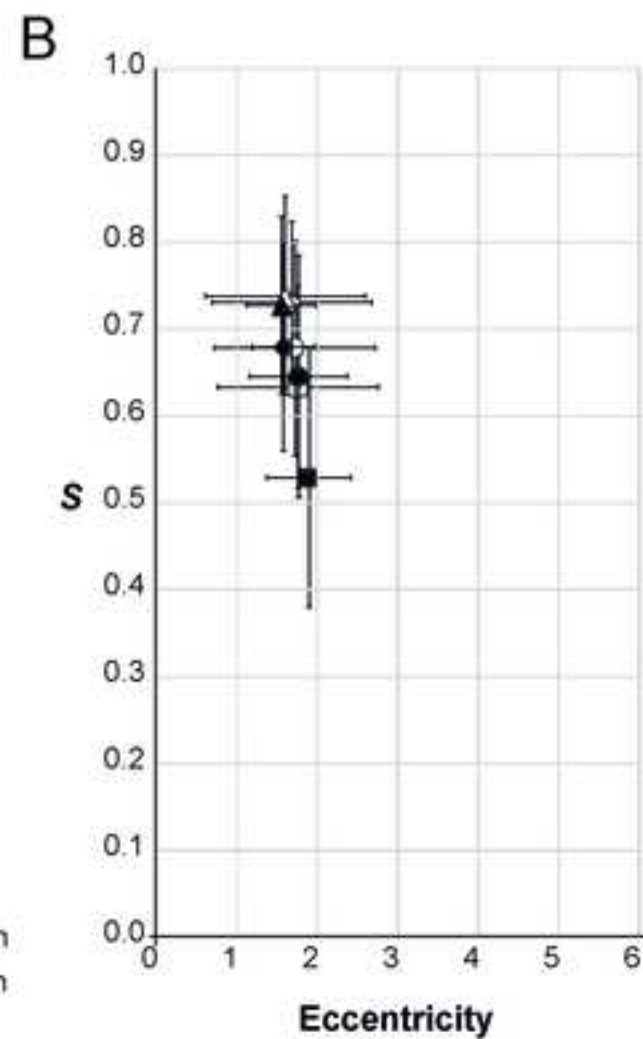
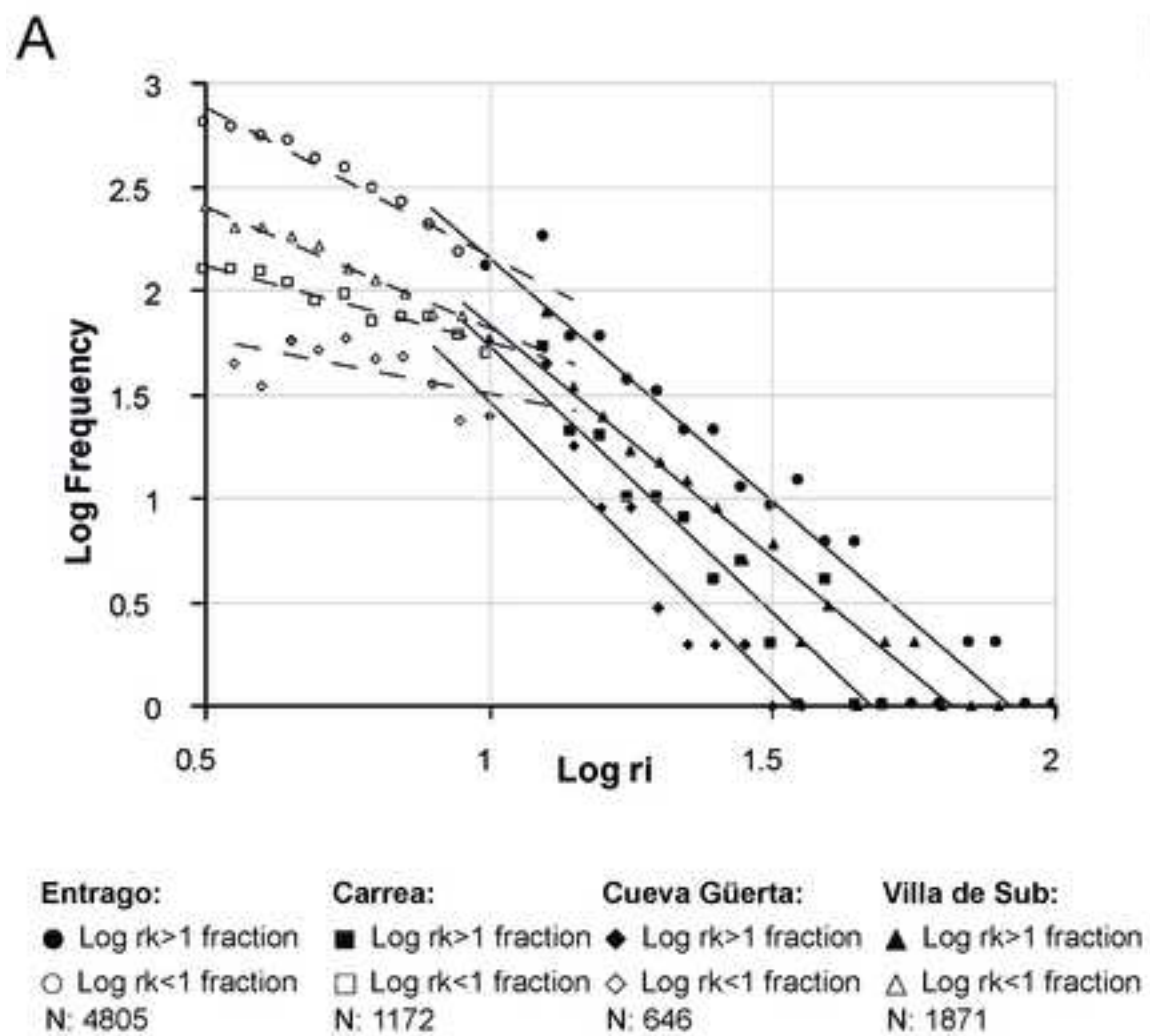












Author declaration

[Instructions: Please check all applicable boxes and provide additional information as requested.]

1. Conflict of Interest

Potential conflict of interest exists:

We wish to draw the attention of the Editor to the following facts, which may be considered as potential conflicts of interest, and to significant financial contributions to this work:

The nature of potential conflict of interest is described below:

No conflict of interest exists.

We wish to confirm that there are no known conflicts of interest associated with this publication and there has been no significant financial support for this work that could have influenced its outcome.

2. Funding

Funding was received for this work.

All of the sources of funding for the work described in this publication are acknowledged below:

Research funded by the Spanish Ministry of Education and Science, through project CGL2015-66997-R from the National Research plan, and by the FC-GRUPIN-IDI72018/000216 project of the Principado de Asturias government

No funding was received for this work.

3. Intellectual Property

We confirm that we have given due consideration to the protection of intellectual

property associated with this work and that there are no impediments to publication, including the timing of publication, with respect to intellectual property. In so doing we confirm that we have followed the regulations of our institutions concerning intellectual property.

4. Research Ethics

X We further confirm that any aspect of the work covered in this manuscript that has involved human patients has been conducted with the ethical approval of all relevant bodies and that such approvals are acknowledged within the manuscript.

X IRB approval was obtained (required for studies and series of 3 or more cases)

X Written consent to publish potentially identifying information, such as details or the case and photographs, was obtained from the patient(s) or their legal guardian(s).

5. Authorship

X We confirm that the manuscript has been read and approved by all named authors.

X We confirm that the order of authors listed in the manuscript has been approved by all named authors.

6. Contact with the Editorial Office

The Corresponding Author declared on the title page of the manuscript is:

Francisco José Fernández (ffernandez@uniovi.es)

The corresponding author on behalf of the other coauthors agree with all of the above.

Author's name (Fist, Last)

Signature

Date

1. Francisco José Fernández



Digitally signed by Francisco José
 José
 DN: cn=Francisco José,
 o=Universidad de Oviedo,
 ou=University,
 email=ffernandez@uniovi.e
 s, c=ES
 Date: 2021.01.21 13:59:20
 +01'00'

21/01/2021

